University of Liège

Faculty of Medicine

Laboratory of Tumor and Development Biology

Promoter: Pr. Didier Cataldo (Faculty of Medicine)

Co-promoter: Pr. Mireille Dumoulin (Faculty of Sciences)

Inhibition of ADAM10 targeted to mesothelioma: development of a Dual Targeting protein

Marco Morbidelli

Thesis submitted for the Degree of Doctorate in Biomedical and Pharmaceutical Sciences

Academic year 2025/2026

University of Liège

Faculty of Medicine

Laboratory of Tumor and Development Biology

Promoter: Pr. Didier Cataldo (Faculty of Medicine)

Co-promoter: Pr. Mireille Dumoulin (Faculty of Sciences)

Inhibition of ADAM10 targeted to mesothelioma: development of a Dual Targeting protein

Marco Morbidelli

Thesis submitted for the Degree of Doctorate in Biomedical and Pharmaceutical Sciences

Academic year 2025/2026

Acknowledgements

ACKNOWLEDGEMENTS

"*Alone we can do so little; together we can do so much.*"
Helen Keller

I truly understood the depth of this quote during my PhD journey. These years have shown me the real importance of collaboration, of belonging to a community, a team, and ultimately a family. And a family is exactly what I found here in Belgium, a place that, after five years, I can finally call home. This feeling exists entirely because of the astonishing people I have met along the way, encounters that would never have happened had I not embarked on this adventure.

For this reason, and because I consider all of these people part of a "large family," I wish to express my deepest gratitude, to Didier Cataldo, for accepting me as a PhD candidate and for being one of the three pillars guiding me toward this moment. Your energy, optimism, and constant encouragement helped me navigate both successes and setbacks, giving me strength even in negative results and motivation to explore new directions. I am also grateful for all the extra-lab activities you organized, which strengthened the bonds within the LBTD team. I will never forget the Italian apéro wine tasting, nor how tipsy I became, and your kindness in inviting me to the Christmas party. To make sure I wasn't the only one without a present, you even took it upon yourself to be my Secret Santa. Thank you sincerely for all of this.

To Mireille Dumoulin, my co-supervisor and the second pillar, who shared with me her passion for nanobod… ah no, due to "copyright," I must say *VHHs*. Your scientific rigor, enthusiasm, and kindness have been essential throughout this work. Thank you for your patience, for correcting my mistakes, and for teaching me how to use magnificent biochemical instruments. Yes, thanks to you I fell in love with BLI and circular dichroism; I even dreamt about them. But it was not only about lab training: from our conference in Bled, I will always remember our hike to admire the view from the top of the mountain, and your stories about your PhD in Japan. These beautiful memories stayed with me and gave me strength to continue despite the many difficulties encountered in my project.

To Patricia Lassaux, last but certainly not least among my co-supervisors, the third pillar. If I am here today, I owe a great deal to you: for welcoming me as an Erasmus student, for being the first to help me find projects and funding, and for supporting me when everything in Belgium was still new. Thank you for always finding time for me, for giving me new ideas, and for following me throughout the project. Thank you for trusting me from the very beginning and letting me explore phage display and enzymatic assays. This trust allowed me to grow and become the person I am today. Thank you for being the first to treat me as an equal and make me feel part of the family. And thank you for the amazing team-building trips, from amusement parks to Madrid, which I will always treasure.

My heartfelt thanks also go to the members of the thesis jury, Colige Alain, Galleni Moreno, Lassaux Patricia, Scherpereel Arnaud and Vincke Cécile for accepting to evaluate my work and for dedicating their time and expertise to this project.

We acknowledge the Robotein® platform of the BE Instruct-ERIC Centre for providing access to Bio-Layer Interferometry (BLI) equipment.

I am grateful to all the members of the MBPEL lab: to Deborah Palumbo, my “sister” and “mama mouche,” my shoulder to cry on, and the person with whom I shared so many beautiful moments, your happiness, your patience, and your amazing food brightened my days, even during the rainiest Belgian weather. Thank you for feeding me and bringing me so much good food, because clearly, I was not eating well enough. If I am still alive today, it is partly thanked to you.

I would also like to thank Petronie, who, despite occasional communication challenges due to our different languages, was always kind, full of energy, and ready to dance, a spirit that lifted my mood every single day.

My thanks go as well to all the zebrafish team: Chiara, Caroline, Colin, Colin “bébé,” Elisa, Laura, Manon, Románe. From the very beginning, you included me in every hangout, becoming not only colleagues but true friends. I was incredibly lucky to share the office with you. I will never forget our nights in the lab, working until 2 AM, it was exhausting, but also so much fun.

To all the LBTD group: Marie Julie, Alicia, Benedetta, Fabienne, Laura, Laurine, Maëlle, Marine, Marie-Laure, Perrine, Rebekha, thank you for helping me with thousands of experiments, for giving me constantly advices to improve my work, for all the flow cytometry and with the mouse model. Your support made this work possible. Thank you for including me in all the external activities such as restaurants. It made me feel less Italy and having a very good moment with you.

I would also like to thank all my friends, starting with the “Italians” which drove me from the Erasmus up to now, particularly: Benedetta, a person which I shared good and bad moments together, our coffee breaks were unforgettable, as like our Sanremo or movie nights. Gabriele, Giovanni, Paola, which before being a colleague she was a truly friend, with her capacity to find a solution even in the darkest spot, Valentina with her happiness and hyperactivity she brought light and energy could instantly change the mood of any day, but as well as Deborah, Lucia, Fulvio, Sharon, Benedetta. But as well a lot of international such as Gustavo, Claire for our night beers (you) and coke (me), our chill moment to speak and discuss about life problems, and Perrine which represented for me the lighthouse in the deepest night. Vorrei inoltre ringraziare i miei genitori per essermi sempre stati accanto, per tutti i sacrifici fatti e per aver sostenuto ogni mia scelta. Anche nella distanza, il loro affetto non è mai venuto meno.

And finally, to you, Ale, half friend, but truly the best one. You always believed in me, even when I struggled to believe in myself. You left this world far too early, but your presence has never left my life. Even though your atoms are now scattered across the universe, I will always carry you with me, in the deepest part of my heart.

ACKNOWLEDGEMENTS

Table of contents

Abstract

Abstract

Pleural mesothelioma (PM) is a highly aggressive cancer primarily caused by airborne asbestos exposure. Although the European Union’s asbestos ban has reduced incidence, PM remains a major clinical challenge. Current treatments, including chemotherapy with cisplatin and pemetrexed as well as immune checkpoint inhibitors, such as nivolumab and ipilimumab, have moderately improved survival. The overall prognosis remains therefore poor, and innovative therapeutic strategies are urgently needed.

Among potential molecular targets, the metalloprotease ADAM10 has emerged as a particularly promising candidate. ADAM10 is frequently overexpressed in PM and contributes to tumor progression, chemoresistance, and invasiveness. In PM, ADAM10-mediated cleavage of N-cadherin, a key adhesion molecule controlling cell–cell contacts and migration, releases an N-terminal fragment (NTF) that is thought to promote tumor cell progression. Inhibiting ADAM10 could therefore reduce N-cadherin shedding and impair PM progression. As an initial strategy, we used phage display to identify peptides inhibiting ADAM10. Using the NEB Ph.D. library, several candidate peptides were isolated and evaluated through *in silico* docking and enzymatic assays. One peptide exhibited partial inhibition of recombinant ADAM10 representing, to our knowledge, the first report of a phage-derived *in vitro* ADAM10 inhibitor peptide, although its inhibition capacity was limited. Given these modest effects, we next investigated the ADAM10 Prodomain, an endogenous inhibitor domain that maintains ADAM10 in its inactive zymogen state. Although the isolated prodomain suppresses ADAM10 catalytic activity, systemic inhibition of ADAM10 may cause adverse effects due to its essential physiological functions in healthy tissues. To achieve selective ADAM10 inhibition in PM, we engineered a Dual Targeting protein by fusing the ADAM10 Prodomain to an anti-mature mesothelin VHH (anti mMSLN VHH), a high-affinity single-domain antibody specific for the mature, membrane-bound mesothelin, a surface marker strongly expressed in epithelioid and biphasic subtypes of PM.

ABSTRACT

This construct binds mesothelin-positive tumor cells while locally inhibiting ADAM10 activity. Biochemical validation confirmed both mature mesothelin binding and ADAM10 inhibition, and its biological effects were assessed *in vitro* in PM cell lines.

Collectively, our findings provide the proof of concept of a dual targeting protein strategy combining VHH-mediated tumor specificity with endogenous ADAM10 inhibition. These results support the feasibility of targeted metalloprotease modulation PM to decrease cancerous cell migration and tumor progression.

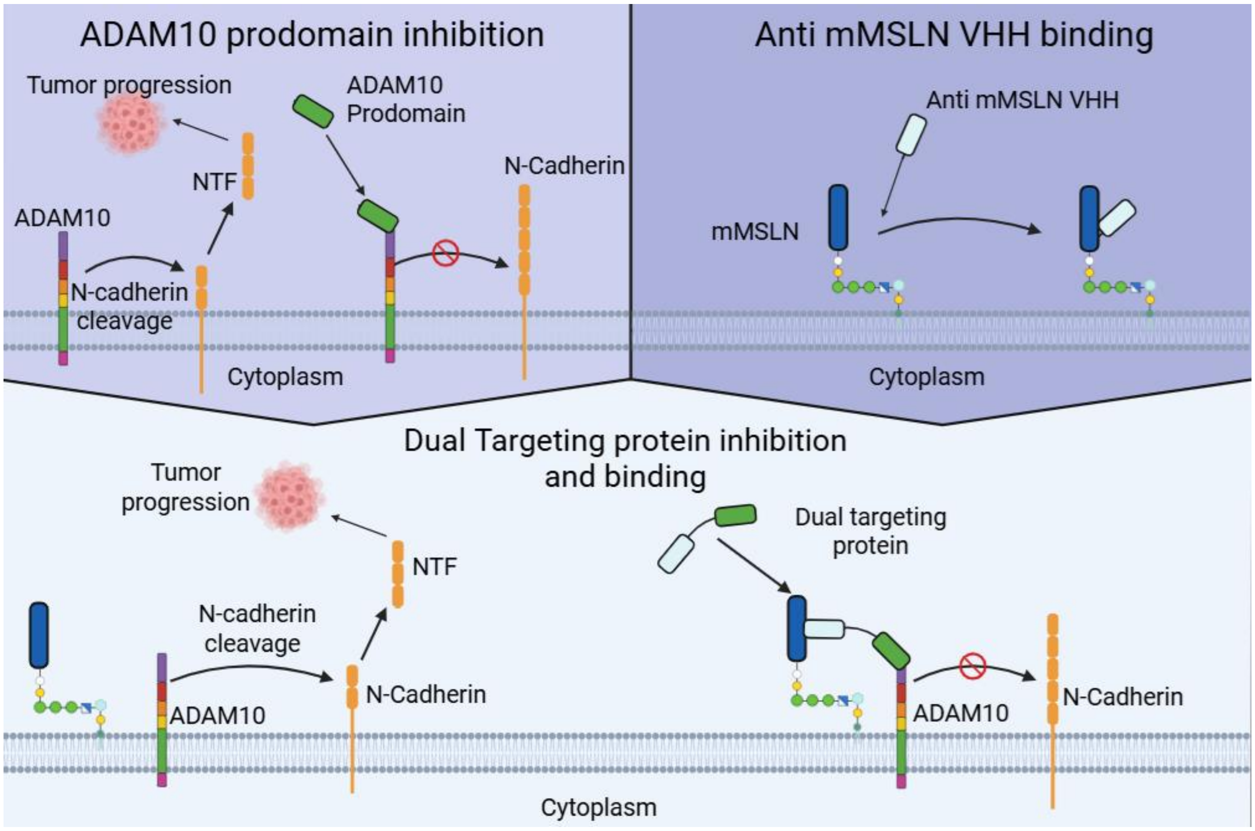

Figure 1) Schematic representation of the dual targeting protein therapeutic strategy developed in this work. *Top left: The ADAM10 prodomain inhibits ADAM10, preventing N-cadherin cleavage and the subsequent release of the N-terminal fragment (NTF), a process known to promote tumor progression in pleural mesothelioma (PM). Top right: anti mature mesothelin (mMSLN) VHH specifically binds mesothelin on the surface of PM cells. Bottom: The engineered dual targeting protein, composed of the ADAM10 prodomain fused to the anti mMSLN VHH, simultaneously binds mesothelin-expressing tumor cells and locally inhibits ADAM10 activity. This targeted inhibition reduces N-cadherin cleavage while minimizing off-target effects, providing a novel therapeutic approach for PM. This figure was created with BioRender.*

Abbreviations

Abbreviations

Abbreviations	Full Term
A1 VHH	Anti mMSLN VHH
ACS	American Chemical Society
ADAM	A Disintegrin And Metalloproteinase
ADAMDEC-1	A Disintegrin And Metalloproteinase Domain-Like Decysin-1
ADAMTS	ADAM with Thrombospondin Motifs
ADCC	Antibody-Dependent Cell-Mediated Cytotoxicity
APC	Antigen Presenting Cells
APP	Amyloid Precursor Protein
BACE	Beta-secretase 1
BAP1	BRCA1 Associated Protein 1
BCMA	B-Cell Maturation Antigen
BM	Biphasic Mesothelioma
CA-125	Mucin
CAR	Chimeric Antigen Receptor
CDKN2A	Cyclin Dependent Kinase Inhibitor 2A
CDR	Complementarity-determining region
CTLA-4	Cytotoxic T-Lymphocyte Antigen 4
CX3CL1	C-X3-C Motif Chemokine Ligand 1
CXCL16	C-X-C Motif Chemokine Ligand 16
CXCL2	C-X-C Motif Chemokine Ligand 2
DAMP	Damage Associated molecular Pattern molecules
DKK1	Dickkopf WNT Signaling Pathway Inhibitor 1
DM4	Ravtansine
EGCG	Epigallocatechin-3-gallate
EGF	Epidermal Growth Factor
ELISA	Enzyme-Linked Immunosorbent Assay
EPM	Epithelioid Malignant Pleural Mesothelioma
EMT	Epithelial-to-Mesenchymal Transition
ERK	Extracellular Signal-Regulated Kinase
FACS	Fluorescence-Activated Cell Sorting
FDA	Food and Drug Administration
FGFR	Fibroblast Growth Factor Receptor
GARFT	Glycinamide Ribonucleotide Formyl Transferase
GBM	Glioblastoma
HDAC1	Histone Deacetylase 1

HEGFR	Human Epidermal Growth Factor Receptor
HEAT	Huntingtin elongation factor 3 (EF3) Phosphatase 2A (PP2A) and the yeast kinase TOR1.
HMGB1	High Mobility Group Box 1
hMSLN	Human mesothelin
HPV	Human Papilloma Virus
IL	Interleukin
IPTG	Isopropyl β-D-1-ThioGalactopyranoside
JNK	c-Jun N-terminal Kinase
MHC	Major Histocompatibility Complex
MMP	Matrix Metalloproteinase
MPF	Megakaryocyte Potentiating Factor
PM	Malignant Pleural Mesothelioma
MRI	Magnetic Resonance Imaging
MSLN	Mesothelin
MTAP	Methylthioadenosine Phosphorylase
MTMMP	Membrane-type Metalloproteinase
MUC16	Mucin 16
NAD	Nicotinamide Adenine Dinucleotide
IgNAR	Immunoglobulin New Antigen Receptor
NKG2D/L	Natural Killer G2D/L
NLGN3	Neuroligin-3
NSCLC	Non-Small Cell Lung Carcinoma
NTF	N-Terminal Fragment
PABPN1	Polyadenylate Binding Protein 1
PCR	Polymerase Chain Reaction
PD-1	Programmed Death-1
PD-L1	Programmed Death-Ligand 1
PET-CT	Positron Emission Tomography–Computed Tomography
PI3K	Phosphoinositide 3-Kinases
PMDA	Japan’s Pharmaceuticals and Medical Devices Agency
RIP	Regulated Intramembrane Proteolysis
RNS	Reactive Nitrogen Species
ROS	Reactive Oxygen Species
rhmMSLN	Recombinant human mature mesothelin
SIRT1	Sirtuin 1
SLE	Systemic Lupus Erythematosus
SMM	Sarcomatoid Malignant Mesothelioma
SMRP	Soluble mesothelin related peptide
STAT3	Signal Transducer and Activator of Transcription 3

ABBREVIATIONS

SV40	Simian Virus 40
SVMP	Snake Venom Metalloproteinase
TACE	TNF-Alpha Converting Enzyme
TNBC	Triple Negative Breast Cancer
TNF	Tumor Necrosis Factor
TTP	Thrombotic Thrombocytopenic Purpura
TUP	Target-Unrelated Peptides
VH	Variabledomain of the heavy-chains of conventional IgGs
VHH	Variable Domain of Heavy Chain of Heavy-Chain-only Antibody
VL	Variable domain of the light chains of conventional IgGs
WHO	World Health Organization
WT	Wild Type

1 - Introduction

1- Introduction

1.1 Mesothelioma

The lung is a complex structure composed of airways, vasculature and interstitium, covered by an elastic serous membrane that forms the pleural cavity [Figure 2]. This cavity provides mechanical protection, a lubricated surface for lung movement during inspiration and expiration, and serves as immunological and metabolic active membrane involved in maintaining homeostasis and responding to pleural inflammation [1]. The pleura develops from the lateral plate mesoderm, which splits into somatic (parietal) and splanchnic (visceral) layers. The parietal pleura arises from the somatic mesoderm and lines the thoracic wall, while the visceral pleura arises from the splanchnic mesoderm and covers the lungs. This mesodermal origin accounts for the pleura's specific sensitivity and innervation, as well as the “mesothelium”, which are mesoderm-derived epithelial-like cells specialized for lubrication and transport [2]. The mesothelium is therefore a specialized monolayer of mesothelial cells supported by connective tissue, blood vessels, and lymphatics. This structure not only forms the pleura surrounding lungs but also lines other body cavities such as the peritoneum in the abdominopelvic region and pericardium around the heart [2]. Mesothelial cells which are the main component of the mesothelium play a dynamic role secreting surfactant-like molecules and release of pro- and anti-inflammatory mediators, synthesis of growth factors and extracellular matrix proteins to assist in pleural membrane repair [2].

1 - INTRODUCTION

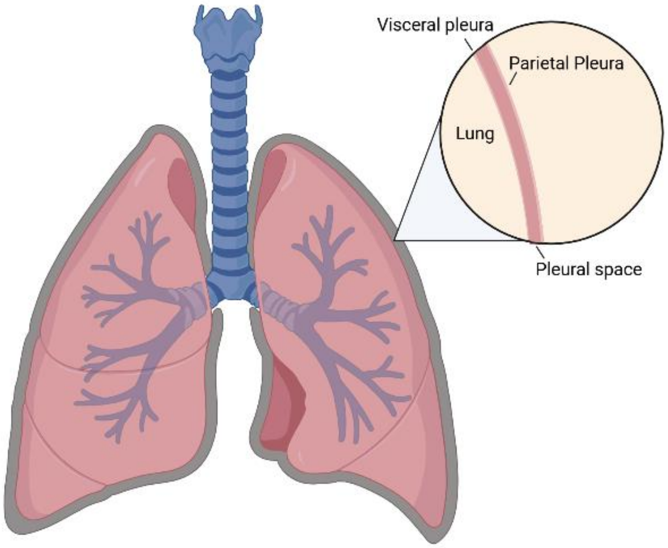

Figure 2) Schematic representation of the lungs and pleural membranes. The visceral pleura directly covers the lung surface, while the parietal pleura lines the thoracic cavity. The pleural space, located between the two layers, contains a thin layer of lubricating fluid that reduces friction during respiration. This image was created with BioRender.

Chronic exposure to asbestos, which can translocate from the pulmonary alveoli to the pleural space and whose fibers are resistant to degradation, causes pleural irritation. This irritation triggers cycles of proinflammatory repair, potentially leading to the development of mesothelioma [3]. Mesothelioma primarily arises in the pleura (73-85% of cases) and is usually referred to Pleural mesothelioma (PM). In less frequent cases, mesothelioma appears in the peritoneal (7-18% of cases) [Figure 3 A], pericardial cavities (1-2%) [Figure 3 B], and occasionally in the tunica vaginalis (<1%) [Figure 3 C] [4]. The World Health Organization (WHO) classifications traditionally recognizes three major subtypes of PM: epithelioid, biphasic, and sarcomatoid pleural mesothelioma [5]. These subtypes have an impact on prognosis and treatments of patients diagnosed with this tumor [6]. Despite advances in diagnosis and treatment, the median survival for patients with mesothelioma remains poor, averaging approximately of 9 months from initial diagnosis [7].

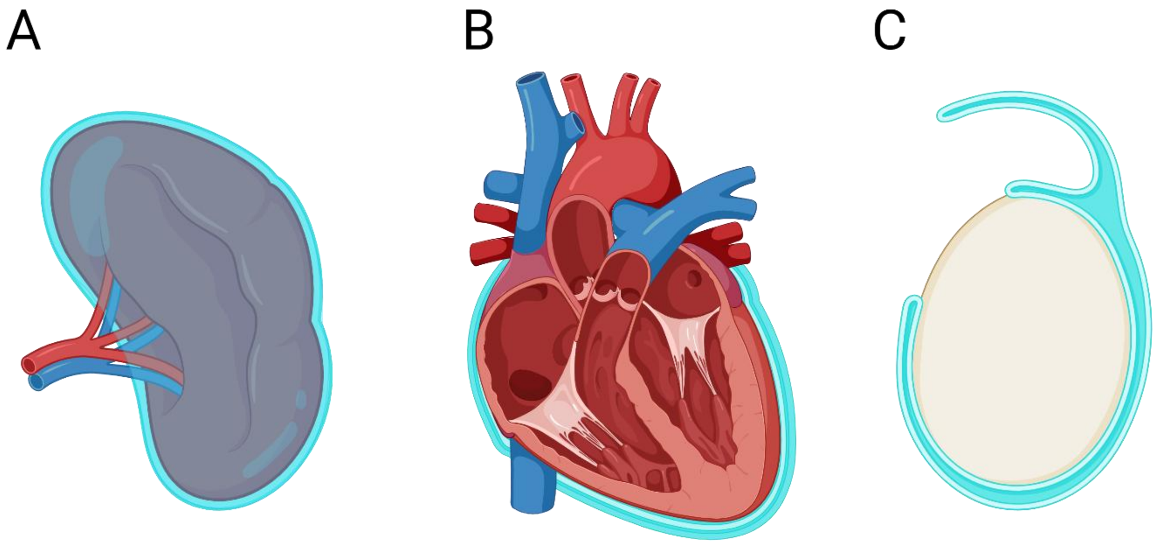

Figure 3) Schematic illustration of three serous membranes and the organs they envelop (light blue), all of which can give rise to mesothelioma. A) The peritoneum, the serous membrane of the abdominal cavity, covers and supports intraperitoneal organs such as the spleen. B) The pericardium, a double-layered serous membrane of the thoracic cavity, which surrounds and protects the heart. C) The tunica vaginalis, peritoneal derivative within the scrotum, forms the serous covering the testis. This image was created with BioRender.

1.1.1 Causes of Mesothelioma

The main causes of Mesothelioma include prolonged exposure to asbestos, genetic mutations, and infection with Simian Virus 40 (SV40). Among these, asbestos exposure is by far the most common and well-established risk factor. On the other hand, the role of DNA mutations and SV40 in Mesothelioma development are still under investigation.

1.1.2 The role of asbestos in PM development

Asbestos is a generic noun referring to six types of naturally occurring mineral fibers. The fibers belong to two groups: serpentines and amphiboles. The serpentine group contains only one mineral: chrysotile; while the amphibole group includes five asbestiform varieties: anthophyllite, grunerite (amosite), riebeckite (crocidolite), tremolite, and actinolite [8].

The first use of asbestos has been traced to Finland around 4700 BC, where anthophyllite were used to reinforce clay tools and potteries [9] but it was only in the nineteenth century that asbestos begun to be used in an industrial scale, in Italy, with the development of asbestos textiles [10]. At the beginning of the twentieth century, the demand of asbestos fibers grew, especially during the World War II due to its desirable properties: fire resistance, thermal stability, resistance to biodegradation, chemical inertia and low electrical conductivity [11]. Global asbestos extraction peaked in 1977 with 4.8 million tons decreasing to 1.3 million tons in 2023 [12].

Due to latency period, often exceeding 30 years [13], it is only in the 1960s that researchers established a correlation between worker's asbestos exposure and respiratory cancer diseases. Inhalation in a high concentration of both long asbestos fibers (more than 8 µm) and wide asbestos fibers (more than 0.25 µm) was associated with conditions such as asbestosis, lung cancer, benign pleurisy, pleural plaques and PM [13,14].

Due to its dangerousness, European Union member states banned five of the six types of asbestos in 1991, the use of chrysotile was also prohibited on January 1, 2005 [15]. Despite this significative reduction, asbestos fibers remain largely used in emerging economies such as Russia, Kazakhstan, China, Brazil and in developed country such as United Stated [12], which has not yet adapted a full nationwide ban.

1.1.3 Epidemiology

Three distinct "waves" of PM incidence have been identified: i) exposure related to mining, milling and transportation of raw asbestos (from 1920 up to 1980), ii) industrial use in manufacturing, insulation, shipping and carpentry (from 1950 up to 1980) iii) exposure during renovation or demolition of buildings containing asbestos (from 1980 up to today) [16–18].

During these waves, asbestos workers face a lifetime mesothelioma risk of approximately 10% and tobacco smoking further increased malignancy risk [19]. Family members were also affected due to their exposure to asbestos fibers brought home on clothes [19]. Indeed, although mesothelioma incidence rate is notably higher in men than women, primarily due to occupational asbestos exposure [20], women were also affected since they were cleaning clothes contaminated by asbestos fibers. According to Alpert *et al* [21] between 2008 and 2012, the incidence rate per 100,000 person was 0.9 for men and 0.3 for women in the U.S., and 1.7 for men and 0.4 for women across Europe. Additionally, mesothelioma is extremely rare in young individuals, with incidence typically rising between the ages of 50 and 60 years [19].

In Belgium, there is no asbestos mines, but the country became a major international manufacturer in the early 1900, as the Eternit group has developed factories in the country [22]. Between 1994-2008, Belgium had the fourth-highest number of PM deaths worldwide [22]. The age adjusted mortality rates for PM were 18.0 deaths per million for males and 3.1 deaths per million of females. These rate were about the double than the global averages, which stands at 9 deaths per million of males and 1.9 deaths per million of female [22]. According to the Belgian Cancer Registry, there were 311 new cases in 2022, with 51.8% of cases occurring in patients over 75 years old. Despite the improvements in diagnosis and treatments, most PM are still diagnosed at a late stage.

1.1.4 Inflammatory responses triggered by asbestos

Recent studies have shed light on how asbestos exposure leads to the transformation of human mesothelial cells. Different fibers have different carcinogenic properties: amphiboles (anthophyllite asbestos), grunerite asbestos (amosite), riebeckite asbestos (crocidolite), tremolite asbestos, and actinolite asbestos are more persistence in tissues, bringing a higher pathogenicity than serpentine fibers (chrysotile), which represents the most common fibers mined worldwide [23]. Despite being less carcinogenic due to its less persistence in tissues, serpentine fibers can still induce mesothelium cell transformation with chronic exposure.

Macrophages attempt to eliminate inhaled fibers through phagocytosis, but this is not possible since the length of asbestos fibers is too big, leading to 'frustrated phagocytosis'. This triggers the release of lysosomal content and cytotoxic effects, including intracellular oxidation, DNA damage, the release of reactive oxygen and nitrogen species (ROS and RNS), cell death, and carcinogenesis [3].

Understanding how asbestos induces malignant transformation has been challenging, because the fibers are highly cytotoxic and the entire cell population *in vitro* is wiped out within few days [24]. *In vitro* studies have shown that, asbestos fibers physically perforate the membranes and even the nuclei of mesothelial cells, suggesting a mechanical mechanism of DNA damage and potential oncogenesis [25].

Recent findings have also revealed a complex mechanism involving chronic inflammation triggered by the persistent presence of asbestos fibers. In mesothelium cells, asbestos exposure induces HMGB1 translocation from nucleus to the cytoplasm and in the extracellular environment. In the extracellular environment, HMBG1 leads to the production of TNF-α and macrophage inflammatory protein 2 (CXCL2). Altogether, these factors contribute to the chronic inflammatory process, recruiting immune cells such as monocytes, granulocytes and tissue macrophages. This chronic inflammatory microenvironment is a key driver of PM. The central role of HMGB1 in asbestos derived PM is supported by the evidence that inert mineral fibers do not elicit HMGB1 release, avoiding the chronic inflammation [26]. These findings are further confirmed by research showing that pharmacological inhibition of HMGB1 suppresses PM growth both in murine models and human cell lines [27].

Another driver of PM has been linked to the iron impurities present in asbestos. These impurities can catalyze the production of ROS leading to extensive DNA damage. Indeed, asbestos fibers induce necrotic cell death, which begins with lysosome-dependent cell death and after ferroptosis. The necrotic macrophages further exacerbate iron-dependent oxidative stress causing double strand DNA damage in mesothelial cells and promoting carcinogenesis [28].

1.1.5 Genetic mutations associated with PM

Genetic mutations can either trigger the appearance of PM or increase their incidence after asbestos inhalation [Figure 4]. BRCA1-associated protein 1 (BAP1) is a deubiquitylase which plays a critical role in chromatin remodeling and DNA repair in the nucleus [24]. When BAP1 is reduced or absent, Histone deacetylase 1 (HDAC1) becomes ubiquitylated and is degraded, leading to acetylation of HMGB1. This causes HMGB1 translocation into the extracellular space, promoting PM [24]. Indeed, extracellular HMGB1 acts as danger-associated molecular pattern (DAMP) that triggers chronic inflammation, cytokine release, and sustained cell survival and proliferation signaling therefore creating a pro-tumorigenic microenvironment. To support the importance of BAP1 in this mechanism, a mouse model carrying a heterozygous inactivating mutation of BAP1 has been developed and exhibits reduced DNA repair capacity and impaired cells death response to genetic damage [24,29].

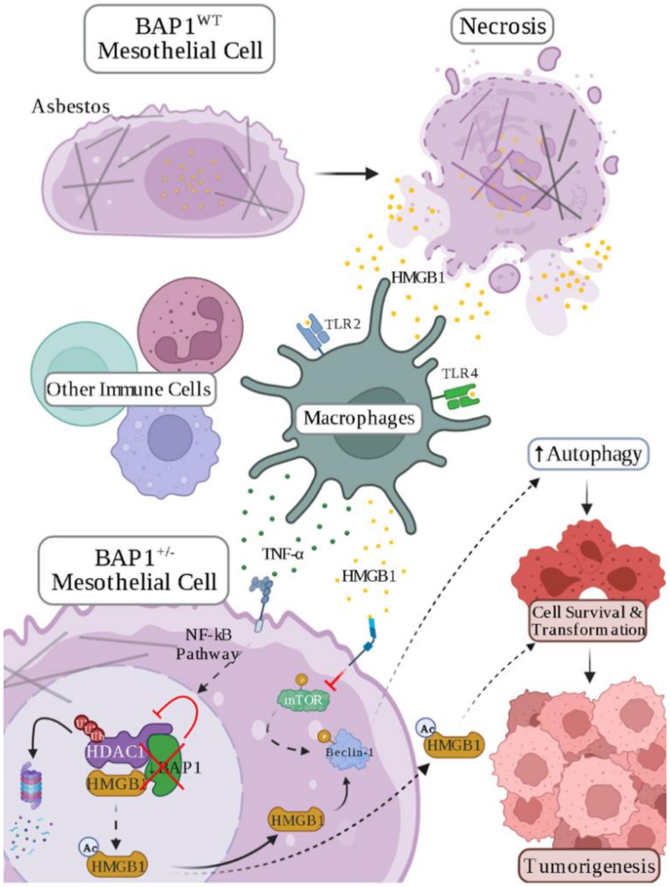

Figure 4) Asbestos exposure leads to the release of High Mobility Group Box 1 (HMGB1) from the nucleus into the extracellular space. Extracellular HMGB1 acts as a damage-associated molecular pattern (DAMP), recruiting macrophages and other immune cells. These macrophages produce additional HMGB1 and tumor necrosis factor-alpha (TNF-α), in order to promote a chronic inflammatory microenvironment. Prolonged inflammation can result to PM. Mesothelial cells with BAP1 mutations (BAP1$^{+/-}$), can bring a similar inflammatory pattern [24].

1.1.6 Simian Virus 40 involvement in PM appearance

Another potential cause of PM is the Simian Virus 40 (SV40). During the 1950s and 1960s, batches of inactivated polio vaccines produced using kidney cells from rhesus monkeys were contaminated with SV40. As a result more than 30 million of people in the USA may have been exposed to the active virus [30]. Although SV40 was found in other people who did not receive the contaminated vaccine, it was associated with PM and other cancers, due to its capacity to suppress the expression of tumor suppressor genes. The link between SV40 and PM is further supported by the evidence of SV40 DNA sequences have been found in up to 60% of human PM [30–32], suggesting a possible co-carcinogenic role alongside asbestos exposure. Other risks alongside asbestos and SV40 are associated to mutation caused by ionizing radiation (mainly therapeutic radiation), although it accounts for only a small proportion of the total cases [33,34].

1.1.7 Histological classification of PM

Different subtypes of invasive PM are recognized by the WHO: epithelioid, biphasic, and sarcomatoid. Furthermore, a preinvasive mesothelial tumor form, known as PM *in situ*, is primarily associated with the BAP1 mutation.

Initially, PM *in situ* was described morphologically as a single layer of small papillary projections of atypical mesothelial cells on the pleural surface [5]. Later, Churg *et al* [35] identified its association with BAP1 loss and/or cyclin-dependent kinase inhibitor 2A (CDKN2A) homozygous deletion in patient without evidence of tumor on imaging. Other genetic alterations are currently unknown in PM but BAP1 and CDKN2A loss occur in up to 70% of cases. Identifying the *in situ* PM is important since after a median follow up of 5 years, up to 70% of PM *in situ* progress into the invasive form [36].

Among the various forms of PM, several histological subtypes can be identified. Epithelioid PM (EPM) is the most common, accounting for up to 80% of all PM cases. It is characterized by a diffuse and invasive growth pattern of epithelioid cells originating from pleural surface and it can exhibit a high morphological heterogeneity. According to the 2015 WHO classification, trabecular and tubule-papillary patterns in the EPM are associates with a more favorable prognostic compared to other patterns within the epithelioid subtype [37,38]. Due to the difficulty in classifying EPM, the European reference Network on Rare Adult cancers (EURACAN) and the International Association for the Study of Lung Cancer (IASLC) have proposed a new histological classification for PM, dividing it into the following categories: tubular, papillary, tubule-papillary, trabecular, solid, micropapillary, adenomatoid, microcystic, pleomorphic and transitional. Additionally, other characteristics such as rhabdoid, small cell, clear cell, signet ring cell, are considered cytological features, which further complicate the diagnosis [39] .

Sarcomatoid Pleural Mesothelioma (SPM) is a rare subtype, comprising less than 10% of cases. It is characterized by a diffuse and infiltrative growth of spindle cells, or mesenchymal appearing cells. It usually presents no pleural effusion and has often more distant metastases. Diagnosis clues include pronounced atypia of tumor cells, necrosis and invasion. Prognosis is extremely poor, untreated patients with SPM die within 5-6 months [37].

Biphasic Pleural Mesothelioma (BPM) is characterized by at least 10% of epithelioid or sarcomatoid components. Prognosis lies between pure epithelioid and sarcomatoid PM. Biphasic patients with a large epithelioid component may benefit from surgery, while patients with a large component of sarcomatoid features do not. It has been demonstrated that patients with less than 50% of epithelioid components have a poor survival of around 6.6 months compared to the one with more than 50% of around 11.8 months. Diagnosis of BPM is challenging due to the difficulty in confirming the malignant spindle cell component. BAP1 loss and CDKN2A/p16 homozygous deletion can aid in distinguishing biphasic cases [37].

1.1.8 Staging of PM

According to the American Cancer society, four stages of PM are described. These stages are defined by the tumor size and extent, the spread to nearby lymph nodes and the metastasis to distant sites [40]. The stages range from I to IV, with lower numbers indicating cancer that has spread less extensively. Staging is crucial for determining the most appropriate treatment and predicting the likely outcome.

Stage I: Cancer cells are present in the pleura lining the chest wall on only one side. The average pleural thickness, calculated at three different locations, does not exceed 12 mm. The tumor has not spread to the nearby lymph nodes, and no distant metastases are visible.

Stage II: Cancer is still present in the pleura lining the chest wall on only one side. The total pleural thickness doesn’t have to exceed 30 mm or 12 mm if the tumor involves the fissure or the mediastinum. Cancer may have spread to nearby lymph nodes, but no distant metastases are present.

In stage III A, PM is confined to the pleura lining on one side of the chest, with a total thickness not exceeding 30 mm. It may involve the fissures, the mediastinal fat, and regional lymph nodes on the same side as the primary tumor. No distant metastases are visible.

In stage III B, the tumor is considered unresectable due to extensive local invasion. It may have invaded a rib, a mediastinal organ, the diaphragm, the contralateral pleura or the pericardium. The cancer may or not have spread to nearby lymph nodes but no distant metastases are present.

Stage IV: Cancer may or may not have invaded the nearby structure and lymph nodes, but distant metastases are present. These may involve organs such as bones, liver or peritoneum.

1.1.9 Diagnostic tools and biomarkers for PM

Despite the fact the PM symptoms are non-specific and that they overlap with those of other respiratory diseases, most patients commonly experience breathlessness, chest pain, weight loss and fatigue. Shortness of breath is typically caused by pleural effusion and intrathoracic tumor growth, while chest pain may result from tumor invasion of chest wall, potentially causing bone pain. Due to the non-specific nature of these symptoms and the long latency period, often exceeding 30 years [13], PM is usually diagnosed later in life, with a mean age of 74 years at the time of diagnosis [41]. Consequently, early diagnosis is essential for improving patient outcome and initial diagnosis evaluation includes chest X-ray to investigate the pleural effusion. However, due to the low sensitivity of this technique, thoracic ultrasounds, PET-CT scan or MRI are generally preferred. These techniques provide better visualization of pleural fluid volume, effusion and lesions of the pleura. When imaging is inconclusive, invasive procedures become necessary to evaluate mediastinal involvement and peritoneal invasion [42].

Obtaining confirmation of the PM diagnosis by histological evaluation is crucial. Biopsies are studied by standard staining and immunohistochemistry that help to determine the PM subtype and to distinguish it from metastasis of other malignancies that would reach the pleura [42]. Since tissues morphology alone is not sufficient, several biomarkers are studied by immunohistochemistry, such as mesothelin, BAP-1 protein loss or S-methyl-5'-thioadenosine phosphorylase (MTAP) expression.

In addition, other biomarkers support the diagnosis and offer insights into the biology of tumor. This includes serum mesothelin-related protein which is elevated in 84% of patients. It is associated with epithelioid and biphasic subtypes and plays a role in enhancing tumor cell adhesion. Additional blood markers includes: osteopontin, a phosphoprotein containing an arginine-glycine-aspartic acid motif that mediates integrin binding and promotes tumor cell migration and invasion [43]. Vimentin, a marker of epithelial–mesenchymal transition associated with tumor progression and more aggressive phenotypes [44,45,46]. Elevated plasma levels of MUC16 (CA-125), CA15-3 and hyaluronic acid have also been found in PM cancers suggesting that they can be used as biomarker [42].

1.1.10 Therapeutic approaches for PM

Pleural mesothelioma treatment is primarily guided by staging, histologic subtypes and patient's overall clinical condition [47]. Although several therapeutic treatments have been explored over the years, including surgery, radiotherapy, chemotherapy and immunotherapy, the efficacy of a systemic anticancer therapy against PM remains limited. Nonetheless, growing interest in immunotherapy, particularly the immune checkpoint inhibitors has brought new advancements into PM management [48].

Historically, radiotherapy was used as prophylactic treatment to prevent chest-wall invasion and metastasis; several studies have however shown that they provide no benefits in this context [47,49]. Today, radiotherapy plays an important role as adjuvant, neoadjuvant or palliative treatment, and modern techniques focus on minimizing the radiation doses reaching the surrounding tissues like heart and contralateral lung. In the palliative setting, the radiotherapy is commonly used for symptomatic relief in cases of tumor invasion into the chest wall or spine, spinal cord compression, or other obstructive symptoms [50].

Another treatment is the surgery, which aims to achieve a macroscopic complete resection often in combination with other therapies such as chemotherapy and radiotherapy [51]. The most commonly used surgical techniques are pleurectomy decortication or the extended pleurectomy decortication, which are associated with a low rate of mortality and morbidity compared to other surgical methods [52]. Many patients with PM are found to have unresectable diseases, and only 60%-80% are eligible for complete resection. The length of overall median survival remains around 24 months despite some improvements related to the use of radiation therapy before extra pleural pneumonectomy that has shown a median overall survival of 66 months in selected patients with the epithelioid histology [49]. Given the poor overall prognosis, it is obvious that other treatments must be investigated to improve outcomes. Chemotherapy remains one of the most used treatments. The EMPHACIS trial demonstrated that the combination of cisplatin and pemetrexed significantly improved median overall survival from 9.3 months (cisplatin alone) to 14.1 months (cisplatin and pemetrexed combined) [53]. Cisplatin is a cytotoxic platinum-based drug belonging to the class of alkylating agents used to treat solid tumors and hematologic malignancies. Its toxicity is due to its covalent binding of platinum to the guanine and adenine DNA bases, which leads to strand breaks [54]. Damaged DNA block cell cycle and triggers cell death. Moreover cisplatin is particularly effective at targeting rapidly dividing cells while it is less useful for slow growing tumors [54]. Pemetrexed is an antifolate agent that inhibits key enzymes involved in pyrimidine and purine synthesis such as thymidylate synthase [55], a folate-dependent enzyme which catalyzes the transformation of deoxy uridine monophosphate to deoxythymidine monophosphate. In addition, pemetrexed inhibits dihydrofolate reductase, which is an enzyme involved in the reduction and activation of the folic acid, as well as the glycinamide ribonucleotide formyl transferase (GARFT) which is involved in purine synthesis [55]. Another antifolate, raltitrexed combined with cisplatin, has also shown improved efficacy compared to cisplatin alone, further supporting the idea of using an antifolate treatment against PM [56].

In other studies, the chemotherapy treatments were often associated with other molecules or antibodies such as bevacizumab, a monoclonal antibody against vascular endothelial growth factor A, which has been shown an increased antitumoral effect by inhibiting the angiogenesis and tumor proliferation [57,58]. Similarly, other tyrosine kinase inhibitors such as Nintedanib [59] and Cediranib [60,61], inhibit vascular endothelial growth receptors 1-3 (VEGFR) [62] signaling pathway, suppressing angiogenesis and tumor growth have been evaluated in combination with cisplatin and pemetrexed. These combinations have increased the overall survival of around 2 months compared to the control group treated with Cisplatin and Pemetrexed only [60,63,64].

Immunotherapy has emerged as a promising alternative for PM, particularly following the results of the CheckMate 743 trial [48], which compared the combination of ipilimumab and nivolumab with the standard cisplatin-pemetrexed chemotherapy in treatment-naïve patients [48]. Immunotherapy achieved an overall median survival of 18.1 months compared with 14.1 months for chemotherapy. Ipilimumab (Yervoy) is a high affinity monoclonal antibody that targets CTLA-4, a negative regulator of T-cell activation. By blocking CTLA-4 signaling, ipilimumab enhances T-Cell activation and promotes antitumor immunity [65]. Because CTLA-4 plays a pivotal role in downregulating T-cell responses, it represents a key targeting immune checkpoint blockade therapy [65]. Nivolumab, on the other hand, is a fully human IgG4 monoclonal antibody directed against PD-1 (Programmed Death-1), another immune checkpoint receptor. PD-1 is a checkpoint receptor known to suppress T-cell activity upon binding to PD-L1/2. Inhibiting PD-1 restores T-cell function allowing an effective antitumor immune response [65].

Among these therapeutic strategies, increasing attention has been directed toward targeting tumor-specific antigens. One such emerging target is A Disintegrin and Metalloproteinase 10 (ADAM10), a transmembrane metalloprotease implicated in tumor progression, including PM [66].

1.2 A Disintegrin and Metalloproteinase 10 (ADAM10)

ADAM10 is a member of the ADAMs family, a group of transmembrane and secreted proteins. The terms ADAM standing for “A Disintegrin And Metalloproteinase”, reflects their modular construction. It also alludes to the initial characterization of proteins members in the snake venom with the acronym associated with fertility due to their presence in sperm proteins [67]. Functionally ADAM10 acts as a major sheddase, cleaving the ectodomains of numerous substrates, including Notch, N-cadherin, E-cadherin, Epidermal Growth Factor Receptor ligands, and Amyloid Precursor Protein (APP) [68]. Through these activities, ADAM10 regulates key processes such as cell-adhesion, synaptic maturation, and regulated intramembrane proteolysis (RIP). In cancer, ADAM10 is frequently upregulated and contributes to tumor progression, proliferation and drug resistance, through multiple mechanisms. Elevated ADAM10 expression has been reported in several cancers, including glioblastoma, breast cancer, ovarian cancer, and PM [66,69].

1.2.1 ADAMs family: structure and classification

Proteins of the ADAMs family have been identified in a broad range of species, from the nematode *Caenorhabditis elegans* to the vertebrates [70]. They are, however, absent in plants. A total of 38 members of the ADAM proteins has been identified across species. In human, the genome encodes 25 ADAM genes with 4 pseudogenes, while mouse and rat have 37 and 34 ADAM genes, respectively [71]. Within the 21 presumed functional human ADAMs, 13 encode proteases with the reprolysin-type active site (HEXGHXXGXXHD).

According to the MEROPS database classification (https://www.ebi.ac.uk/merops/), ADAMs proteins belong to the M12B, adamalysin protease subfamily, alongside Matrix Metalloproteinases (MMPs), membrane-type metalloproteinases (MTMMPs), A Disintegrin And Metalloproteinase with Thrombospondin motifs (ADAMTSs) and venom metalloproteinases (SVMPs) [72].

ADAMs, MMPs, ADAMTSs, MTMMP, and SVMPs all possess a N-terminal signal peptide that directs their secretion. These proteins also contain a prodomain that acts as an intramolecular chaperone facilitating correct folding and maintaining enzyme latency via a cysteine-switch mechanism [73]. This prodomain is cleaved intracellularly during its transit through the Golgi system either by autocatalytic cleavage (e.g. ADAM8 and ADAM28) or by pro-protein convertases [74,75]. Following the prodomain is the metalloproteinase (MP) domain, which serves as catalytic core of ADAMs family. Structural differences between families begin at this point [Figure 5]. Interestingly, ADAMs, ADAMTSs and SVMPs contain a disintegrin-like domain which is absent in MMPs and MTMMPs; this domain resembles a protein found in hemorrhagic snake venom that binds platelet integrin αIIbβIIIa, blocking their aggregation, while the adjacent cysteine-rich domain contributes to substrate recognition and binding [76]. Many ADAM proteins have the Epidermal Growth Factor (EGF) like domain although ADAM10 and ADAM17 contains only a small EGF like motif [77]. The structure ends with a transmembrane domain followed by a cytoplasmic tail, whose length and sequence vary among ADAM family members.

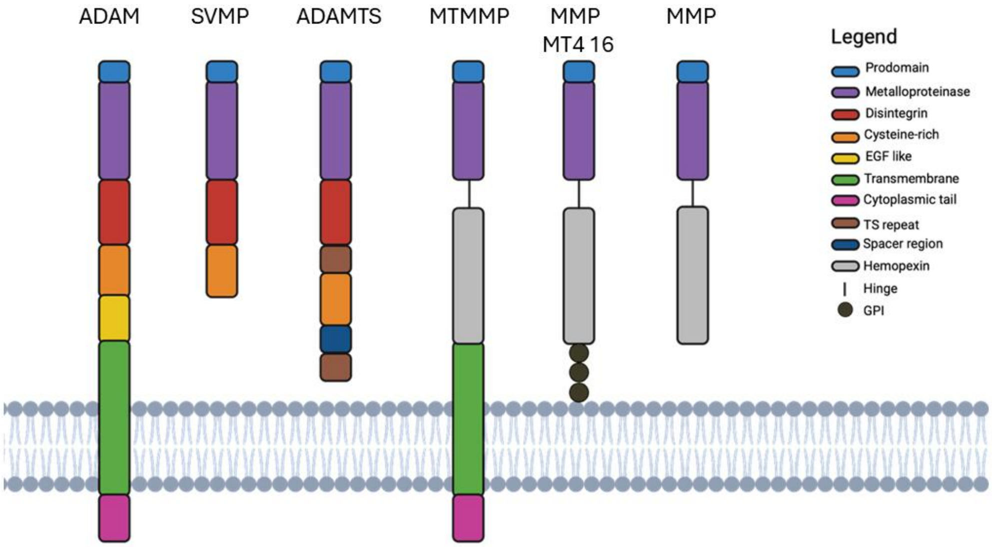

Figure 5) Illustration of the structural organization of five metalloproteinase families: ADAM, SVMP, ADAMTS, MTMMP, and MMP. Notably, MT4-MMP and MT16-MMP are GPI-anchored rather than containing a transmembrane domain. Each protein structure is represented as a linear sequence of domains, color-coded according to their functional regions. The color code is illustrated on the figure. A double-layered cell membrane is depicted at the bottom of the diagram to indicate membrane-associated proteins. This comparative visualization highlights the diversity and modularity of domain arrangements across these protein families, reflecting their distinct biological roles and mechanisms of action. This image was created with BioRender.

Not all the human ADAM proteins are catalytically active. The active ADAMs are ADAMDEC-1, ADAM-8, -9, -10, -12, -15, -17, -19, -20, -21, -28, -30 and -33. Inactive ADAMs are ADAM-2, -7, -11, -18, -22, -23, -29 and -32 in which the metalloproteinase domain could play a role in folding or protein-protein interaction. ADAM proteins participate in several physiological processes, including sperm-egg interaction, cell fate determination in the nervous system, muscle development, immunity and cell migration [68]. One interesting example is ADAM17 (also known as TACE) which cleaves pro-TNFα, playing essential roles in immune and inflammatory response and development. Among all the ADAM proteins, ADAM10 is the protein which is mainly important for our study for its role in PM [66].

1.2.2 Structural features of ADAM10

ADAM10 is a transmembrane metalloprotease encoded by a gene located on chromosome 15q21.3. It comprises 16 exons and produces an mRNA transcript of 3,410bp. Like other members of the ADAM family, ADAM10 is synthesized as a catalytically inactive precursor, as its prodomain maintains the enzyme in a latent state. ADAM10 plays a critical role in developmental signaling and is implicated in various pathological processes including cancer.

ADAM10's modular structure includes an N-terminal signal peptide, a prodomain, metalloproteinase domain, disintegrin domain, cysteine-rich domain, EGF like motif, a transmembrane domain and a cytoplasmic tail [76] [Figure 6].

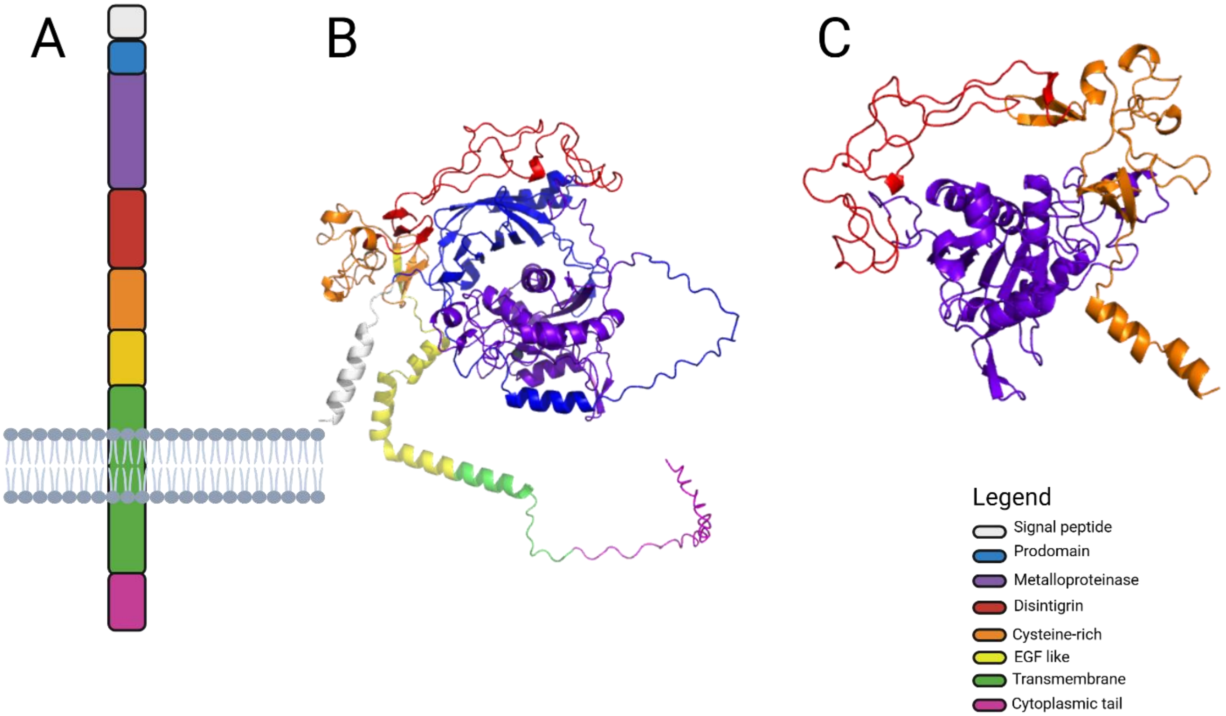

Figure 6) Representation of ADAM10 metalloproteinase. A) A schematic diagram illustrating the domain architecture of the protein transmembrane in the cell membrane, with each domain distinctly color-coded. B) A 3D model of the ADAM10, shown as ribbon, and predicted with Alphafold 3.0. The same color scheme is used in both panels as shown on the figure. C) Experimentally determined 3D structure of the ADAM10 extracellular domain (PDB:6BE6). The images are created with Biorender and Pymol.

The full-length ADAM10 precursor is catalytically inactive until the prodomain is cleaved off [76]. Comparative structural analysis between ADAM10 and its non-catalytic homolog ADAM22 (PDB 3G5C), the only available ectodomain experimental structure of a non-catalytic ADAM, highlight differences in domain arrangement [Figure 7]. Despite individual domains are structurally similar between the two ADAMs, the superimposition structure shows distinct structural organization, suggesting that ADAM family members may structurally differ significantly [76]. The catalytic domain of ADAM10 is anchored by a five-stranded β-sheets, on the edge of which lies the active site cleft. Below the cleft there is a central helix, known as the "base" of active site which includes the conserved HEXXH motif [Figure 8]. Three histidine residues (His383, His387 and His393) coordinate the zinc ion, which is essential for catalysis, while the glutamate residue (Glu384) participates in the acid/base catalysis.

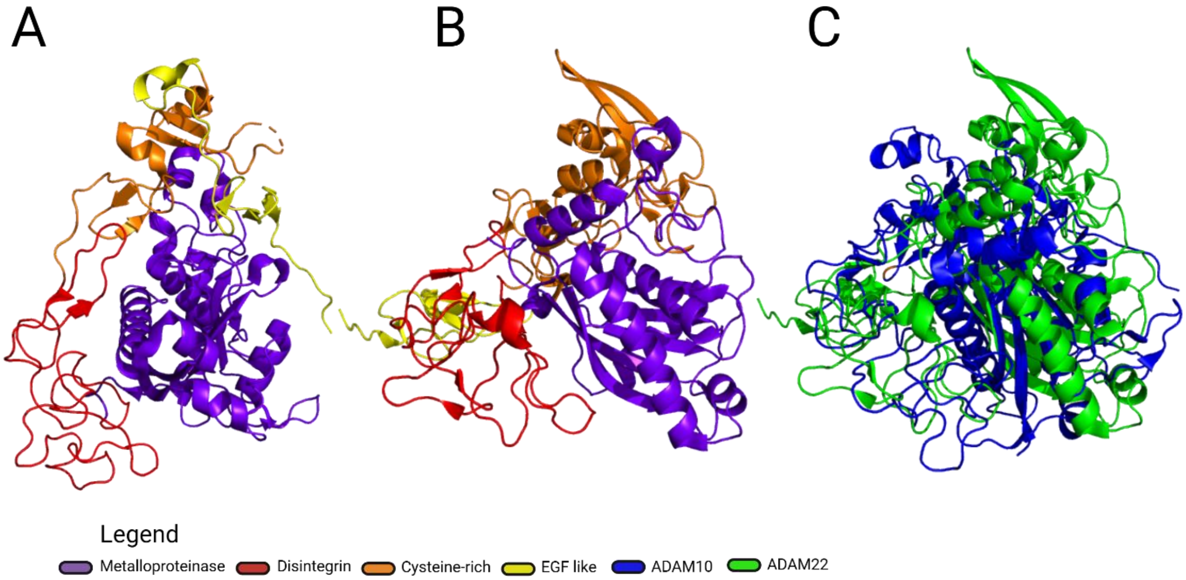

Figure 7) Structural comparison of ADAM10 and ADAM22. A) Ribbon representation of ADAM10 (PDB: 6BE6) each color represents a different domain B) Ribbon representation of ADAM22 (PDB:3G5C), each domain is shown with a different color. C) ADAM10 and ADAM22 superimposition. Despite belonging to the same ADAM family, the two metalloproteases display substantial domain arrangement divergence with a calculated root-mean-square of approximately 19Å across aligned Cα atoms. The image was created with Pymol and BioRender.

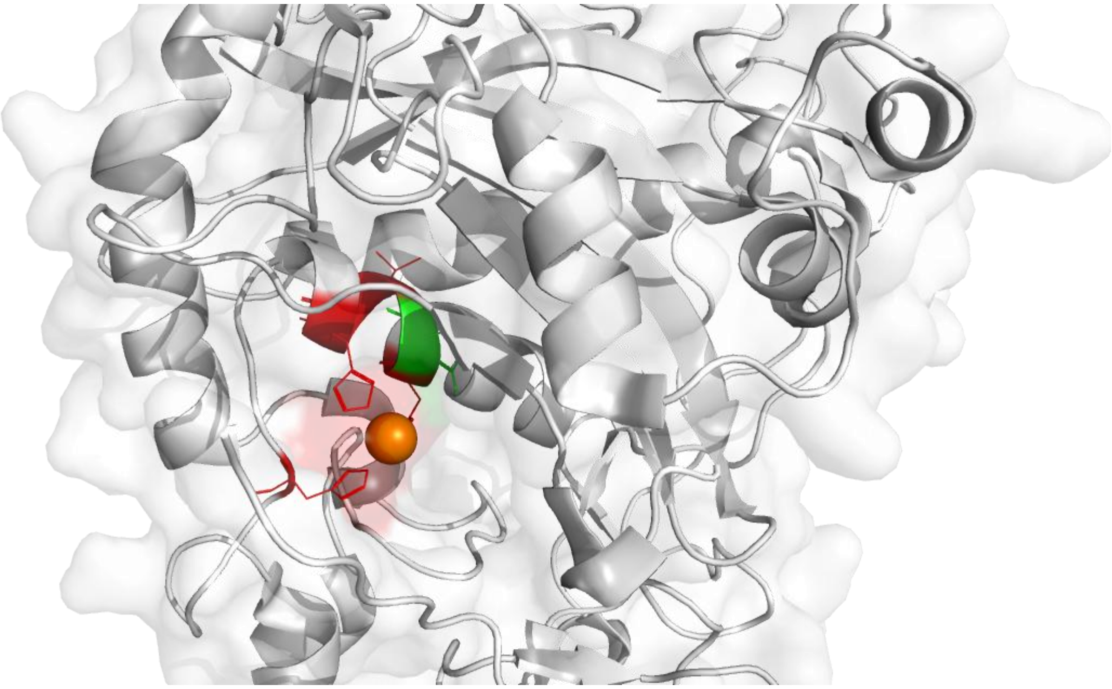

Figure 8) Structure of the catalytic domain of ADAM10 metalloprotease. The zinc ion (orange) is coordinated by His383 and His387 belonging to the HEXXH helix and His393 in the adjacent loop (red). The Glu384 (green) in the HEXXH helix is the catalytic residue, participating in substrate cleavage. Image created with Pymol.

Substrate selectivity of ADAM10 is determined by three main pockets refer to as P1, P2 and P3 [Figure 9]. P1 is the most important pocket which has a strong affinity for hydrophobic residues [76,78] and it is defined by Val376, Ile379, Thr380, Ile416 and Thr422 [76]. The P2 pocket is poorly defined and form hydrogen bonds between Leu654 and Ala331. In contrast, the P3 pocket is defined by Leu301, Leu330 and Trp332 and shows a preference for proline and hydrophobic residues [76].

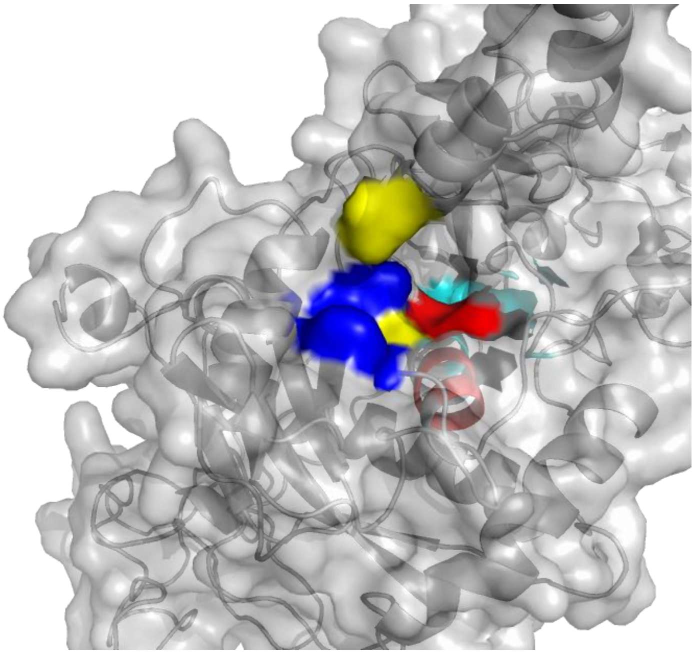

Figure 9) Substrate-binding pockets of ADAM10 metalloprotease. The P1 pocket (blue) shows strong affinity for hydrophobic residues and it is defined by residues Val376, Ile379, Thr380, Ile416, Thr422. The P2 pocket (cyan) is poorly defined, and it's described by Leu654 and Ala331. The P3 pocket (yellow) is defined by Leu301, Leu330 and Trp332. The HEXXH active site is in red. Image created with PyMol.

Early studies by Pan and Rubin have suggested that the disintegrin and cysteine rich domain might have an autoregulatory role inhibiting the metalloproteinase activity in the absence of a substrate [79]. This hypothesis was further supported by Seegar *et al* [76], who demonstrated that ADAM10 extracellular domain adopts a compact arrowhead conformation in which the disintegrin and cysteine-rich domain envelop the metalloproteinase domain [76]. This autoinhibited conformation limits substrate access to the P1 and P2 pockets, reducing the enzyme activity. This inhibitory effect has been observed in both Notch signaling and APP shedding assays, reinforcing the hypothesis of the modulatory effect on enzyme function [76] [Figure 10].

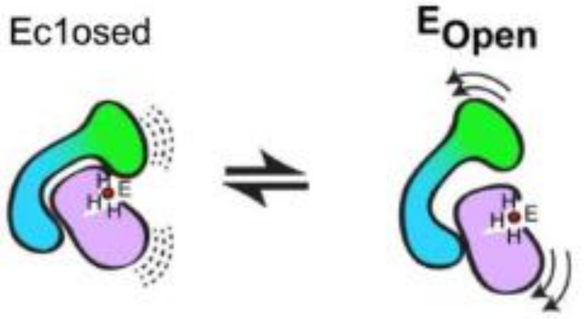

Figure 10) ADAM10 can adopt two structural states: a closed conformation ("Ec1osed") as shown on the left and an open conformation ("EOpen") shown on the right. In the closed conformation, the disintegrin domain and cysteine rich domain (green and blue) closes the metalloproteinase domains (purple). In the open state, the green domain reveals an open conformation allowing the accessibility to the catalytic domain. This figure was originally published in Seegar et al [76].

1.2.3 Biological functions and mechanism of action of ADAM10

ADAM10 can cleave more than 50 different transmembrane proteins, ranging from adhesion molecules to proteins involved in cell-to-cell communication, thus controlling a vast variety of biological processes [Annex1-Table]. ADAM10 is a central mediator of Regulated Intramembrane Proteolysis (RIP), a mechanism crucial for maintaining the transmembrane proteins turnover and transmitting intracellular signals. During RIP, ADAM10 initiates the process by the ectodomain shedding of one of a transmembrane protein such as Notch and releases the extracellular portion of the target protein. The membrane bound fragment is subsequently cleaved by a γ-secretase which releases the intracellular domain that is translocated to the nucleus and acts as a transcription factor, regulating gene expression. ADAM10 dependent Notch cleavage facilitates downstream signaling pathways involved in proliferation, differentiation and cell fate determination [80]. Thus, ADAM10 is essential for the development, and knockout mice exhibit early embryonic lethality, highlighting its critical developmental role [81].

ADAM10 has been implicated in a wide range of diseases, with extensive research highlighting its role in both neurological and immunological disorders. In the nervous system, ADAM10 is crucial for neurogenesis, neuronal migration, axon sprouting, primarily through the cleavage of ephrin and ephrin receptors, neural glial-related cell adhesion molecule, and other substrates [82,83].

One of the most well-known substrates is the amyloid precursor protein (APP), which is central to Alzheimer's disease pathology. Under pathological conditions, APP is cleaved by β-secretase (BACE), initiating the amyloidogenic pathway and generating a membrane-anchored C terminal fragment. This latter is further processed by a γ-secretase releasing the APP intracellular domain and the neurotoxic Aβ peptide, which accumulates extracellularly and drives the amyloid cascade. ADAM10 competes with BACE1 for APP cleavage, generating shorter fragments which does not produce the Aβ peptide and then having a protective role [82].

ADAM10 also contributes to protect from prion disease by shedding the cellular prion protein (PrPc) and thereby preventing its conformational conversion into the pathological misfolded form (PrPsc) [84]. Additionally, excess cleavage of N-cadherin is correlated with synapses loss, and its pharmacological inhibition has been observed to rescue the synaptic function [82].

Beyond the nervous system, ADAM10 is highly expressed in other tissues like bone marrow and lymphoid tissues and is involved in other important disorders such as rheumatoid arthritis (RA), psoriasis, systemic lupus erythematous (SLE) and atherosclerosis.

In rheumatoid arthritis, a chronic inflammatory disease affecting synovial joints [69], ADAM10 contributes to disease progression through multiple mechanisms. It facilitates the shedding of the low-affinity IgE receptor CD23 [85], producing a soluble form which activates the immune cells and stimulates the release of TNF-α and other pro-inflammatory cytokines contributing to the disease. ADAM10 can also cleave adhesion molecules JAM-A and JAM-C or chemokines CXCL16 and CX3CL1, which enhance the infiltration of immune cells and inflammatory processes. Indeed, ADAM10 and CXCL16 are upregulated in synovial joint biopsies from rheumatoid arthritis patients, particularly in synovial macrophages, where their co-expression sustains local inflammatory processes. Knockdown of ADAM10 suppressed the release of proinflammatory cytokines TNF-α, IL-6 and IL-8 [69].

In psoriasis, an inflammatory disease characterized by hyperproliferative lesions of the skin associated to aberrant keratinocyte differentiation [69], ADAM10 plays a central role through its regulation of the Notch signaling pathway in keratinocyte maturation. Deletion of ADAM10 in adult mice results in the hyperproliferation of keratinocytes and defective differentiation. Consequently, ADAM10 activators such as acitretin, a retinoid used in psoriasis treatment, have been shown to restore normal keratinocyte behavior via upregulation of ADAM10 [86].

1.2.4 The role of ADAM10 in cancer progression

ADAM10 has been implicated in the progression of various cancers due to its ability to cleave multiple substrates [Table 1]. In glioblastoma (GBM), ADAM10 is negatively correlated with the patient prognosis, enhancing cell migration and invasion through the shedding of adhesion molecules such as L1CAM and N-cadherin [69,87]. Treatment with the anti-ADAM10 inhibitory antibody AB19026 (Millipore) reduces the tumor growth and migration by blocking N-cadherin cleavage [87]. Another mechanism involves neuroligin-3 (NLGN3), a synaptic protein released via ADAM10 cleavage, which promotes glioma proliferation by activating the PI3K-mTOR pathway and inducing oncogenic gene expression via focal adhesion kinase (FAK) glioma proliferation [69]. This mechanism was confirmed by ADAM10 inhibitors GI254023X and INCB7839, which have shown efficacy in reducing GBM cell growth in preclinical mouse models [88]. Furthermore, ADAM10 mediates the release of the heat shock protein 90α (Hsp90α), a potential pan-cancer biomarker and its inhibition with GI254023X reduces Hsp90α secretion in tumor cell lines [89]. Interestingly, high ADAM10 levels have been positively correlated with poor clinical outcomes, including increased metastasis, disease-free survival and overall survival [90].

In human non-small cell lung-carcinoma (NSCLC), elevated ADAM10 levels in both primary tumor tissues and circulating exosomes have been proposed as a prognostic biomarker and tool for early detection and disease monitoring [91].

In breast cancer, ADAM10 contributes to tumor progression via two mechanisms. In HER2+, which approximately represents 10-20% of all invasive ductal mammary carcinomas, ADAM10 sheds HER2 into the extracellular space, reducing trastuzumab efficacy of binding [92]. Treatment with the ADAM10 inhibitor INCB8765 increases sensitivity to trastuzumab *in vitro*, and restores responsiveness in trastuzumab-resistant cells [Table 1] [93]. Although both ADAM10 and ADAM17 are expressed in the majority of triple negative breast cancer, a subtype characterized by the absence of the HER2 expression, ADAM10 inhibition has been shown to reduce cell migration and cancer invasiveness [69,94]. Furthermore, ADAM10 has been proposed to have a role in regulating the PD-1/PD-L1 immune checkpoint axis [95]. ADAM10 plays a crucial role in PM progression, particularly by enhancing tumor cell migration and tumor progression [66]. It is overexpressed in both human and mouse PM, with consistent results observed *in vitro* in AB12 (mouse mesothelioma cell line), PM27 (mice primary mesothelioma cells obtained from ascites), and H28 Mesothelioma cell lines (human sarcomatoid mesothelioma cells), as well as *in vivo* in an intrapleural mouse model that recapitulates key features of human PM. Functional analyses revealed that ADAM10 inhibition via shRNA, or the pharmacological inhibitor GI254023X, affects cell migration, demonstrating that ADAM10 significantly promotes mesothelioma [66]. Importantly, *in vivo* downregulation of ADAM10 resulted in reduced tumor growth, demonstrating its involvement in disease progression. Mechanistically, ADAM10 exerts its pro-migratory effects through its sheddase activity on N-cadherin, releasing a soluble N-terminal fragment (NTF) that stimulates cell migration, likely via the activation of the fibroblast growth factor receptor (FGFR) [66]. This hypothesis was supported by experiments using a specific FGFR inhibitor, which confirmed the role of FGFR signaling in ADAM10-mediated migration. These findings identify the ADAM10/soluble N-cadherin/FGFR axis as a novel pathway contributing to PM invasiveness and highlight ADAM10 as a promising therapeutic target [66]. For this reason, we aimed to develop an inhibitor capable of specifically targeting ADAM10 in PM cells as a strategy to reduce tumor progression and limit its aggressiveness.

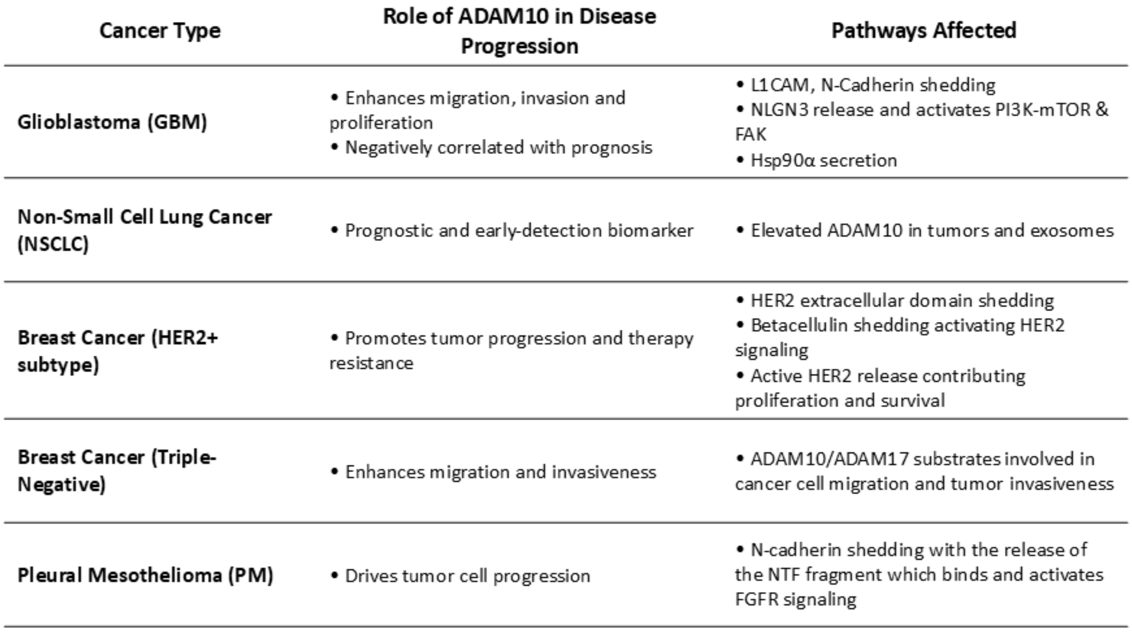

Cancer Type	Role of ADAM10 in Disease Progression	Pathways Affected
Glioblastoma (GBM)	• Enhances migration, invasion and proliferation • Negatively correlated with prognosis	• L1CAM, N-Cadherin shedding • NLGN3 release and activates PI3K-mTOR & FAK • Hsp90α secretion
Non-Small Cell Lung Cancer (NSCLC)	• Prognostic and early-detection biomarker	• Elevated ADAM10 in tumors and exosomes
Breast Cancer (HER2+ subtype)	• Promotes tumor progression and therapy resistance	• HER2 extracellular domain shedding • Betacellulin shedding activating HER2 signaling • Active HER2 release contributing proliferation and survival
Breast Cancer (Triple-Negative)	• Enhances migration and invasiveness	• ADAM10/ADAM17 substrates involved in cancer cell migration and tumor invasiveness
Pleural Mesothelioma (PM)	• Drives tumor cell progression	• N-cadherin shedding with the release of the NTF fragment which binds and activates FGFR signaling

Table 1) Summary of ADAM10 functions in cancer and pathways affected [66,69,87-95].

1.2.5 ADAM10 inhibitors: therapeutic perspectives

Among the natural compounds, rapamycin, a macrocyclic antibiotic produced by bacterium *Streptomyces hygroscopicus,* decreases ADAM10 expression through the mTOR pathway, leading to a decreased production of neuroprotective APP cleavage products [82]. Similarly, triptolide, a terpenoid epoxide produced by *Tripterygium wilfordii,* downregulates ADAM10 expression in different cell lines [82,96].

In addition to natural inhibitors, synthetic compounds, particularly those belonging to the hydroxamate-based zinc-chelating inhibitors class, have been developed. These inhibitors function by coordinating with the catalytic zinc ion present in the active site of ADAM10, thereby blocking its proteolytic activity [69]. One of the most widely used synthetic compounds is the GI254023X (GlaxoSmihKline). GI254023X has demonstrated potent activity in cancers such as glioblastoma and breast cancer. However, due to its lack of selectivity, it exhibited hepatotoxicity, causing the failure in preclinical development [69,94].

Other ADAM10 inhibitory compounds have been developed such as INCB3629 and INCB7839 (Incyte Corporation) which are non-selective ADAM10 inhibitors. INCB7839 is in clinical trial in combination with Rituximab (monoclonal antibody targeting CD20) for the treatment of Diffuse Large B Cell Non/Hodgkin Lymphoma or in association with trastuzumab against breast cancer. This compound reduces the Natural Killer G2D/L (NKG2D/L) shedding mediated by ADAM10 on Hodgkin Lymphoma [97].

Peptide-based inhibitors have been developed only for two members of ADAMs family: ADAM8 and ADAM17 but not for ADAM10 [98]. For ADAM17, inhibitors such as ragespin-1 with an IC_{50} of 92nM were identified using combinatorial peptide libraries and further optimization of the sequences. All of them have, however, shown a limited selectivity, since they also inhibits other MMPs such as MMP-12 due to the highly similarity of their active site [98] [99] .

A particularly promising and unique strategy for ADAM10 inhibition is based on its own prodomain (Tyr21-Thr214), a natural regulatory region of ADAM family members that maintains the enzyme in a latent state. While not all prodomains effectively inhibit their respective enzymes, the ADAM10 Prodomain is a potent and selective inhibitor of ADAM10 activity [73]. Moss *et al* [73] have successfully expressed, in *E. coli,* the mouse ADAM10 prodomain, which share 92% of identity with the prodomain of human ADAM10 and characterized its inhibitory function. It inhibits both murine and human ADAM10 with an inhibition constant (Ki) of 48±36nM for human ADAM10. Moreover, it is very selective for ADAM10 since it doesn’t show significant inhibitory activity for other ADAM family members. Thus, it is the first selective human ADAM10 inhibitor reported so far. Interestingly, a mutant form of the ADAM10 prodomain (C173S) displays a Ki of 36 ± 9nM. The retention of high-affinity inhibition despite mutation of the conserved cysteine suggests that the inhibitory mechanism may differ from the classic cysteine-switch mechanism observed in other metalloproteinases such as MMP-1 [100] and 2 [101], in which the prodomain Cys173 coordinates the catalytic zinc ion maintaining the enzyme in the inactive state [73] .

Taken together, these findings highlight both the therapeutic potential and the challenges in developing potent, selective, and clinically safe ADAM10 inhibitors. Further research is needed to potentially exploit prodomain-based approaches for targeted cancer therapy or to develop a new peptide inhibiting ADAM10 using the phage display technique.

1.3 Phage display: a system for binders' discovery

One of the methodology we used to find an ADAM10 inhibitor is phage display, which is a high-throughput method used to identify binding peptides or antibody fragments specific to a target antigen [102]. In phage display, bacteriophages are engineered to present peptides or proteins on their surface while carrying the corresponding coding DNA inside of the viral particle. This physical linkage between phenotype (displayed molecule) and genotype (the coding sequence) enables efficient selection, amplification, and identification of high-affinity binders from libraries that can reach sizes of 10^9-10^{11} variants [103]. While phage display is the most used system, several other types of display exist.

1.3.1 Overview of surface display technologies

Beyond phage display, other techniques to select binders have been developed: eukaryotic virus display, bacterial display, yeast display, mammalian cell display, ribosome display and mRNA display [Figure 11].

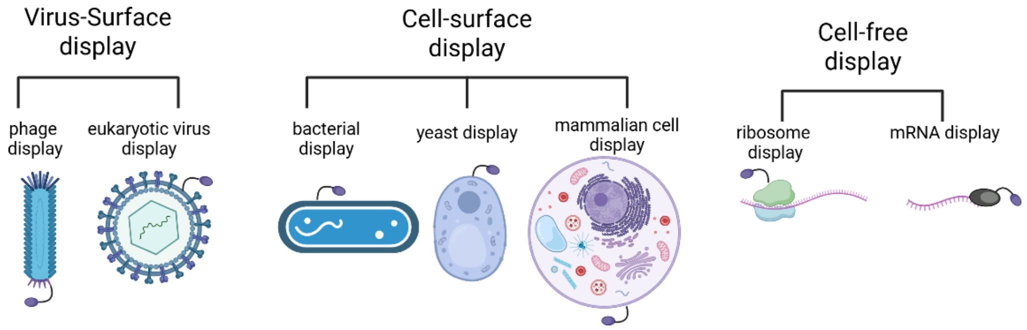

Figure 11) Overview of display techniques, categorized into virus-surface, cell-surface, and cell-free systems. Each method, ranging from phage and eukaryotic virus display to bacterial, yeast, mammalian cell display, and ribosome/mRNA-based cell-free display, illustrates distinct platforms for exposing proteins or peptides. This image was created with BioRender.

Eukaryotic virus can infect a wide range of hosts, including protists, fungi, plants and animals. Three major virus families have been adapted for the display technology:

Adenoviridae, Retroviridae and *Baculoviridae*. For instance Adenovirus have been successfully used to display influenza A antigens and ovalbumin [104].

Bacterial cell surface display allows the presentation of heterologous proteins on the Gram-positive and Gram-Negative cells' surface. Peptides or proteins are typically fused to an anchoring motif by C-terminal or N-terminal fusion. The most widespread bacteria used for bacterial display is *E. coli* due to high grow rate and several mutants available [105]. However, the display of proteins could increase the membrane fragility, for this reason it is possible to use Gram positive bacteria such as *Staphylococcus* and *Bacillus genera*. Applications include the display of proteins and peptides libraries [106,107]. Despite its versatility, bacteria display has several drawbacks such as low display efficiency and inability to express eukaryotic proteins with post-translational modifications [108].

In yeast display, involving typically *Saccharomyces cerevisiae,* proteins are displayed on the cell wall, through the fusion of the protein of interest to cell surface glycoproteins. Yeast display is more suitable than bacteria for proteins that require post-translational processing for efficient activity and folding [108]. However, yeast-specific glycosylation pattern differs from the human one, which may impact the function and structure of engineered proteins. This system has been used to successfully display various molecules including enzymes, cytokines, scFv and Fab [108].

Mammalian cell display was initially developed to allow the isolation of high affinity antibodies in human embryonic kidney 293T cells [109]. The advantages are due to the correct folding of human proteins and correct post translational modifications [108]. This display system is ideal for producing fully human therapeutic proteins. However, limitations include reduced library sizes, lower transformation efficiency and complexity in library screening [108].

More interest is growing for *in vitro* display technologies, due to the lack of transformation steps, which allow the creation and screening of very large libraries up to $10^{12\text{-}14}$ unique variants [110]. These libraries have been used for the selection of high-affinity target-binding molecules as such as peptides and proteins [103].

In ribosome displays, the selection is based on the ternary complex composed by the *in vitro* translation of proteins, and their attachment to the ribosome and to the mRNA. This complex stabilization is obtained by modulating the magnesium ion concentration and by terminating the protein elongation with chloramphenicol or decreasing the temperature. Ribosomal display is mainly used for building massive libraries containing up to 10^{12} different binders [111], but also for biomarker identification. For instance, Cong *et al* [112] have used ribosome display to successfully isolate scFv antibodies specific to 16 different biomarkers, combining the display with a protein microarray, to screen the ribosome-displayed scFvs directly on an array of antigens.

In mRNA display, covalent complexes between a polypeptide and its coding mRNA can be obtained using puromycin, a peptidyl acceptor antibiotic at their 3' end. In this method, during the *in vitro* translation, the ribosomes stall at the junction between the mRNA and engineered DNA linker, allowing the puromycin entrance and amide bond formation. This technique can be used to encode peptides synthesized with unnatural amino acid allowing the synthesis of non-biological polymers [108,113].

Our study has been focused on the use of phage display technology which is described below.

1.3.2 The M13 bacteriophage structure

Various bacteriophage systems, including T4, lambda, and M13 have been used to display proteins or peptides. Among them, the M13 bacteriophage has emerged as the most widely used platform, thanks to extensive knowledge of it accumulated over years [114]. M13 belongs to a group of filamentous phages known as Ff phages [115], which specifically infects *E. coli* strains that express the F pilus. The G3P protein on the phage coat recognizes and binds to the F pilus, initiating internalization into the bacteria. The M13 phage is a non-lytic, single stranded DNA+ phage. Its DNA encodes for eleven different proteins. Six of them are involved in the replication and the phage assembly, while the last five are structural coat proteins. The phage is approximately 900 nm long and it has a diameter of 6.5 nm [116]. Its filamentous structure is primarily composed of around 2700 copies of the major coat protein G8P, which coat and protect the viral genome. The other four coating proteins (G3P, G6P, G7P, and G9P) are present in approximately five copies [114]. Among them G7P and G9P are required for the initiation and maintenance of phage assembly in the host bacterium [103]. The G3P protein plays a crucial role for the phage infection since it mediates the initial interaction with the F pilus allowing phage internalization [Figure 12].

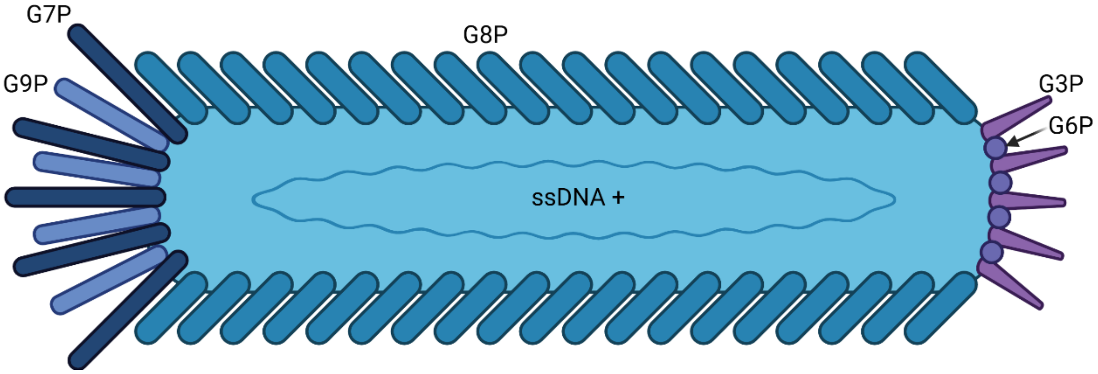

Figure 12) Schematic representation of a filamentous bacteriophage, highlighting its structural components including surface proteins G7P, G9P, G8P, G3P, and G6P, and the internal single-stranded DNA (ssDNA+). This image was created with BioRender.

1.3.3 Infection mechanism of M13 Phage

Phage infection is the process by which the phage enters into *E. coli* cells to replicate. It begins with the phage infection which is mediated by the interaction of G3P with the F pilus on the surface of *E. coli* F+ cells [117] [Figure 13]. Specifically, G3P binds to the N1 and N2 domains of the F pilus, which then enables interactions with TolA, a co-receptor of the bacterium surface. Together with TolQ and TolR, TolA facilitates coat protein depolymerization and the ssDNA translocation into the host cytoplasm [118].

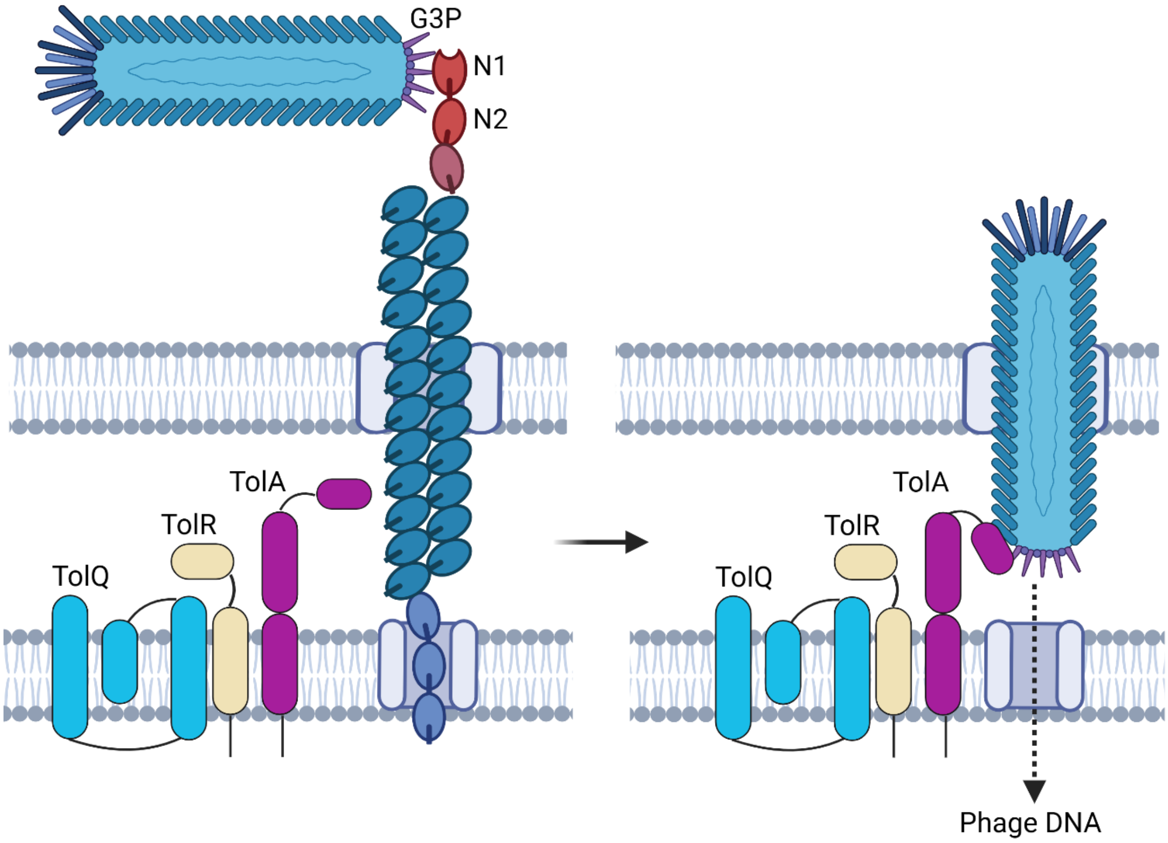

Figure 13) Schematic representation of M13 phage infection. The G3P protein of M13 initiates the binding to the F pilus via N1 and N2 domain. Pilus retraction enable the interaction with TolA. TolQ and TolR components enables the depolymerization and DNA translocation in the cytoplasm. This image was created with BioRender.

Once internalized, the ssDNA serves as a template for the synthesis of the complementary strand DNA (-) of M13 phages forming a dsDNA named replicative form (RF), using the host's replication machinery. Replication starts when G2P nicks the + strand of the RF and covalently binds its 5' end. Host DNA polymerase then elongates the strands using the – strand as template [114]. When the cycle is completed, G2P cleaves the + strand and the replication process is repeated in a rolling circle manner. During the early stage of infection, the newly synthesized ssDNA is converted into RF, to massively replicate the virus genome [Figure 14].

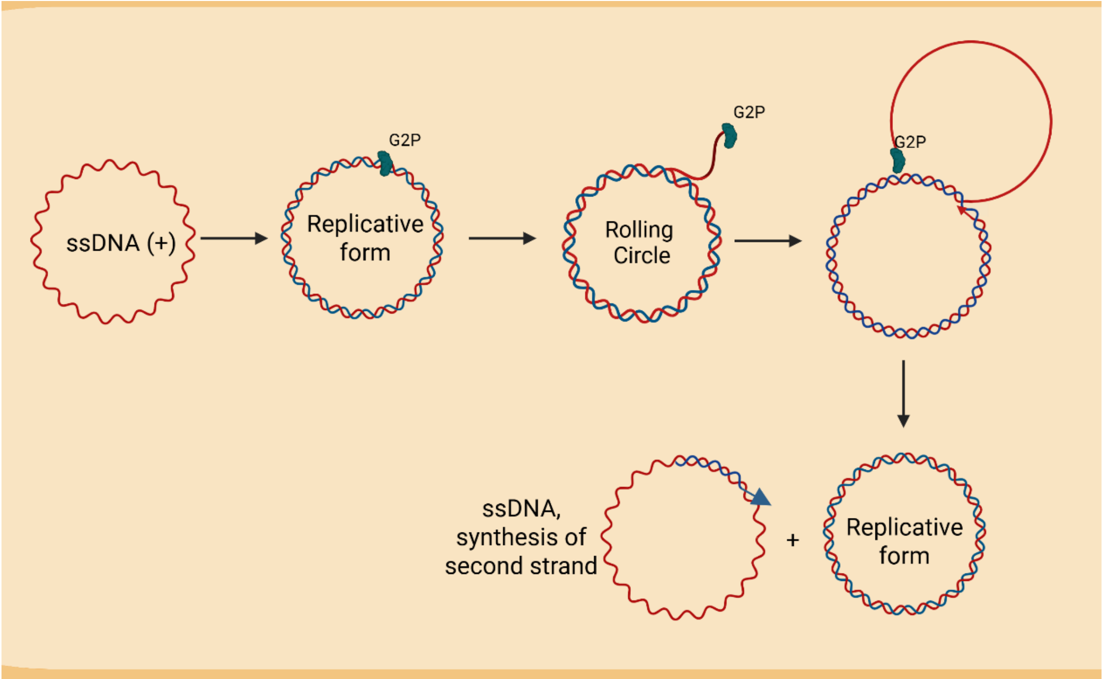

Figure 14) Rolling circle replication of M13 phage. After its entry into the host cell, the single-stranded DNA (+) of M13 is converted into a double-stranded replicative form (RF) using the host machinery. Replication initiates when the viral protein G2P introduces a site-specific nick in the (+) strand of the RF and covalently binds the 5' end. Host DNA polymerase elongates the strand using the (-) strand as template, displacing the original (+) strand in a rolling circle manner. Once a full synthesis is completed, G2P cleaves the newly synthesized strand, generating single-stranded DNA for packing and maintaining the RF for further replication cycles. This image was created with BioRender.

In the late stage of infection, when the G5P is sufficient for fast sequestering the ssDNA, the RFs formation is suppressed. The G5P dimerizes and binds the phage DNA, converting the circular ssDNA into a rod-shaped appearance except for a hairpin loop. This shape is ideal for packing.

The phage assembly occurs in five steps: pre-initiation, initiation, elongation, pre-termination and termination. During the pre-initiation step, 12-14 G4P proteins with G1P and G10P, compose a cylindrical structure between the cytoplasmic membrane and the outer membrane. During the initiation step, the G5P coated phage chromosome associates with G7P and G9P interacts with G1P. In the elongation phase, the G5P is replaced by the G8P forming the filamentous body. In the pre-termination step, the membrane-embedded G3P complexed with G6P are incorporated at the terminal end of the phage particle and the phage is released due to a conformational change in the G3P and G6P complex [114] [Figure 15].

This well-characterized architecture and infection mechanism make M13 an ideal platform for phage display, enabling the presentation of peptides or proteins on its surface for applications in drug discovery, diagnostics and therapeutics.

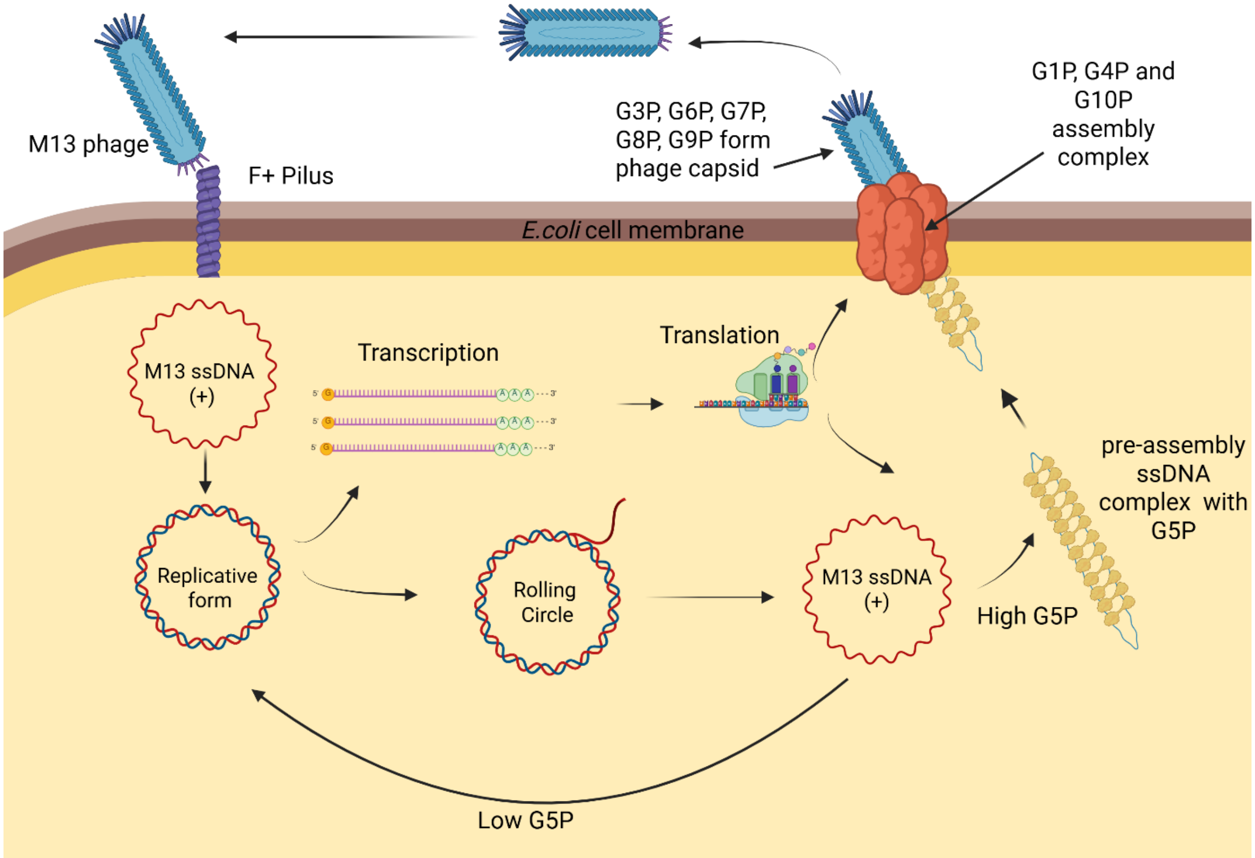

Figure 15) Life cycle of the M13 bacteriophage in E. coli, illustrating attachment to the F+ pilus, entry of single-stranded DNA (ssDNA), formation of the replicative form, transcription and translation of viral proteins, rolling circle replication, and assembly and release of new phage particles. This image was created with BioRender.

1.3.4 Phage display for high affinity target discovery

Phage display was first demonstrated in 1985 by Smith, who fused foreign peptide-coding DNA to the gene for the G3P coat protein of the M13 bacteriophage, incorporating it into the phage genome [119], enabling the surface presentation of peptides on phage particles. Five years later, McCafferty *et al* [120] made a landmark advancement by engineering an M13 phage to display a single-chain variable fragment (scFv) antibody fused with the G3P protein. This achievement demonstrated the feasibility of displaying antibody fragments on the phage surface and laid the foundation for phage display technology, enabling the selection of phages with antigen-binding properties.

Since then, a wide variety of antibody-displaying phage libraries have been developed. These include libraries expressing human heavy-chain variable fragments (VH), camelid and shark-derived VHHs, scFvs, bivalent diabodies, and even Fab fragments [114].

Phage display systems generally follow two main formats: polyvalent and monovalent display. In the polyvalent display, all five copies of the G3P protein on each phage particle are fused to the polypeptide. This strategy is typically used for displaying short peptides, as their small size does not interfere with the infective function of G3P and phage adsorption [108]. In contrast, the monovalent display is used for larger proteins that could impair G3P functionality if all copies are fused with the foreign protein. This system involves two components: a phagemid and a helper phage. The phagemid carries the gene coding the fusion between the protein of interest with G3P, an origin of replication (ori) and a gene for bacterial resistance. While the helper phage lacks its own ori to limit replication, but it provides all necessary elements for phage assembly, including native (unfused) G3P. As a result, the phages are produced with a typical ratio of approximately 1:5 fused G3P to native G3P, preserving their infectivity and limit the avidity effects which will lead the selection of low affinity binders [117].

Although G3P is the most used coat protein for phage display, alternative coat proteins such as G8P, G6P and G7P have also been explored. G8P, for example, is attractive due to its high copy number on each phage particle. Interestingly, the use of G7P for peptide display has been shown not to impair phage function, potentially eliminating the need for a helper phage [121].

Beyond M13, other phages including lytic phages such as T4, T7, P4, and lambda have been used for display applications, expanding the versatility of the technique. Over the past few decades, phage display has proven to be a powerful tool for isolating and identifying high affinity target polypeptides [114].

Phage display has been used to identify peptides that bind to caspases, or metalloproteases [122,123]. More recently, its applications have expanded through integration with complementary techniques. For instance, combining phage display with real-time PCR (qPCR), allows quantitative monitoring of the amplification of phage population after the phage selection on different cells or tissues without relying in slower method such as phage titration [124]. Furthermore, fluorescently labeled phage particles have been used to assess binding specificity and can be employed for cell sorting via FACS or for fluorescence microscopy imaging [108,114]. Additionally, combining phage display with enzymatic assays has enabled the identification of peptides that function as enzyme substrates or mediate microbial adhesion [125].

1.3.5 Commercial phage display libraries

Among commercially available phage libraries, one of the most used is the Ph.D.-12™ Phage Display Peptide Library (New England Laboratory). This system is based on the M13 filamentous phage vector, engineered for pentavalent display of random 12-mer peptides fused to the N-terminal fusion of the G3P coating protein. Although G3P protein is present in only five copies clustered in one end of the M13 virion, this peptide insert does not affect the phage infectivity by binding the F-pilus of the *E. coli* hosting cell, because it is shorter than 50 residues [126]. The reduced valency of G3P libraries, as compared to those based on G8P makes the phage display system more suitable for the discovery of higher affinity binders. The library diversity is approximately in the order of 10^9 independent clones, which represents only a tiny fraction of the $4*10^{15}$ amino acid combinations for a 12-mer library [126]. Unlike phagemid-based display systems, the Ph.D.-12™ Phage Display Peptide Library uses a complete M13 genome, which does not carry a plasmid replicon or antibiotic-resistance cassette. Since the full phage genome encodes all proteins required for virion assembly and infection, no helper phage is needed during the amplification, simplifying the selection workflow [126].

The Ph.D.-12™ Phage Display Peptide Library has been widely applied in different applications including the discovery of antimicrobial and antiviral peptides. For instance, a random 12-mer peptide library was successfully used to identify novel peptide ligands that bind to the envelope glycoprotein gp120 of HIV-1, thereby interfering with its interaction with the CD4 receptor on host cells [127]. Similarly, a study using a disulfide-constrained 7-mer phage display library identified peptides capable of binding the surface of the avian influenza virus subtype H9N2, with one peptide showing significant antiviral activity [128].

Beyond biomedical applications, phage display has also been used in material science, enabling the identification of short peptides that specifically bind semiconductor surfaces [129], and to selectively recognize β-sheet nanofibers, demonstrating the remarkable ability of short peptides to discriminate between different protein structures [123].

1.3.6 Experimental workflow of phage display selection

The selection (biopanning) process includes 6 steps [Figure 16].

I) Binding to the target: The phage library is incubated into a well where the target antigen is immobilized, either by adsorption or via a capture approach (e.g. streptavidin-biotin). During this incubation step, phages displaying peptides with affinity for the antigen bind to the immobilized target.

II) Washing: The non-binding or weakly binding phages are removed by multiple washing steps. Phages displaying the highest affinity peptides remained bound to the antigen.

III) Elution: The bound phages are eluted by an acid or a base.

IV) Amplification: The eluted phages are used to infect *E. coli F+* cells, which produce new phage particles.

V) Phage titer: The eluted and amplified phages are quantified to assess the enrichment of phages displaying binders specific to the target after each round of selection.

VI) DNA sequencing: The DNA from the phages eluted at each round, and constituting sub-libraries, is purified. The gene encoding the pIII (G3P) fusion protein, which carries the antigen-recognition peptide, is then sequenced using Sanger or next-generation sequencing to identify the selected binders.

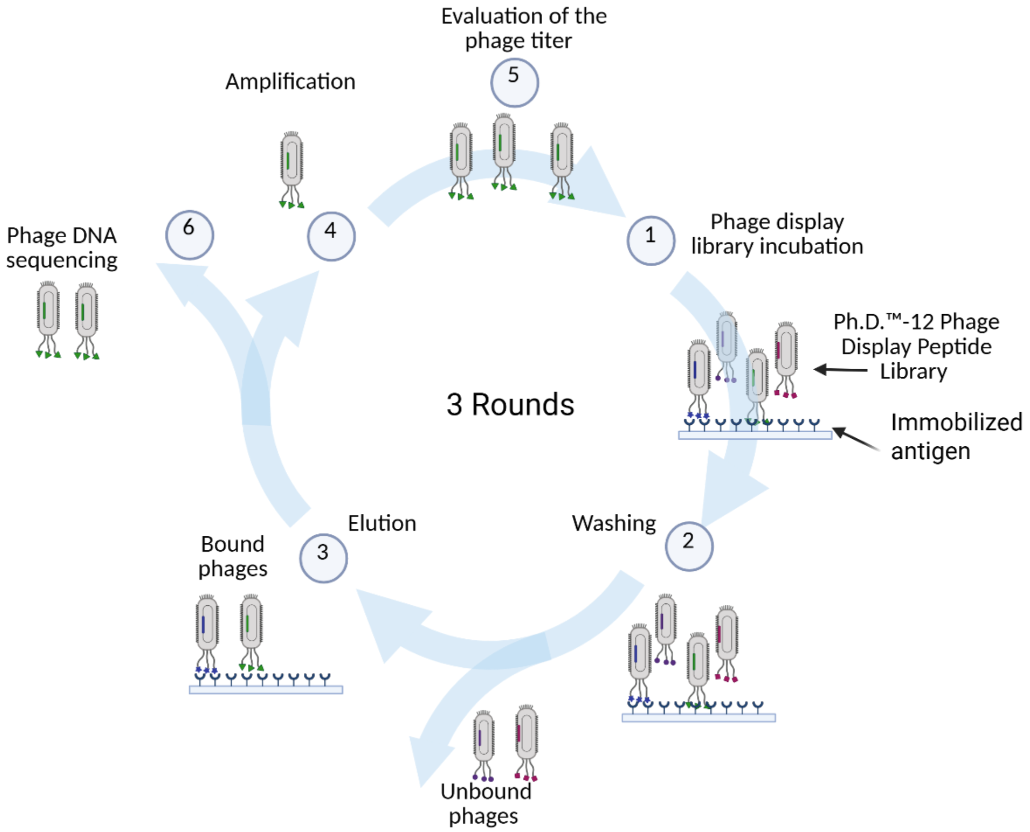

Figure 16) Phage display biopanning cycle, a method used to identify peptides or proteins with high affinity for a target molecule. 1) The phage library is incubated with the immobilized target, and it binds the target. 2) Unbound or weakly bound phages are eliminated by extensive washing steps. 3) Strongly bound phages are eluted from the target by incubation with an acid or a basic solution. 4) Eluted phages are amplified by infecting E. coli cells, allowing the production of new phage particles, and thereby increasing the amount of the selected binder for the next round. 5) At every round, the phage titer is evaluated and 30 individual phage clones DNA for each round are isolated. 6)The G3P gene that carries the peptide of the

phages is sequenced to identify the binders, revealing candidates with the highest affinity. This image was created with Biorender.

Phage display methodology can thus be used to select peptides strongly inhibiting ADAM10 to treat PM. However, due to the role of ADAM10 and its widespread exposition on healthy cells, as discussed above, a specific targeting strategy is essential for new strategies to treat PM.

1.4 Mesothelin: an antigen overexpressed by cancer cells

One promising target to specifically address ADAM10 inhibitor to PM cells is mesothelin (MSLN), which is a cell surface glycoprotein first identified in 1992 by Chang *et al* [131,132]. Its name derives from its predominant expression in mesothelial cells and mesothelial-derived cancer cells, while it is absent in the parenchyma of any other organs. MSLN has been found in the pleura, pericardium and peritoneum, making it a selective marker for certain malignancies [133]. Over the past decades, mesothelin has been extensively documented for its interest as cancer antigen due to its marked overexpression in various malignancies, including PM, epithelial ovarian cancer, pancreatic adenocarcinoma, gastric cancer and triple negative breast cancer (TNBC) [133].

1.4.1 Structural insight into MSLN

The human MSLN gene comprises 17 exons and it is located on chromosome 16p13.3. It encodes an open reading frame of 1,884bp [134]. The open reading frame encodes a 622 amino acid residue (69kDa) precursor protein (pre-pro mesothelin) [135]. During the protein maturation, the N-terminal signal peptide (residues 1-33) is cleaved [Figure 17], and a furin protease cleaves at Arg295 yielding two distinct products: i) a mature 40kDa extracellular membrane glycosylphosphatidylinositol (GPI)-anchored MSLN (mMSLN), which localizes to membrane lipid raft after the addition of the GPI anchor at Ser598, and II) a 31kDa C-terminal region known as Megakaryocytic potentiating factor (MPF) which is secreted and released in the blood stream [135] [Figure 17]. Interestingly, mMSLN could be further cleaved through physiological shedding mediated by members of ADAM family, especially ADAM17 [136]. The fragment released into the blood is known as soluble mesothelin (SMRP). Although this shedding has not been specifically characterized in PM cancer cells, studies in other systems have shown that reducing ADAM17 expression in pancreatic ductal adenocarcinoma KLM1 cell line decreases mMSLN shedding by ~45%, whereas no effect is observed in endocervical adenocarcinoma KB31 cell lines [136]. Similarly, ADAM10 inhibition has been reported to decrease MSLN cleavage in OVCAR8 cell line. However, the extent and effect of MSLN cleavage appear to be cell line and tumor type dependent.

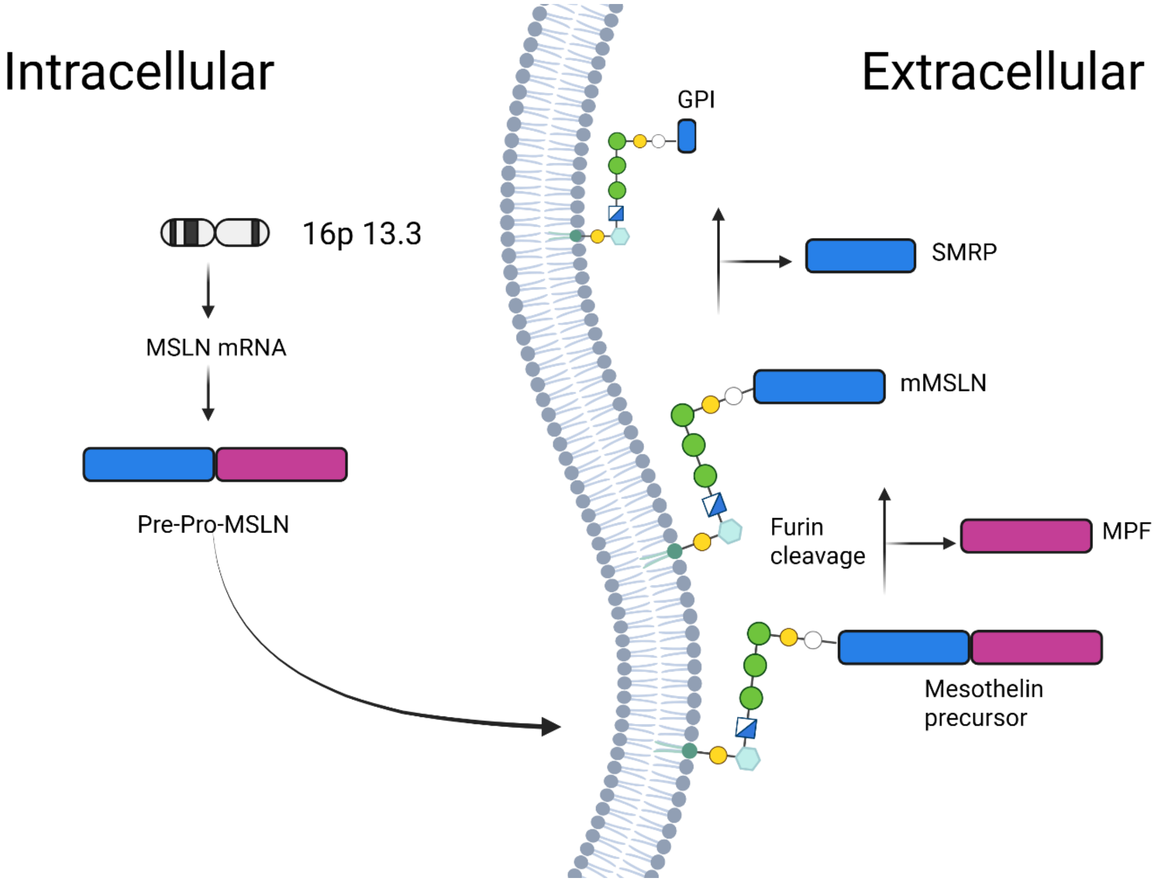

Figure 17) Schematic representation of mesothelin (MSLN) biosynthesis and processing. Intracellularly, MSLN mRNA transcribed from chromosome 16p13.3 encodes Pre-Pro-MSLN. which is translated and translocated to the membrane. A furin cleavage yields mature MSLN (mMSLN), which is anchored to glycosylphosphatidylinositol (GPI) and MPF (Megakaryocyte Potentiating Factor) which is released into the bloodstream. Mature MSLN could undergo a further cleavage by ADAMs family protein, leading to the release of a soluble fragment referred to as SMRP. This image was created with BioRender.

The final GPI-anchored MSLN (mMSLN) contains 303 amino acids, and there are three N-linked glycosylation sites at the following positions: Asn388, Asn488, and Asn515 [137]. The post-translational modifications are not merely structural, since they influence the ligand binding, particularly with MUC16, a mucin implicated in ovarian cancer metastasis [138]. Two disulfide bridges have also been identified between, respectively, Cys302-Cys326 and Cys442-Cys468, contributing to the protein's structural stability.

Recently, partial structure of mMSLN was solved (PDB:8CX3) from residues 295 to 600 with a resolution of 3.61 Å [Figure 18 C] [139]. This structure is coherent with the AlphaFold 3.0 server prediction structure [Figure 18 B-C] and reveals a solenoid structure composed of ARM, Armadillo Repeat Motifs, and HEAT motifs [Figure 19]. ARM typically consist of three α-helixes forming a helical turn [140]. ARM-repeated proteins are characterized by repeated ARMs stacked together with a hydrophobic core, forming an elongated superhelix, while HEAT motifs consisting in two anti-parallel α-helixes. mMSLN has in total 7 repeated units: 5 interspersed ARMs repeats and 2 HEAT motifs units [139].

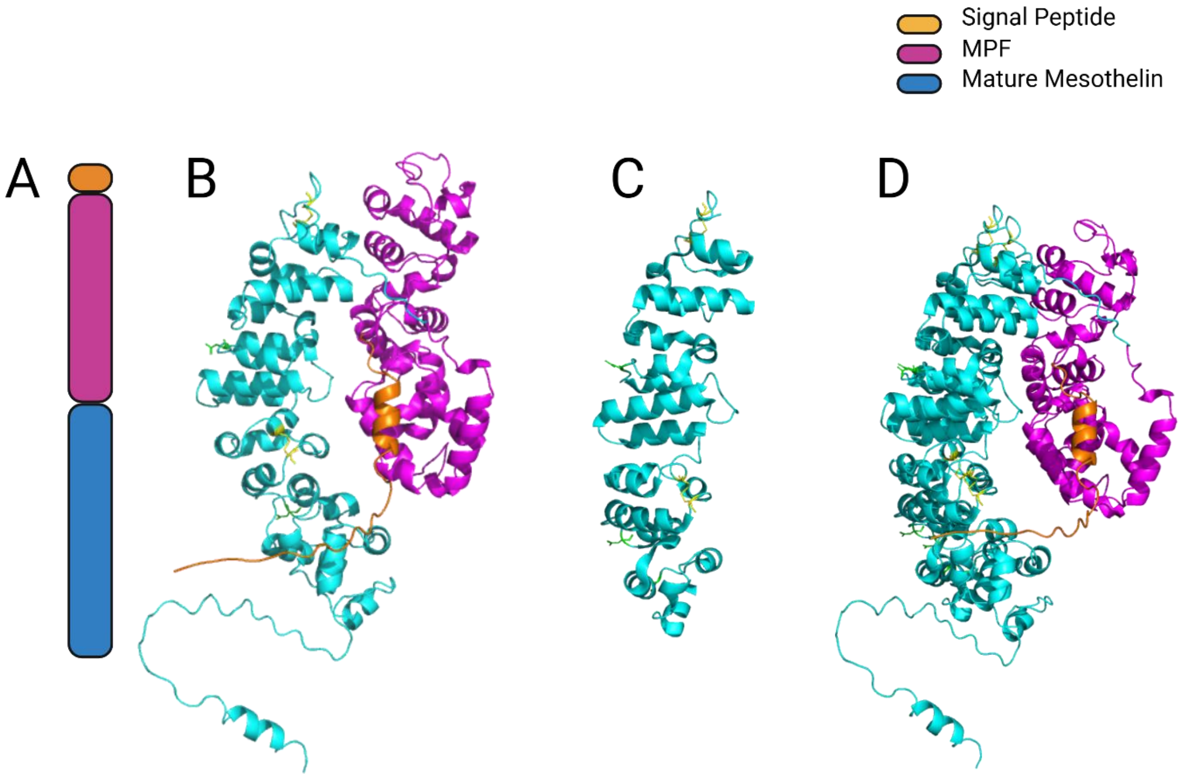

Figure 18) Structural organization of MSLN. A) Schematic representation of MSLN domain organization. The protein consists of an N-terminal signal peptide (orange), the megakaryocyte potentiating factor (MPF magenta), and mMSLN (cyan) B) Predicted three-dimensional structure of full-length pre-proMSLN generated using the AlphaFold3 server. Disulfide bonds are shown in yellow, and the glycosylation sites are in green. C) Experimentally determined X-ray structure of the mature mesothelin domain (PDB ID: 8CX3) from amino acids 295 to 600. D) Superimposition of the X-ray structure (8CX3) with the AlphaFold3 predicted full length pre-proMSLN. The overlay illustrates the correspondence between the experimentally determined mMSLN structure and the in-silico model. This image was created with Pymol and BioRender.

Three mMSLN variants have been identified. The variant 1 is the canonical isoform expressed by both normal and malignant cells. Variant 2 differs from the first one by a 24 amino acid insertion, while the third variant encodes for a mMSLN with an alternative C-terminus with a non-functional GPI-anchor motif. This isoform is unable to bind to the membrane and is restricted to the nuclear fraction. Its importance in tumor biology remains unclear [141].

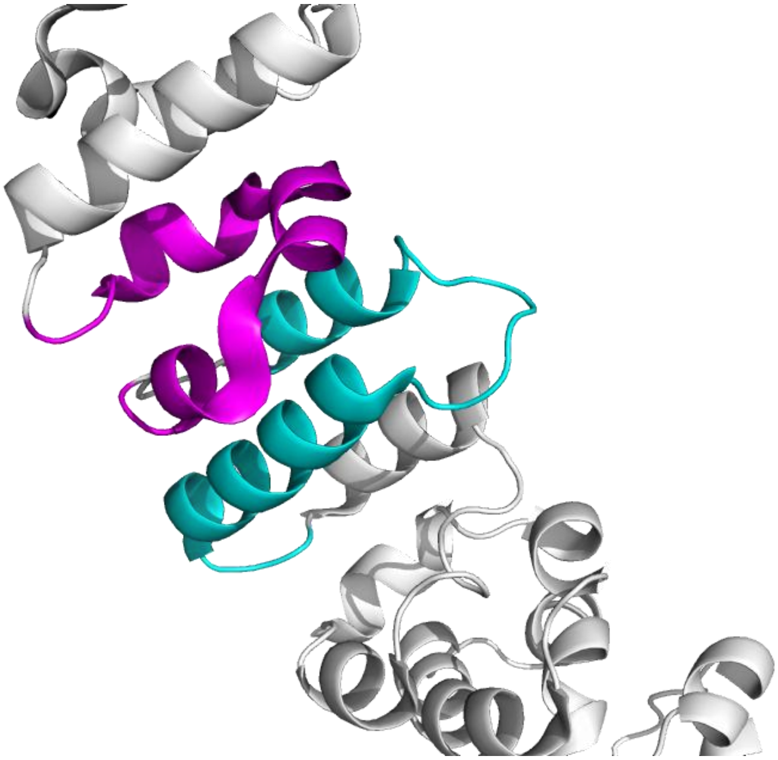

Figure 19) Structure of mMSLN (PDB:8CX3). The figure highlights two characteristic structural motifs within the mature mesothelin: the ARM repeat motif depicted in magenta, and the HEAT repeat motif shown in cyan. This image was created with Pymol.

1.4.2 Functional roles of mMSLN in cancer

Early studies conducted by Bera and Pastan [142] demonstrated that mMSLN knockout mice displayed no evident alteration in development, physiology, or reproduction, suggesting that mMSLN is non-essential under physiological conditions. Over the years, numerous *in vivo* and *in vitro* studies have attempted to elucidate its biological role, and in particular its role in cellular processes and tumorigenesis. mMSLN is mainly expressed in epithelial cells of the pleura, peritoneum and pericardium [143] where mesothelium cells are present. Emerging evidence suggests that mMSLN is involved in immune responses and the regulation of inflammation, possibly through its extracellular mature form [144].

One of the most well-characterized binding partners of mMSLN is MUC16, a glycoprotein highly expressed in ovarian cancer cells and PM [145,146]. The interaction between MUC16 and mMSLN plays a role in peritoneal metastasis of ovarian tumors by promoting cell adhesion and migration [146]. The binding site of mMSLN responsible for this interaction has been mapped to amino acid to Tyr318, Trp321 and Glu324 [146]. This interaction also downregulates Dickkopf-1 (DKK1) via the SGK3/FOXO3 signaling pathway, thereby enhancing cellular migration and promoting ovarian cancer metastasis [147].

Furthermore, mMSLN interaction with MUC16 triggers MMP-7 expression via p38 MAP pathway in pancreatic ductal adenocarcinoma, contributing to the tumor proliferation, differentiation, invasion and migration. Moreover, mMSLN overexpression also enhances resistance to chemotherapeutic agents by promoting epithelial to mesenchymal transition (EMT) [135,148].

In pancreatic cancer, a novel mechanism involving mMSLN overexpression has been identified by the constitutive activation of STAT3 that leads to increased cyclin E expression and the formation of cyclin E /cyclin dependent kinase 2 complex, and acceleration G1-S phase transition [149]. However, the exact way in which mMSLN activates STAT3 remains unclear. Overexpression of mMSLN in pancreatic cancer has also been shown to activate NF-kB, resulting in elevated IL-6 production, enhanced cell proliferation, and improved survival [150].

The mechanism by which mesothelin transduces intracellular signals remains unclear, as the mature membrane-bound form lacks a transmembrane and cytoplasmic domain. Consequently, signal transduction mediated by mesothelin remains largely speculative. Lipid rafts function as dynamic signaling platforms by concentrating receptors and membrane-associated enzymes [151]. Within this context, mMSLN may act as co-receptor, facilitating its interactions with multiple proteins that play role in signal transductions, including receptors adhesion molecules and transmembrane proteases [152]. Similar raft-mediated signaling mechanism have been described for multiple GPI-anchored proteins [153].

In PM, mMSLN expression is associated with increased tumor aggressiveness. Analysis of the mMSLN promoter revealed three CpG methylation sites located 214bp upstream of the transcription start site. This sites are hypomethylated in tumor tissue compared to normal pleura, suggesting that epigenetic deregulation contributes to mMSLN overexpression in PM tumors [154].

1.4.3 Mesothelin as a Biomarker and Target in PM

Mesothelin is under investigation as a tumor biomarker and therapeutic agent in PM due to its high and selective expression in epithelioid and biphasic PM. Indeed, due to the high expression of mMSLN on the tumor surface several therapeutic strategies targeting mesothelin have been developed for PM [155] [Figure 21].

SS1P, a recombinant immunotoxin composed of a high-affinity murine anti mMSLN antibody chemically conjugated to *Pseudomonas* exotoxin A (PEA) has shown promising results. The binding between the anti mMSLN antibody and mMSLN occurs in the N-terminal region of mature mesothelin (amino acid region between 296-390) [Figure 20] and mediates the drug internalization. Once in the cells, the PEA toxin inhibits the elongation factor-2, ceasing the protein synthesis and therefore inducing the cell death [156]. However, the efficacy of SS1P is limited by the development of anti-PEA antibodies in patients after multiple injections. To reduce immunogenicity, researchers developed LMB-100, which incorporates a fully humanized Fab fragment derived from the murine anti mMSLN antibody, along with deletion and point mutations in PEA [157]. In a Phase I clinical trial (NCT01445392), treatment of PM patients with SS1P in combination with chemotherapy, showed significant antitumoral activity, although its safety remains to be demonstrated.

Another therapeutic strategy involved the development of MORAb-009 (amatuximab), a high affinity monoclonal antibody specific for mMSLN. It recognizes the N-terminal domain of mMSLN (296-390) [Figure 20], preventing the interaction between mMSLN and MUC16, and thereby reducing the tumor metastatic and invasiveness potential [158].

Some PM patients have also been involved in a clinical trial with CRS-207, a cancer vaccine based on a 1,000 fold attenuated strain of *Listeria monocytogenes*. This strain is engineered through deletion of two virulence genes *actA* and *internalin B,* and modified to secrete human mMSLN, thereby stimulating an anti mMSLN immune response. After internalization in macrophages, CRS-207 secretes mMSLN, which is processed and presented on MHC class I complexes, ultimately triggering a cell-mediated immune response [159]. In a phase I clinical trial (NCT00585845) involving 17 patients (including 5 with PM), CRS-207 demonstrated safety and good tolerability in the bloodstream. In a subsequent phase Ib study (NCT01675765), patients with an unresectable PM, CRS-207 combined to chemotherapy showed anti-tumoral effect for 63% of patients [158,160].

Another explored strategy is the Anetumab ravtansine, an antibody-drug conjugate composed by a fully humanized anti mMSLN antibody conjugated with DM4, a maytansinoid tubulin inhibitor. This drug binds cancerous cells expressing mesothelin and following its internalization, it disrupts microtubules and induces cell apoptosis [161]. Preclinical studies showed an improved anti-tumor effect when used in combination with standard chemotherapy.

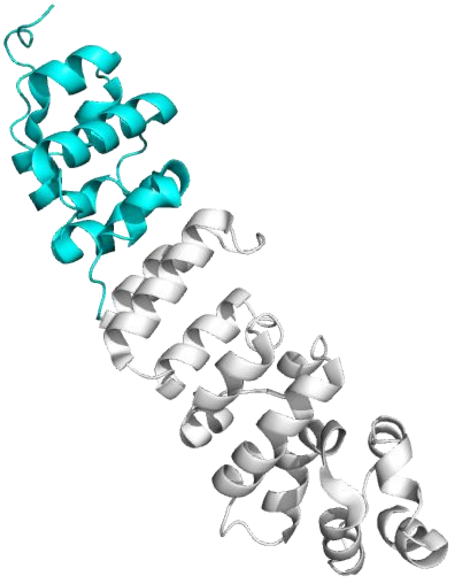

Figure 20) Three-dimensional representation of mMSLN (PDB:8CX3) highlighting the N-terminal region (residues 269-390 in cyan), that constitutes the principal epitope targeted by therapeutic antibodies SS1P, MORAb-009 and anetumab ravtansine. This image was created with Pymol.

As already mentioned, a major challenge in mesothelin-targeted therapies arises from the extracellular shedding of the GPI-anchored mMSLN. This shedding reduces therapeutic efficacy by enabling MSLN to act as a decoy, binding therapeutic antibodies and preventing them from reaching the membrane bound MSLN at the tumor site. To overcome this, a combination of strategies is explored. Paclitaxel (chemotherapeutic agent), when co-administrated with SS1P reduces mMSLN shedding, thereby improving the efficacy by increasing the amount of drug available to bind tumor associated mMSLN [158]. The exact mechanism underlying this effect, however, has not yet been elucidated [162].

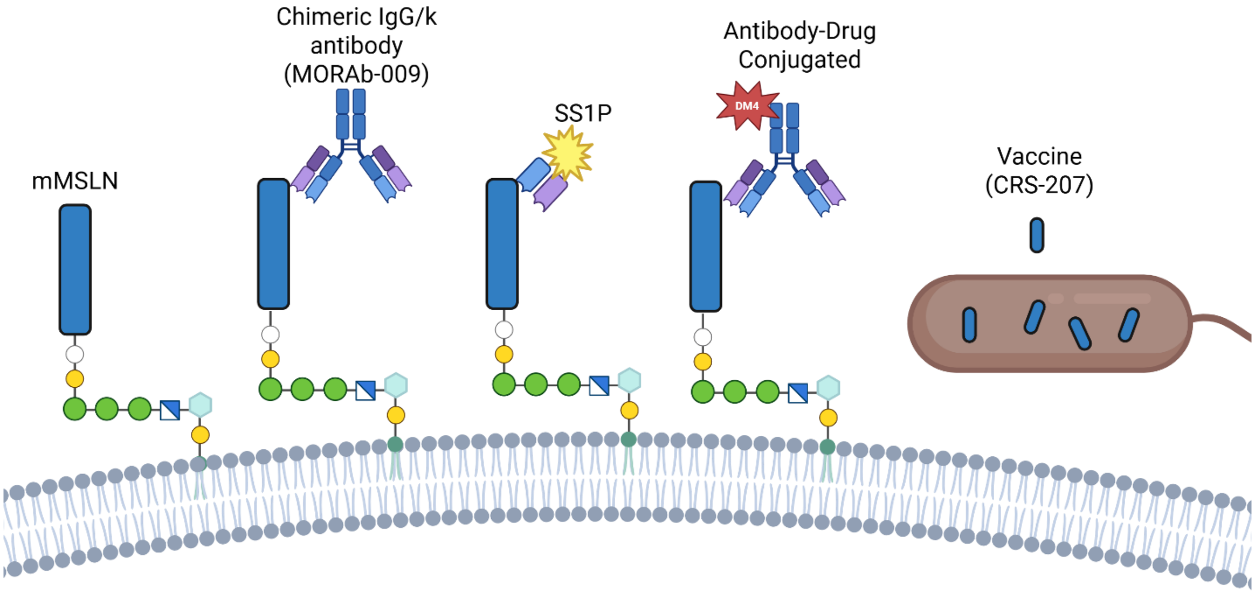

Figure 21) Therapeutic strategies targeting mesothelin (MSLN) on the cell surface, including chimeric IgG/k antibody (MORAb-009), immunotoxin (SS1P), antibody-drug conjugate with DM4, and the CRS-207 vaccine. This image was created with BioRender.

Robinson *et al* first reported SMRP of 2003 using an ELISA based on the SM-165 antibody [163]. This assay was later commercialized as MESOMARK (Fujirebio Diagnostics, Malvern, PA) and was approved by the FDA in 2007. However, SMRP cannot be used universally as a diagnostic marker since MSLN is negative in sarcomatoid histological sub-types [164]. Furthermore, its effectiveness may be compromised in patients receiving mesothelin-targeted antibody-based therapies due to interference with circulating mesothelin. Indeed, several mesothelin targeting antibodies recognize a specific conformational epitope within the N-terminal region of the mature mesothelin (approximately residues 296-359), similar to other therapeutic antibodies directed against this domain [Figure 20]. For this reason, MPF has also been proposed as a biomarker since it does not interfere with any anti mesothelin treatment, and elevated MPF levels have been associated with a poor prognosis in PM patients [155].

To effectively target MSLN, a specific drug is needed. To develop such a tool, the use of the variable domains of heavy chain-only antibodies was investigated.

1.5 Variable domains of Heavy-Chain-only Antibodies (VHHs)

In 1989, Professor Raymond Hamers-Casterman from the Vrije Universiteit Brussel (VUB) discovered a unique class of antibodies lacking the light chain, known as heavy-chain-only antibodies (HCAbs) while studying a *Trypanosoma evansi* infected dromedary camels [165]. The Variable domain of HCAbs, also referred to as VHH, are fully capable of recognizing antigens. Due to favorable properties, described in the following sections VHHs, constitute highly versatile molecules for both therapeutic and diagnostic applications [165–167].

1.5.1 A small and stable antibody fragment known as variable domain of heavy-chain-only antibodies

HCAbs are naturally found in members of the *Camelidae* family in addition to conventional IgGs. They are characterized by the absence of both the first constant domain of the heavy chain (CH1), which is required for the light chain pairing [166], and light chain polypeptide. Thus, the molecular mass of HCAbs is of approximately 90kDa compared to 150 kDa for conventional IgGs [166,167]. The antigen binding domain of HCAbs is therefore reduced to a single domain, referred to as variable domain of the heavy-chain-only antibody (VHH). VHHs are structurally and functionally equivalent to Fvs fragments in conventional IgGs.

The proportion of HCAbs in Camelidae varies between species; they represent about 50-80% of all IgGs in camels, but only 10-25% in South American camelids species [168]. Camelids are the only family within Artiodactyla order, (which includes Ruminantia and Suiformes) to produce functional HCAbs, although non-functional heavy-chain-only antibodies have been described in humans with a pathological disorder or in mouse hybridoma due to genetic deletions of part of VH and CH1 regions [169,170]. A similar distinct class of antibodies, known as immunoglobulin new antigen receptors (IgNARs), has been identified in cartilaginous fish such as nurse sharks and wobbegong. IgNARs also lack light chains and possess a variable domain (VNAR) responsible for antigen recognition. Despite their sequence divergence, HCAbs and IgNARs are products of convergent evolution, sharing structural and functional similarities [171] [Figure 22].

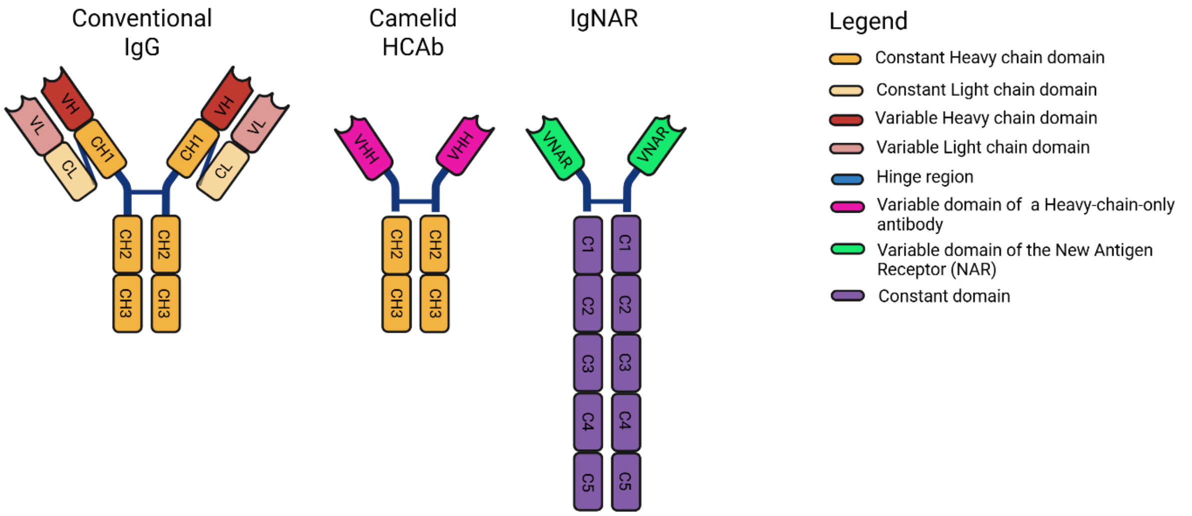

Figure 22) *Comparative structural overview of antibody formats including IgG, Camelid heavy-chain-only antibody (HCAb) and shark IgNAR. Each structure highlights the presence or the absence of light chains, hinge regions, and constant/variable domains. Human IgG consists of two heavy and two light chains forming a Y-shaped molecule. Camelid HCabs and shark IgNARs lack light chains. VHH represents the minimal antigen-binding domain derived from camelid HCAbs. This image was created with BioRender.*

1.5.2 Structure of VHHs

A VHH comprises three complementarity-determining regions (CDRs), and a conserved framework (FR) itself divided into four sections (FR1, FR2, FR3 and FR4) [Figure 23]. The CDRs are responsible for antigen recognition, while the framework provides structural stability. Structurally, a VHH is composed by nine β-strands (A-B-C-C'-C''-D-E-F-G) forming two β-sheets, one with four strands and another with five strands connected by loops and stabilized by a disulfide bond [172]. The hypervariable regions are loops connecting B-C, C'-C'' and F-G strands. VHHs share a high sequence identity (83-91%) with the consensus sequence of human VH domains [173]. In VHs, FR2 contains four conserved hydrophobic residues, which interact with the light chain, while in VHHs, these residues are replaced by smaller or hydrophilic amino acid [174], which is associated with the high solubility of VHHs. Interestingly reverting these amino acids in a VHH to mimic human VH can induce the dimerization of the humanized VHH [175]. Another difference between VHs and VHHs is observed in hypervariable region loops. To provide a large interacting surface of 600-800 $Å^2$, comparable of the 600-900 $Å^2$ of conventional IgGs, VHHs feature a longer CDR1 and CDR3 [176,177]. The elongated finger-tip CDR3 of VHHs, enables to access cryptic epitopes, that are generally inaccessible to conventional antibodies such as enzyme active sites. However, increased loop length also introduces conformational flexibility, which can be entropically unfavorable for binding. To counteract this, many VHHs with long CDR3, which averages ~16 amino acids compared with the ~14 amino acids in the human VH domain, contain an additional disulfide bond. Interestingly, this disulfide bond occurs less frequently in llama VHHs due to the generally shorter CDR3's length compared to the one in dromedary VHHs [174].

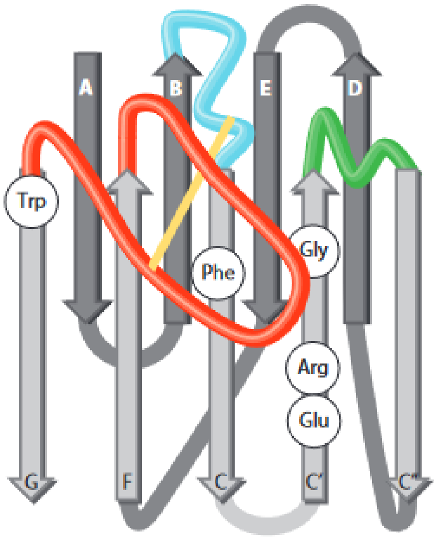

Figure 23) Structural diagram of a VHH domain highlighting its β-sheet architecture. The nine β-strands (A–G) are depicted as arrows forming the core framework, interconnected by loop regions (grey, red, blue, and green). The complementarity-determining regions (CDRs) are shown in blue, red, and green, while the remaining loops correspond to framework regions contributing to antigen binding and structural stability. The additional disulfide bond between CDR1 and CDR3 is highlighted in yellow. The canonical intradomain disulfide bond (between framework regions) is not shown in this representation. This figure was originally published by Muyldermans et al.[167].

The shelf life of VHHs is several months at 4°C and even longer at -20°C. Furthermore, they shows an high thermal tolerance with a stability at 37°C of several weeks [178]. However, due to their small size of around 15kDa, VHHs exhibit a very short circulatory half-life, typically in the average of 30 min, with some VHHs being completely cleared from bloodstream within the first 1h post injection [179]. To extend the blood half-life, several strategies have been developed, such as PEGylation [180] or fusing a therapeutic VHH to an anti-serum albumin VHH. Serum albumin itself has a long circulatory half-life of ~19 days, which allows the VHH to avoid rapid renal clearance and remain in the bloodstream significantly longer, typically around 30-50 h [181].

1.5.3 VHHs generation and selection

VHHs can be selected starting from three different sources: immune, naïve or synthetic libraries, each offering distinct advantages depending on the application. Immune libraries are generated by immunizing a Camelidae species (e.g., an alpaca or a dromedary) with the target antigen, typically over the course of two months with at least four injections [182]. Alternatively, transgenic mice engineered to produce heavy-chain only antibodies (HCAbs) can be used as source [183].

Naïve libraries are constructed from non-immunized camelids and represent a flexible, rapid alternative for generating large panels of antibody fragments. Once established, a naïve library can be screened repeatedly against different antigens, making it a versatile resource for the isolation of diverse VHH binders [184]. These libraries have a good diversity of around 10^9 distinct VHHs, enabling the selection of high affinity binders. For instance using this methodology an anti-polyadenylate-binding protein-1 (PABPN1) VHH has been identified with an affinity of 10.1 nM [185].

Synthetic libraries represent an emerging alternative to animal immunization for selecting high-affinity VHH binders. These libraries have a diversity of around 10^{10} and offer high modularity and are characterized by two key design parameters: framework selection and CDR engineering [186]. Strategic modification of CDR length can alter the structural flexibility of the binding region, thereby enhancing the ability to target cryptic epitopes that are sterically inaccessible to conventional antibodies (~150kDa [187]), but reachable by the much smaller VHHs (~12-15kDa [166,188]) .

For immune and naïve libraries, the process begins with collection of blood samples, followed by isolation of peripheral blood mononuclear cells (PBMCs) for total RNA extraction and subsequent cDNA synthesis. PCR amplification is then performed to selectively target sequences spanning the VHH coding region and the conserved CH2 domain. Agarose gel electrophoresis is then used to select sequences derived from HCAbs which are smaller than conventional antibody sequences. A second PCR amplified the VHH region using primers that introduce restriction enzyme sites for cloning [166,172].

The amplified VHH genes are ligated into suitable vectors, such as phagemids, and the resulting constructs are used to transform *E. coli* TG1 cells to generate an immune or naïve library. Ideally, these libraries should contain at least 10^7 unique clones [166,172]. Among the various display technologies, phage display remains the most widely used method for presenting VHHs, and the same procedure is applied to synthetic libraries. After selection by phage display, ELISA assays are used to validate the binders before sequencing to identify the best candidates [166,167,172]. VHHs identified in this way are typically expressed in *E. coli* [166].

1.5.4 VHHs as therapeutic and diagnostic agents

VHHs are used as therapeutic or diagnostic tools. Over the past few decades, they have been extensively used due to their small size, high stability, easiness to produce and unique binding capabilities that enabled applications across oncology, imaging, biosensing, and immunotherapy, with a VHH-based agent approved by the FDA [189]. Because of their shorter half-life compared to conventional human antibodies, associated with a low radiation exposure and a decreased risk for patient, VHHs have been used in molecular imaging [190]. The fast pharmacokinetics of VHH-based tracers, allows imaging to be performed within a few hours after administration, enabling same-day imaging [191]. In a preclinical study of photodynamic therapy, VHHs were conjugated to a photosensitizer, a light activatable compound that generates cytotoxic reactive oxygen species upon irradiation at specific light wavelengths. By targeting cytotoxicity on tumor, this approach archives localized destruction with minimal injury to surrounding tissues [192]. VHHs have also been used in radioimmunotherapy, where they selectively bind to antigens specifically expressed on malignant cells and deliver radionuclides to the tumor site, thereby minimizing toxicity to healthy tissues [193]. Similarly, VHHs can serve as carriers for conjugated drugs, helping to overcome the toxicity and adverse effects associated with traditional chemotherapeutic agents [194]. An interesting example is the anti-HER2 VHH doxorubicin conjugate which showed synergistic anti-tumor effect in combination with trastuzumab treatment [195].

VHHs have also been conjugated with various functional proteins including toxins (cucurmosin and *Pseudomonas* exotoxins), cytokines (IFN gamma, IL-2 and TNFα) and tumor inhibitory peptides, thereby showing inhibition of tumor growth [196–199].

Furthermore, VHHs have shown promise in cancer vaccination strategies. Woodham *et al.* conjugated an anti-CD11b VHH with an antigen overexpressed in human papillomavirus associated cancers. This drug has induced a strong CD8+ T-cell response against HPV positive tumors [200].

In addition to therapeutic applications, VHHs have been used as biosensors. These devices combine a VHH-based bioreceptor with a semiconductor to detect and quantify a specific antigen. Upon antigen binding, a change in electric potential is generated and amplified into a measurable signal. Compared to ELISA, biosensors offers a faster detection [166] and biosensors based on a VHH have been successfully used for the fibrinogen detection, a cardiovascular disease biomarker or for detecting SARS-Cov-2 [201,202].

1.5.5 Clinical trials involving VHHs and FDA approved drugs

Since the discovery of VHHs, and their growing interest for therapeutic applications, many VHH based drugs have been developed, four of them have been approved for clinical use and several VHHs, are currently undergoing clinicals trials. Among them Carvykti, a bivalent anti-B-cell maturation antigen (BCMA) VHH that functions as an antigen receptor on T cells, has been approved in 2022 for the treatment of advanced multiple myeloma [203]. In 2021, caplacizumab (Ablynx), a bivalent VHH based therapy targeting thrombotic thrombocytopenic purpura (TTP), received FDA approval. This VHH inhibits the interaction between von Willebrand factor multimers and platelets, preventing thrombocytopenia, hemolytic anemia and tissue ischemia [204]. Another approved drug is Ozoralizumab (Nanozora), developed by Taisho Pharmaceutical Co. Ltd, a trivalent VHH construct designed to treat rheumatoid arthritis. It was approved by Japan's Pharmaceuticals and Medical Devices Agency (PMDA) [205]. In all cases, VHH sequences have been humanized.

1.5.6 An anti mMSLN VHH

In 2015, Prantner *et al* [206] have described an anti mMSLN VHH (A1 VHH) generated via subcutaneous llama immunization with soluble human mature mesothelin protein. This A1 VHH is composed of 131 amino acids, with a molecular weight of ~14kDa, and a theoretical isoelectric point (pI) of 7.2. The A1 VHH specificity was demonstrated by flow cytometry: it binds to multiple cell lines expressing mMSLN including ovarian cancer cells (OVCAR-3 and SK-OV-3), cervix adenocarcinoma cells (HeLa) and prostate carcinoma cells (22Rv1), but it does not bind to mMSLN-negative cells. A competitive mMSLN binding assay was also performed between A1 VHH and the well-characterized monoclonal antibody K1, the first known antibody targeting mMSLN [206]. Both antibodies recognize the same epitope [206]. Using flow cytometry, the A1 VHH displayed an apparent K_D of ~15nM, indicating high affinity [206]. Furthermore, the A1 VHH was conjugated with quantum dots, semiconductor nanoparticles which absorb and emit light at tunable wavelength, demonstrating its potential for cancer diagnosis. The small size and high specificity of this A1 VHH highlight its promise to generate next generation therapeutic molecules [206]. For this reason, we leveraged this A1 VHH to selectively deliver the ADAM10 inhibitor to PM sites.

2 - Thesis objectives

2 - Thesis objectives

This work aims to develop a novel therapeutic strategy to improve the treatment of pleural mesothelioma (PM). We designed a Dual Targeting protein [Figure 24] capable of selectively recognizing PM cells through simultaneous binding to i) mature mesothelin (mMSLN), an overexpressed surface antigen on PM malignant cells and ii) ADAM10, a transmembrane protease involved in tumor progression and migration, both of which are highly expressed in epithelioid and biphasic mesothelioma subtypes. mMSLN is targeted by a VHH enabling site-specific delivery to the tumor microenvironment, while ADAM10 is targeted by an inhibitory protein, both components being fused into a single Dual Targeting protein.

To develop the ADAM10 specific inhibitor, we followed two complementary strategies. First, we used phage display to identify peptide inhibitors against the recombinant extracellular domain ADAM10 and ADAM10-overexpressing cells. Candidate sequences were analyzed *in silico* to select those predicted to bind the active site of ADAM10, and the most promising peptides were validated for their inhibitory activity *in vitro*. Second, we used the ADAM10 Prodomain, a specific inhibitor, which was previously biochemically characterized and shown to inhibit ADAM10 both *in vitro* and in cells. In parallel, the A1 was validated for its binding specificity to mature mesothelin, including on living cells. We then engineered a dual-targeting fusion protein by fusing, via genetic engineering, the ADAM10 prodomain to the A1 VHH. This construct was experimentally confirmed to bind mature mesothelin and to inhibit ADAM10 activity. Its therapeutic potential was evaluated *in vitro* on PM cell lines and *in vivo* in a mouse model. Collectively, our findings provide the first evidence of a Dual Targeting protein that simultaneously engages mature mesothelin and inhibits ADAM10. This strategy could represent a therapeutic approach for PM and could be used in combination with standard chemotherapy or immunotherapy to enhance treatment efficacy and patient survival.

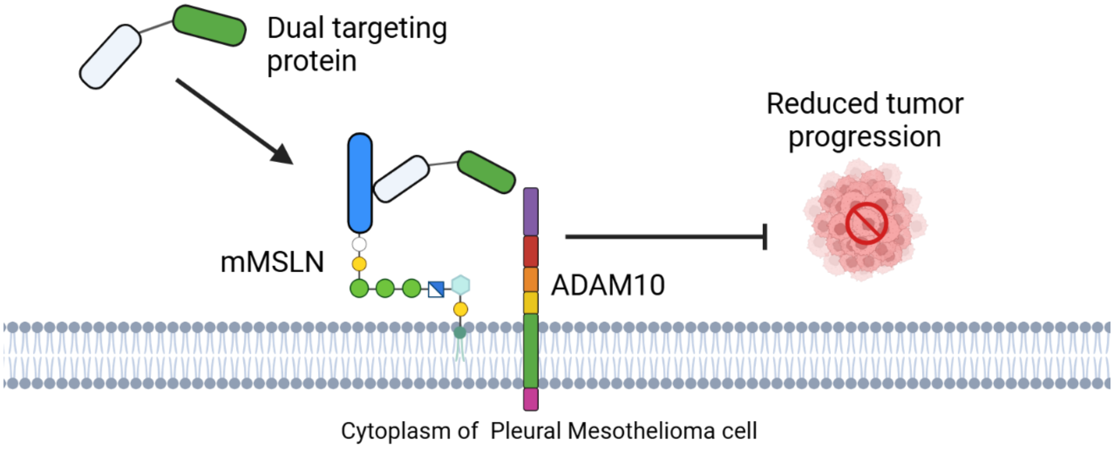

Figure 24) Schematic representation of the Dual-Targeting protein designed to treat PM. The construct simultaneously binds mMSLN, an overexpressed surface antigen on PM cells, and ADAM10, a transmembrane protease involved in tumor progression. Anchoring to mature mesothelin enables site-specific inhibition of ADAM10 at the tumor site, potentially reducing cell migration and proliferation. The cell membrane is shown as a lipid bilayer. This image was created with BioRender.

3 - Material and Methods

3 - Material and Methods

3.1 Identification of ADAM10 inhibitory peptides by phage display

3.1.1 Phage display

The phage display biopanning strategy was used to identify peptide capable of inhibiting ADAM10. Briefly, 100 µL of 10 µg/mL recombinant human ADAM10 (rhADAM10, 936-AD-020, R&D, Minneapolis, USA) solution prepared in 0.1 M $NaHCO_3$ pH 8.6 was added in six wells of a Nunc MaxiSorp 96-well plates (10565981, ThermoFisher, Massachusetts, USA). Plates were incubated overnight at 4°C with gentle agitation in a humidified chamber. The coating solution was removed by inverting the plate and tapping it firmly onto clean absorbent paper. Each well was then filled with 200 µL of blocking buffer (0.1 M $NaHCO_3$ pH 8.6, 5 mg/L BSA) and incubated for 1 h at 4°C. After blocking, the solution was discarded, and plates were washed six times with 200 µL of TBST (50 mM Tris-HCl pH 7.5, 150 mM NaCl, supplemented with 0.1% [v/v] Tween-20). For the first round of panning, 100 µL of the NEB Ph.D.-12 phage display library (E8111L, New England Biolabs, Massachusetts, USA) diluted 1:100 in TBST were added to each well, and plates were incubated with gentle agitation for 10-60 min at room temperature (RT). Unbound phages were removed by 10 consecutive washes with 200 µL TBST. Bound phages were eluted by incubating wells with 100 µL of elution buffer (0.2 M glycine-HCl, pH 2.2, containing 1 mg/mL BSA) for 10 min at RT. The eluates were collected and immediately neutralized with 15 µL of 1M Tris-HCl, pH 9.1. Phages were subsequently amplified [3.1.2 Phages Amplification], and their titer was evaluated [3.1.3 Phage Titer].

For the second round, 100 µL of amplified phages from Round 1 were added to a freshly coated and blocked MaxiSorp plate with rhADAM10 as described above. Binding was allowed for 60 min at RT with gentle agitation. To increase selection, unbound phages were removed by washing with TBST containing 0.5% [v/v] Tween-20. Bound phages were subsequently eluted as described for the first round and amplified.

For the third round, a counter-selection step was performed. 100 µL of amplified phages from the round 2 were incubated in a MaxiSorp plate coated with rhADAM10 that had been pre-incubated with an excess of the ADAM10 inhibitor GI254023X (SML0789, Sigma-Aldrich, Saint Louis, USA). Plates were incubated for 60 min at RT with gentle agitation. Since the active site of ADAM10 was blocked by the inhibitor, the unbound fraction, enriched with phages potentially recognizing the active site were collected. These phages were amplified [3.1.2 Phages Amplification] and their titer evaluated [3.1.3 Phage Titer].

In parallel, a cell-based selection was carried out using H28 cells (CRL-5820, American Type Culture Collection, USA), which overexpress ADAM10 [66]. For the first two rounds, 1×10^5 cells were resuspended in 100 µL of phage solution (NEB Ph.D.-12 phage display library (E8111L) diluted 1:100 in PBS+1% FBS or phage from the previous round). Cells were incubated for 30–60 min at RT with gentle agitation, and unbound phages were removed by centrifugation followed by five additional washes in PBS+1%FBS. Bound phages were eluted using elution buffer as described for plate-based panning and immediately neutralized.

For the counter-selection, H28 cells were pre-treated with 10 µM GI254023X for 30 min at RT to inhibit the ADAM10 active site before incubation. Phages unable to bind the inhibited enzyme were collected from the unbound fraction, amplified, and the titer was evaluated.

3.1.2 Phages Amplification

Phages recovered from the elution step were amplified by infecting *E. coli* ER2738 (E4104, New England BioLabs). The neutralized phage eluate was added to 20 mL of early-log phase *E. coli* ER2738 (OD_{600} 0.01-0.05) grown in LB-Tetracycline medium (10 g/L Baco-Tryptone, 5 g/L Yeast Extract, 5 g/L NaCl, 15 g/L Agar, and 20 mg/L Tetracycline). Cultures were incubated at 37°C with vigorous shaking for 4.5 h to allow phage amplification. Following incubation, amplified phages were recovered by centrifuging the culture twice at 12,000 g for 10 min at 4°C, and collecting the supernatant. Phages were precipitated by incubating the supernatant with 3 mL of 20% [v/v] PEG/2.5 M NaCl overnight at 4° C, followed by a centrifugation at 12,000 g for 15 min at 4°C. The supernatant was discarded, and the resulting phages pellet was resuspended in 1 mL of TBS. To further improve the phage purity, 160 µL of 20% PEG/2.5

M NaCl was added to the resuspended phages and incubated for 60 min at 4°C. The suspension was centrifuged at 14,000 rpm for 10 min at 4°C, and the supernatant was discarded. The final phage pellet was resuspended in 200 µL of TBS. The titer of the amplified phage preparation was subsequently determined in pfu/mL.

3.1.3 Phage Titer

To evaluate phage amplification, 10 mL of LB medium with 20 µg/mL Tetracycline were inoculated with a colony of *E. coli* ER2738 and incubated at 37°C until they reached an OD_{600} of 0.5. Phages were serial diluted up to 10^{11} times in TBS, and 200 µL of bacterial culture were mixed with 10 µL of phage dilution, to carry out the infection. After brief vortexing, infected cells were incubated for 5 min and subsequently transferred into tubes pre-warmed at 45°C with Top Agar (10 g/L Bacto-Tryptone, 5 g/L Yeast extract, 5 g/L NaCl, 7 g/L Agar). The cells were immediately poured onto a prewarmed in LB (10 g Bacto-Triptone, 5 g yeast extract, 5 g NaCl, 15 g/L agar) supplemented with 0.2 mM IPTG (367931 Sigma-Aldrich), and 100 µM Xgal(B1690 ThermoFisher) in petri dishes (627102, Greiner, Kremsmunster, Austria). Plates were incubated overnight at 37°C, and only the plaques in dishes presenting fewer than 100 blue were counted. Phage titer was expressed in pfu/mL.

3.1.4 DNA phage extraction

An overnight culture of *E. coli* ER2738 was diluted 1:100 in LB medium. For each clone, 1 mL of diluted culture was dispensed into 5 mL culture tubes (187262, Greiner, Austria). Thirty blue plaques from each library were picked randomly using sterile wooden sticks and inoculated into the corresponding tubes. Infected cultures were incubated overnight at 37°C, 220 rpm, and they were pelleted by centrifugation at 14,000 rpm for 30 s. Phages were precipitated by adding 200 µL of 20% PEG 2.5 M NaCl for 20 min at RT, followed by centrifugation at 14,000 rpm for 10 min at 4°C and the pellets were resuspended in 100 µL Iodide buffer (10 mM Tris-HCl pH 8, 1 mM EDTA, 4 M NaI). The DNA was precipitated by adding 250 µL of 100% ethanol and incubating 20 min at RT, followed by centrifugation at

14,000 rpm for 10 min at 4°C. Pellets were washed with 500 µL cold 70% ethanol, air-dried, and resuspended in 30 µL nuclease-free water. DNA concentration was measured using Nanodrop spectrophotometer at 260 nm (Implen Nanophotometer N60, Munich, Germany), while DNA purity was assessed using the 260/280 ratio, with values of approximately 1.8 indicating pure DNA [15].

3.1.5 Sanger Sequencing

A 96-well sequencing plate (Eurofins, Ebersberg, Germany) was prepared by dispensing 15 µL of phage DNA (50 ng/µL) in each well. A volume of 2 µL of sequencing primer (5'-CCCTCATAGTTAGCGTAACG-3' 10 pmol/µL) was added to each sample. Sequence quality was assessed using SnapGene Viewer software v8.1.0 (Dotmatics, Boston, USA) and nucleotide sequences were translated using the ExPASy translate tool [207] (https://web.expasy.org/translate/). Only the amino acid region located between the conserved flanking motifs "LVVPFYSHS" and "GGGSAETVE", which corresponds to the 12-mer displayed amino acid, were further analyzed.

3.1.6 Next generation sequencing (NGS)

Phage display sub-libraries from each round of selection were analyzed by NGS using the Illumina MiSeq platform (Eurofins). Briefly, 130 ng of each phage DNA library were amplified by PCR using 0.7 µM of each primer

(forward 5'TCGTCGGCAGCGTCAGATGTGTATAAGAGACAGTTGTCGTCTTTCCAGACGTT3', reverse 5'GTCTCGTGGGCTCGGAGATGTGTATAAGAGACAGGCAAGCTGATAAACCGATACA3'), 5 µL of GoTaq Buffer Green 5x (Promega, Madison, USA), 0.1 µM GoTaq Polymerase (Promega, Madison, USA) and 0.14 mM dNTP. PCR cycles consisted of initial denaturation at 95°C for 45 s, followed by 25 cycles of 95°C for 45 s, 50.6°C for 45 s, and 68°C for 30 s. Amplified products were analyzed on a 0.5% [w/v] agarose gel in 0.5X Tris-Acetate-EDTA buffer (0.5 mM EDTA, 20 mM Tris-HCl pH 8, 10 mM acetic acid) at 120V for 20 min. The band corresponding to 309 bp was excised and purified using the PCR purification kit (Macherey Nage, Duren, Germany). DNA concentration was determined at 260 nm using Nanodrop.

Samples with a concentration above 4 ng/µL (25 µL) were sent to Eurofins for paired-end sequencing with Illumina MiSeq. Adaptors and quality trimming were performed with Trimmomatic-0.39 (Usadel Lab, Aachen, Germany) using the parameters:

"java -jar trimmomatic-0.39.jar PE InputR1.fastq.gz InputR2.gz OutputR1_paired.fq.gz OutputR1_unpaired.fq.gz OutputR2_paired.fq.gz OutputR2_unpaired.fq.gz ILLUMINACLIP:TruSeq3-PE.fa:2:30:10:2:True LEADING:3 TRAILING:3 MINLEN:36".

Paired reads were merged with FLASH using :

"flash OutputR1_paired.fq.gz OutputR2_paired.fq.gz -o merged".

Sequence quality was evaluated with FastQC v0.12.10 (Babraham Bioinformatics, Cambridge, UK). Twelve amino acid variable regions flanked by the conserved motif "LVVPFYSHS" and "GGGSAETVE" were extracted using a custom Python script [Annex 1].

3.1.7 Peptide selection and filtering

A set of 12-mer peptide sequences obtained from phage display sequencing was analyzed using the SAROTUP suite [208,209] (https://i.uestc.edu.cn/sarotup3/index.html) to identify and eliminate target-unrelated peptides. SAROTUP suite includes multiple tools such as TUPScan, MimoScan and SABinder, which evaluate peptide sequences for known non-specific bindings. Only peptides classified as negative across all SAROTUP analysis were retained for further structural and binding site prediction.

The amino acid sequence of mature human ADAM10 (residues 220-748), along with selected peptides and a zinc and calcium ion, were submitted to AlphaFold 3.0 Server [210] (https://alphafoldserver.com/) for structure prediction. Predicted models were evaluated based on i) Predicted Template Modeling score (pTM) >0.5 indicating a reliable overall fold and ii) Interface predicted Template Modeling (ipTM) score >0.8 which corresponds to an acceptable prediction.

Peptide docking simulations were performed using CABS-Dock 2.0 [211] (https://biocomp.chem.uw.edu.pl/CABSdock), employing resolved extracellular domain of ADAM10 (residues 214-654 PDB ID:6BE6) as receptor structure. Docking solutions were filtered based on peptide proximity to the ADAM10 active site, Root Mean Square Deviation (RMSD) values and cluster density, reflecting the stability and consistency of docking positionings.

Selected peptide-ADAM10 complexes were further analyzed using Protein-Ligand Interaction Profiler (https://plip-tool.biotec.tu-dresden.de/plip-web/plip/index) [212], to identify non covalent interactions such as hydrogen bonds, hydrophobic contacts and metal coordination. Effects of peptide binding on the flexibility of the ADAM10 catalytic site and surrounding pockets, were analyzed using CABS-Flex 3.0 (https://lcbio.pl/cabsflex3/) [213]. Docking-derived structures from CABS-Dock 2.0 were uploaded in PDB format, and peptide conformation were refined using peptide-modeling function of CABS-Flex 3.0. The flexibility of residues constituting the HEXXH ADAM10 catalytic motif and residues forming the P1, P2 and P3 substrate binding pockets of ADAM10 were compared before and after peptide binding and peptide intrinsic flexibility was also evaluated independently and upon complex formation. The top-ranked peptides were synthetized by PepMic Co (Suzhou, China) for experimental validation.

3.2 ADAM10 prodomain, A1 VHH and Dual Targeting protein production

3.2.1 Expression vectors

A pET28b plasmid containing the A1 VHH gene [206] fused to the mouse ADAM10 prodomain gene [73], with a (G4S)3 linker and a C-terminal His_6-Tag (Dual Targeting protein), was purchased from Genecust (Dudelange, Luxemburg). The pHEN6 A1 VHH plasmid vector and a pET28a ADAM10 Prodomain plasmid were generated in-house from this commercial plasmid.

Amplification of the A1 VHH gene was performed using the VHH Fw and VHH Rv primers [Table 2] and the amplification of the ADAM10 prodomain was performed using Prod Fw and Prod Rv primers [Table 2]. The VHH amplicon and the empty pHEN6 plasmid were digested with HindIII-HF (R3104S, New England Biolabs) and BstEII-HF (R3162L, New England BioLabs), while the pET28a backbone (69864, Novagen, Darmstadt, Germany) and the ADAM10 Prodomain amplicon were digested with NdeI (R0111S, New England BioLabs) and EcoRI-HF (R3101S, New England BioLabs) following the manufacturer's instructions. Digested DNA fragments were ligated overnight at 16°C using 0.1 U T4 DNA Ligase (EL0011, Thermofisher) and the ligated plasmid were transformed into *E. coli* TOP10 Competent cells (C404010, Invitrogen, Waltham, USA) under selective antibiotic conditions. Plasmids were purified with NucleoSpin Plasmid EasyPure (Macherey-Nagel) and sequenced using the M13 or T7 universal primers [Table 2]. Verified plasmids sequences with SnapGene Viewer software v8.1.0 were amplified in *E. coli* TOP10 (C404003 ThermoFisher) and purified with NucleoSpin Plasmid EasyPure (Macherey-Nagel) before being stored at -20°C.

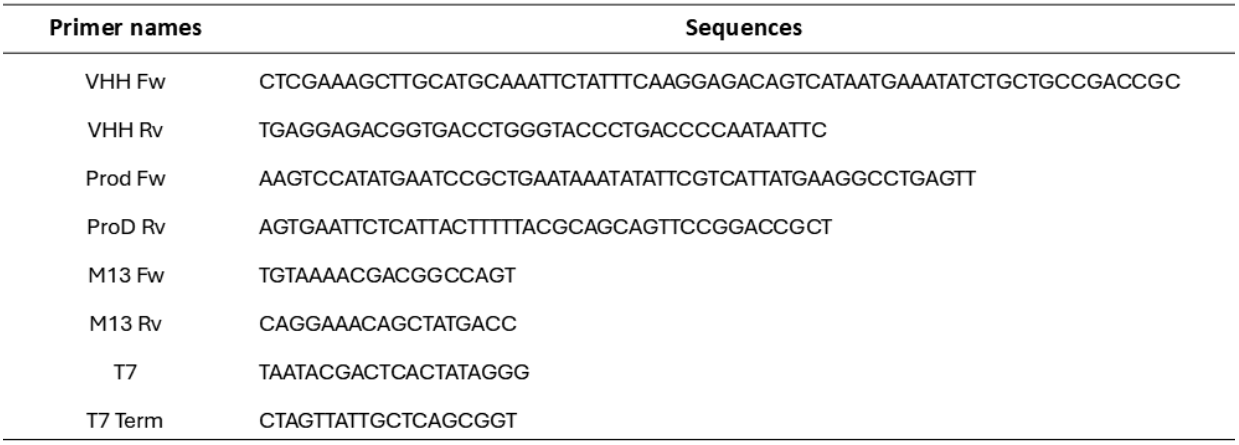

Primer names	**Sequences**
VHH Fw	CTCGAAAGCTTGCATGCAAATTCTATTTCAAGGAGACAGTCATAATGAAATATCTGCTGCCGACCGC
VHH Rv	TGAGGAGACGGTGACCTGGGTACCCTGACCCCAATAATTC
Prod Fw	AAGTCCATATGAATCCGCTGAATAAATATATTCGTCATTATGAAGGCCTGAGTT
ProD Rv	AGTGAATTCTCATTACTTTTTACGCAGCAGTTCCGGACCGCT
M13 Fw	TGTAAAACGACGGCCAGT
M13 Rv	CAGGAAACAGCTATGACC
T7	TAATACGACTCACTATAGGG
T7 Term	CTAGTTATTGCTCAGCGGT

Table 2) Primer sequences for gene amplification and gene sequencing.

3.2.2 Dual Targeting protein expression and purification

The Dual Targeting protein pET28b plasmid was used to transform competent *E. coli* BL21 (DE3) cells (C257I, New England BioLabs). Cultures were grown in Terrific Broth supplemented with 500 µg/mL of kanamycin at 37°C, with shaking at 220 rpm. When cultures reached an OD_{600} of 1.7, recombinant protein expression was induced by adding 1mM of IPTG (367931 Sigma-Aldrich, St. Louis, USA), followed by incubation at 18°C for 12 h.

Induced cells were harvested at 5000 g for 45 min at 4°C, and resuspended in TES buffer (0.2M Tris pH 8.0, 0.5mM EDTA and 0.5M sucrose) supplemented with 150 U Benzonase (E1014, Sigma-Aldrich) and 1 mM $MgCl_2$. After 45 min of incubation at 120 rpm and 4°C, osmotic shock was induced by a four-fold dilution of the TES buffer, followed by incubation for 90 min at 120 rpm at 4°C. The crude extract was clarified by centrifugation (20,000 g, 30 min at 4°C), and the lysate was filtered through a 0.45 µm cut-off PVDF filter (Durapore, Darmstadt, Germany). The resulting supernatant was purified by Ni^{2+} affinity chromatography.

The clarified periplasmic extract was loaded in a 5 mL HisTrap HP column (17524701, Cytiva, Uppsala, Sweden), previously equilibrated with ice cold Buffer (50 mM KP buffer pH 8.0). Bound proteins were eluted with 350 mM of imidazole, and protein concentration was determined by measuring absorbance at 280 nm (A_{280}) using a nanodrop spectrophotometer, applying a theoretical extinction coefficient of 39,435 M^{-1} cm^{-1} calculated with the ProtParam web tool (https://web.expasy.org/protparam/). All the fractions were loaded into a 18% SDS-PAGE for 90 min at 120 V. Pure fractions were pooled and dialyzed against 25 mM Tris-HCl pH 8.0, 100 mM NaCl and 20 % glycerol. The protein was then concentrated with an Amicon 30kDa (UFC910008, Sigma-Aldrich) and the endotoxin levels were reduced via 2 cycles of purification using Pierce High-Capacity Endotoxin Removal Spin Column following provider instruction (88274, ThermoFisher). Purity was assessed by densitometric analysis of Coomassie-stained SDS-PAGE using ImageJ software 1.53k, and expressed as the percentage of the target band relative to the total lane signal. The LPS-pure protein was stored at -80°C. The endotoxin quantities were quantified with Pierce Chromogenic Endotoxin Quant Kit (A39553 ThermoFisher). All steps were performed at 4°C.

3.2.3 A1 VHH production and purification

The A1 VHH was produced following the Redeghieri *et al* [214] protocol. Briefly, the pHEN6 plasmid containing the A1 VHH gene was used to transform chemo-competent *E. coli* WK6 cells. Cultures were grown in Terrific Broth supplemented with 100 µg/mL ampicillin at 37°C, at 220 rpm. When the OD_{600} reached 2-3, the VHH expression was induced with 1mM IPTG, followed by overnight incubation at 18°C.

Cells were harvested by a gentle centrifugation (5,000 g, 30 min at 4°C) and resuspended in cold TES buffer, supplemented with 150 U Benzonase (E1014, Sigma-Aldrich) and 1 mM $MgCl_2$. After 45 min of gentle agitation at 4°C, the osmotic shock was induced by four-fold dilution of the TES buffer, followed by incubation for 90 min at 120 rpm at 4°C. The periplasmic extract was centrifuged at 20,000 g for 30 min at 4°C, and the lysate was filtered through a 0.45 µm cut-off PVDF filter (Durapore). The supernatant was purified by His-Tag affinity chromatography as described for the Dual-Targeting protein. SDS-PAGE pure fractions were pooled and dialyzed against 50 mM Sodium Phosphate (0.09 M NaH_2PO_4, 0.041 M Na_2HPO_4) buffer pH 7.0, and protein concentration was determined by A_{280} absorbance using the nanodrop spectrophotometer, applying a theoretical extinction coefficient of 21,555 M^{-1} cm^{-1} calculated with the ProtParam web tool (https://web.expasy.org/protparam). Purity was assessed by densitometric analysis of Coomassie-stained SDS-PAGE using ImageJ software 1.53k, and expressed as the percentage of the target band relative to the total lane signal. The VHH was concentrated using an Amicom ultra centrifugal Filter 3kDa (UFC500308) and the endotoxin removal was performed as described above. Final aliquots were stored at -20°C.

3.2.4 ADAM10 Prodomain production and purification

The pET28a ADAM10 Prodomain plasmid was used to transform chemo-competent *E. coli* BL21 (DE3) (EC0114, ThermoFisher). Cultures were grown in LB medium supplemented with 500 µg/mL of kanamycin at 37°C, shaking at 220 rpm. When cultures reached an OD_{600} of 0.4, the expression of recombinant protein was induced with 1 mM IPTG, followed by overnight incubation at 18°C.

Cells were harvested by centrifugation (4,500 g for 30 min at 4°C) and resuspended in Buffer A (50 mM Sodium, Phosphate pH 8.0, 10 mM Imidazole, 300 mM NaCl). The suspension was lysed using Emulsiflex-C3 (Avestin, Ottawa, Canada) with three cycles at 20,000 psi, then centrifuged for 20,000 g, 30 min at 4°C. The lysate was filtered through a 0.45 µm cut-off PVDF filter (Durapore).

The filtrate was loaded onto 5 mL HisTag HP column (Cytiva) equilibrated in Buffer A. Elution was performed using a gradient of Buffer B (50 mM sodium phosphate pH 8.0, 300 mM NaCl, 500 mM Imidazole), the fractions corresponding to the elution peaks were analyzed by 18% SDS-PAGE for 60 min at 120 V, and fraction containing the ADAM10 Prodomain were pooled and dialyzed against 50 mM Tris-HCl pH 8.0, 100 mM NaCl and 20% glycerol. Protein concentration was determined by A_{280} absorbance using the nanodrop spectrophotometer, applying a theoretical extinction coefficient of 17,880 M^{-1} cm^{-1} calculated with the ProtParam web tool (https://web.expasy.org/protparam). Purity was assessed by densitometric analysis of Coomassie-stained SDS-PAGE using ImageJ software 1.53k, and expressed as the percentage of the target band relative to the total lane signal. Endotoxin levels were reduced by two cycles of the Pierce High-Capacity Endotoxin Removal system (88274, ThermoFisher). The purified protein was stored at -20°C.

3.3 Biochemical characterization

3.3.1 Circular Dichroism spectroscopy and thermal stability

The secondary structure and thermal stability of the A1 VHH, ADAM10 Prodomain and Dual Targeting protein were analyzed by Circular Dichroism (CD) in the far UV region. Protein samples were prepared in 50 mM sodium phosphate buffer pH 7.0, at a final concentration of 5.3 μM. CD measurements were performed using a JASCO J-1500 spectrophotometer (JASCO Corporation, Tokyo, Germany) equipped with a Peltier cell holder, in a 1 mm quartz cell. Mineral oil was added to prevent sample evaporation. Far-UV CD spectrum were acquired from 185 to 260 nm at 25 °C and 97 °C, using a 1 nm data interval, a data pitch of 0.1 nm, 2 s integration time, a bandwidth of 1 nm and a scanning speed of 50 nm/min. Thermal stability was monitored using linear heating from 25 °C to 97 °C at 0.5 °C/min, acquiring data every 0.3 °C with 4 s integration time and a 1 nm bandwidth.

Thermal transition curves were obtained at 208 nm for A1 VHH, 222 nm for the ADAM10 Prodomain and 218 nm for the Dual Targeting protein. These wavelengths were selected because they showed the largest difference between the native (N) and unfolded (U) states. The onset temperature (T_onset) was extrapolated from the tangent intersections between the pre-transition baseline and the unfolding transition of the raw data. The A1 VHH curves were analyzed based the two states ($N \rightleftharpoons U$) model. Normalization of unfolding curves and the determination of the melting temperature (Tm) were performed as described by Redeghieri *et al* [214] using SigmaPlot 12.0 (Systat Software, San Jose, USA).

3.3.2 Fluorimetry and heat induced denaturation

The tertiary structure of the A1 VHH, ADAM10 Prodomain and the Dual Targeting protein were evaluated using a Cary Eclipse Fluorimeter (Agilent, Santa Clara, USA) equipped with a Peltier multi-cell holder and a 10*0.4 mm pathlength quartz micro cuvette. Proteins were diluted to 5.3 μM in 50 mM sodium phosphate buffer (0.09 M NaH_2PO_4, 0.041 M Na_2HPO_4) pH 7.0 and mineral oil was added on the top of the sample to prevent sample evaporation.

Intrinsic fluorescence spectrum was recorded at 25 °C and 90 °C from 290 nm up to 440 nm, with excitation at 280 nm, the excitation and emission slits were set up at 5 nm, and the detector voltage at 750 V (A1 VHH), 830 V (ADAM10 Prodomain), or 810 V (Dual Targeting protein). Data was collected every 0.5 nm with a scan rate of 30 nm/min.

Heat induced stability of the proteins was monitored by increasing the temperature from 25°C to 97°C, with a heating rate of 1°C/min, with data acquisition every 0.5°C. Fluorescence changes at 351 nm (A1 VHH), 305 nm (ADAM10 Prodomain) and 351 nm (Dual Targeting protein) were used to established the unfolding transition. These wavelengths were chosen because they showed the largest difference in fluorescence intensity between the native and unfolded states for each protein. The transition curves and the normalization was performed as described in the Circular Dichroism paragraph.

3.3.3 Native PAGE

The interaction between rhmMSLN (779802, Biolegend, SanDiego, USA) and either the A1 VHH or the Dual Targeting protein, was evaluated by native PAGE. 2.25 µM of rhmMSLN was incubated alone or with an equimolar concentration between A1 VHH or Dual Targeting protein at 37°C for 15 min. Following incubation, samples were mixed with 5 µL of 4x native loading buffer (62.5 mM Tris-HCl, pH 6.8, 25% [v/v] glycerol, 1% [w/v] Bromophenol Blue).

Samples were loaded onto a 18% or 12% native PAGE gel (12% acrylamide, 0.22 M Tris-HCl pH 8.8, 0.001% [v/v] TEMED, 0.01% [w/v] ammonium persulfate), 1.0 mm. Electrophoresis was carried out at room temperature for 6 h at a constant voltage of 100 V in running buffer (25 mM Tris-HCl pH 8.3 and 192 mM glycine). The gels were stained with InstantBlue Coomassie Protein Stain (119211, Abcam, Cambridge, UK) for 40 min and gel images were acquired at ImageQuant 800 (Amersham, Marlborough, USA).

3.3.4 mMSLN western blot to monitor interaction with the A1 VHH and prodomain

To confirm the capacity of the A1 VHH and the Dual Targeting protein to bind mMSLN a western blot analysis was performed. Briefly, 2.25 µM of rhmMSLN (779802, Biolegend) was migrated into a 12% SDS-PAGE and transferred to a PVDF membrane (88520 Thermofisher) with the Mini Trans-Blot Cell (BioRad, Hercules, USA). Membranes were blocked with BSA 5% [w/v] in TBST. Membranes were incubated with 1 µM of A1 VHH or 1 µM of Dual Targeting protein overnight at 4°C. After three washes in TBST, the goat anti VHH-HRP antibody (AB_2810908, Jackson ImmunoResearch, West Grove, USA) diluted 1:1000 was added for 1 h at room temperature. Detection was performed using Pierce ECL Western Blot substrate (Thermo Scientific 32106) and imaged on Image Quant 800 (Amersham, Marlborough, USA).

3.3.5 Affinity measurements of the A1 VHH and the Dual Targeting protein by Bio-Layer Interferometry experiments

Binding affinities between the A1 or the Dual Targeting protein and rhmMSLN (779802, Biolegend), were assessed using Bio-Layer Interferometry (BLI) with the Octet HTX machine (Sartorius, Gottingen, Germany), available through the Robotein® platform of the BE Instruct-ERIC Centre. A1 VHH and Dual Targeting protein were biotinylated with a ratio 4:1 (biotin:protein) using the EZ-Link Sulfo-NHS-LC-Biotinylation Kit (21435, Thermofisher) and the excess of biotin was removed using Amicom Ultra Centrifugal Filter, 3kDa (UFC500324, Millipore). 27 µg/mL of Dual Targeting protein were immobilized onto streptavidin biosensors (Sartorius) followed by a washing step in KB 1X buffer (Sartorius). The biosensors were then immersed into KB 1X buffer (SA, Sartorius) containing different concentrations of rhmMSLN (200, 100, 50, 25,12.5 and 6.25 nM), to measure the association phase. Subsequently, the biosensor was returned to KB 1X buffer to monitor the dissociation. Association and dissociation rate kinetics were monitored for 60 and 200 s, respectively. To measure the affinity of the A1 VHH, the biotinylated VHH (2.5 µg/mL) was immobilized on SA sensors, after a washing step, the sensors were immersed in rhmMSLN at different concentrations (40, 20, 10, 5, 2.5, 1.25 and 0.65 nM) to measure the association. Subsequently, the biosensors were returned to KB 1X buffer to monitor the dissociation. Association and dissociation rate kinetics were monitored for 300 s and 300 s.

All the experiments were carried out at 30°C in a 384-well black bottom polypropylene microplates (Greiner, Kremsmunster, Austria). The sensorgrams obtained were globally fitted using a 1:1 model to derive the k_{on}, k_{off} and the $K_{D,}$ and the K_D error was calculated using the Equation:

$$\sigma Kd \sqrt{(\frac{\sigma Koff}{Koff})^2 + (\frac{\sigma Kon}{Kon})^2} * Kd$$

Where σ is the error, KD is the dissociation rate constant at the equilibrium, k_{off} is the dissociation rate constant, and k_{on} is the association rate constant. Statistical difference was evaluated using the unpaired student’s t-test analysis on Graph Pad 8.0 (GraphPad software, San Diego USA).

3.3.6 ADAM10 inhibition assay

The inhibitory activity of the ADAM10 Prodomain and the Dual Targeting protein were evaluated by following the cleavage of the fluorogenic Mca-KPLG~L-Dpa-AR-NH_2 substrate (BML-P235, Enzo, Farmingdale, USA) by ADAM10. 1 nM of rhADAM10 ECD (R&D System) was incubated in 25 mM Tris pH 9.0, 2 µM ZnCl2, 0.005% [w/v] Brij-35 with different concentrations of the ADAM10 Prodomain, the Dual-Targeting protein (2, 1, 0.75, 0.5, 0.38, 0.25, 0.19, 0.125, 0.06 and 0.03 µM) or the inhibitory peptides identified with phage display (100, 20, 5, 1 and 0.5 µM) for 15 min at 37°C. 15 µM of Mca-KPLG~L-Dpa-AR-NH_2 substrate was added, and the kinetics were monitor for 60 min at 37 °C by fluorescence with excitation and emission wavelength of, respectively, 320 nm and 405 nm in a SpectraMax i3 (Molecular Devices, San Jose, USA). The deadtime between the addition of the substrate and the first measurement was about 180 s. All the experiments were performed in triplicate.

The residual activity was evaluated by measuring the initial velocity (v_i) of the reaction in the presence of different concentrations of the ADAM10 Prodomain or the Dual Targeting protein. The IC_{50} was determined with GraphPad 8.0 using the non-linear regression model, four-parameter logistic model, inhibitor vs response. The statistical difference between ADAM10 residual activity after the treatment with ADAM10 Prodomain or Dual targeting protein, was evaluated using the unpaired student's t-test analysis on Graph Pad 8.0.

3.4 Cell-based characterization of ADAM10 Prodomain, A1 VHH and Dual Targeting protein

3.4.1 Cell culture

Biphasic PM cell line MSTO-211H (CRL-2081, American Type Culture Collection, Manassas, USA) and Sarcomatoid PM H28 (CRL-5820, American Type Culture Collection) cell line were cultured in RPMI-1640 medium with L-Glutamine (Westburg, Leusden, Netherlands) supplemented with 10% [v/v] heat-inactivated fetal bovine serum (FBS, Gibco) and 5% [v/v] of Pen-Strep (15140122, Gibco). Non-malignant mesothelial cell line Met5a (CRL-9444, American Type Culture Collection) was cultured in Medium 199 (Gibco) supplemented with 10% [v/v] FBS, 5% [v/v] Pen-Strep, 3.3 nM epidermal growth factor (E9644 Sigma-Aldrich), 400 nM hydrocortisone (H3160, Sigma-Aldrich), 20 mM HEPES (15630080 Gibco).

3.4.2 Cell metabolic activity assay

Cell metabolic activity was assessed with the MTT assay. 4,000 H28 cells, 6,000 MSTO-211H cells or 8,000 Met5a cells were plated per well in a 96-well plate (3596 Cornings, NY, USA) and seeded overnight. After 24 h, cells were treated with the ADAM10 Prodomain, the Dual Targeting protein, or the A1 VHH at concentrations of 5, 2.5, 1.25, 0.6, 0.3 and 0.15 µM in complete medium at 37°C with 5% CO_2 for 72 h. As control, cells were treated with complete medium containing the same concentrations of protein buffer used for the tested recombinant proteins, in order to account for any buffer-related effects.

After a washing with 200 µL PBS, 100 µL of 1 mg/mL MTT (M2128, Sigma-Aldrich) in complete medium were added into each well and incubated for 3 h at 37°C, 5% CO_2. Purple formazan crystals were solubilized adding in each well 100 µL of 10% [v/v] SDS, 0.01M HCl, O/N at 37°C. Absorbance was measured at 590 nm in a SpectraMax Plus 384 (Molecular devices, San Jose, USA). The absorbance values were normalized to those of the control wells and expressed as a percentage. Cell metabolic activity curve was determined using the Nonlinear regression function, log(inhibitor) vs response – Variable slope (four parameters) on GraphPad 8.0. The statistical difference was evaluated using the two-way ANOVA analysis on Graph Pad 8.0.

3.4.3 Clonogenic Assay

To assess long-term cell proliferative capacity, 5,000 H28, 8,000 MSTO-211H or 10,000 Met5a cells were seeded in 6-well culture plates (3516 Corning, NY, USA) and incubated overnight at 37°C, 5% CO_2. Cells were then treated for 7 days with the ADAM10 Prodomain, the A1 VHH or the Dual Targeting protein at 5, 2.5, 1.25 µM or control. As control, cells were treated with complete medium containing the same concentrations of protein buffer used for the tested recombinant proteins, in order to account for any buffer-related effects.

At the end of the incubation, cells were washed twice with 2 mL PBS, fixed in 4% formol (Solveco Chemicals, Rosersberg, Sweden) for 15 min, and stained with 5% [w/v] of crystal violet (Sigma-Aldrich). Plates were washed in water, air-dried overnight, and the dye was solubilized in 5% [w/v] SDS. The absorbance was measured at 595 nm in a 96-well plate (3596 Corning) using SpectraMax Plus 384. Data was normalized to those of untreated controls. The statistical difference was evaluated using the unpaired student's t-test analysis or one-way ANOVA with Dunnett's multiple comparison on Graph Pad 8.0.

3.4.4 N-Cadherin cleavage

N-cadherin shedding was used as a readout of ADAM10 inhibition. $1*10^6$ of MSTO-211H, H28 or Met5a cells were seeded in a 10 cm^2 petri dish (627102, Greiner, Kremsmunster, Austria) and incubated at 37°C with 5% CO_2 for 48 h. Cells were treated with the ADAM10 Prodomain or the Dual Targeting protein in serum free medium for 48 h at 37°C. Conditioned medium was collected and concentrated using a 50kDa Amicom (UFC905008, Millipore (Merck), Darmstadt, Germany) to isolate the 95kDa N-terminal N-cadherin Fragment (NTF). Cells were washed twice with 5 mL of PBS, and proteins were extracted with Lysis Buffer (Cell Signaling, Danvers, USA) supplemented with phosSTOP (Roche, Mannheim, Germany) and Protease inhibitor (Roche). The extracted proteins were quantified using the Pierce BCA Protein Assay Kit (ThermoFisher, Waltham, USA) and 10 µg of protein were loaded in a 12% SDS-PAGE. The proteins were transferred to a PVDF membrane (88520 Thermofisher) with the Mini Trans-Blot Cell (BioRad, Hercules, USA). The membrane was blocked in 5% [w/v] BSA or 5% [w/v] dried milk for 1 h at RT, and incubated first with a rabbit anti N-cadherin antibody 1:1000 (4061 Cell Signaling, Danvers, USA) or rabbit anti actin antibody 1:1000 (A2066, Sigma Aldrich) O/N at 4°C. After three washes with TBST (20 mM Tris-HCl, 150 mM NaCl, 0.1% [v/v] Tween-20) the membranes were incubated with 1:1000 goat anti-rabbit antibody coupled to HRP (7074, Cell signaling) for 1 h at RT. Binding were detected with Pierce ECL Western Blot Substrate using Image Quant 800 Band intensity was quantified with ImageJ 1.53k (National Institutes of Health, Bethesda, USA) and normalized with the actin band. All the experiments were performed in triplicate using three different protein batches.

3.4.5 Cell lysate western blot

Extracted proteins of MSTO-211H, H28 or Met5a cell lines, were separated by a 12% or 18% SDS-PAGE and transferred to PVDF membrane (88520, ThermoFisher). Membranes were blocked with BSA 5% [w/v] or non-fat dry milk 5% [w/v], in TBST. Primary antibodies were used at the following concentration: 1:1000 rabbit anti mMSLN antibody (250519, Abbiotec, San Diego, USA), 1 µg/mL A1 VHH, 1 µg/mL Dual Targeting protein, 1:1000 rabbit anti-ADAM10 antibody (EPR5622, Abcam, Cambridge, UK), or 1:1000 rabbit anti actin antibody (A2066, Sigma-Aldrich). Following an overnight incubation at 4°C with gentle agitation, the membranes were incubated with 1:1000 goat anti-Mouse-HRP (31420, ThermoFisher) or 1:1000 goat anti-Rabbit-HRP (31460, ThermoFisher), secondary antibody for 1 h RT with gentle agitation. Detection was performed using Pierce ECL Western blot substrate (32106, ThermoFisher) and imaged on Image Quant 800 (Amersham, Marlborough, USA).

3.4.6 Wound healing assay

Cell migration was assessed by wound healing assay (scratch assay). 40,000 MSTO-211H, 10,000 H28 and 30,000 Met5a cells were seeded in a 96 well flat bottom plate (Sartorius BA-04855) in complete medium. Upon reaching confluence, monolayers were scratched using Sartorius 96-well WoundMaker, washed twice to remove debris, and incubated in medium containing 2% FBS, 10^{-6} M cytosine B-D arabinofuranoside hydrochloride, an antineoplastic agent, treated with 5 µM of anti A1 VHH, ADAM10 Prodomain and Dual Targeting protein or buffer control. Cells were imaged every 4 h for 48 h in an Incucyte S3 Live-Cell Analysis System (Sartorius Lab Instruments GmbH & Co. KG Goettingen, Germany) using the scratch wound settings for with a 10X focus 37°C, 5% CO_2.

The resulting confluence percentage was determined using the Incucyte Cell-by-Cell Analysis Software Module (Sartorius Lab Instruments GmbH & Co.KG). The algorithm was trained using untreated cells from 0 to 48 h, and the same algorithm was used for each triplicate. The significance of the results was evaluated by analyzing the last timing using two-way ANOVA followed by Sidak multiple comparison test with Graph Pad 8.0.

To evaluate whether the Dual Targeting protein selectively affects the migration of cancerous cells co-expressing mMSLN and ADAM10, both malignant cells (MSTO-211H and H28) and non-malignant cells (Met5a) were treated with 2% FBS, 10^{-6} M cytosine B-D arabinofuranoside hydrochloride, an antineoplastic agent, and 5 µM of inhibitors (anti A1 VHH, ADAM10 Prodomain or Dual Targeting protein). Cells were incubated at 37°C for 3 h before being scratched using the scratch 96-well Woundmaker (Sartorius). The cells were washed 5 times and incubated in complete medium for 48 h in Incucyte S3 Live-Cell Analysis System (Sartorius Lab Instruments GmbH & Co. KG Goettingen, Germany) under identical Incucyte condition of the one above.

3.4.7 Flow cytometry

The binding specificity of the A1 VHH or the Dual Targeting protein to PM cell lines was analyzed by flow cytometry. A total of $1*10^5$ cells of Met5a, MSTO-211H and H28 were seeded in a 96 well plate round bottom (CLS3795, Corning). The cells were incubated with 1 µM of A1 VHH, Dual Targeting protein or PBS for 1h at 4°C.

Following a washing with 200 µL of PBS supplemented with 1% [v/v] FBS, cells were incubated with 1:100 goat anti VHH-Alexa Fluor 647 (128-605-230, Jackson ImmunoResearch, West Grove, USA), while the control with 1:100 rabbit anti mMSLN Alexa Fluor 647 (ab252135, Abcam) as positive control for 1 h at 4°C. Samples were washed three times with 200 µL PBS 1% [v/v] FBS, before being analyzed on a BD FACSCanto Bioanalyzer System (BD Bioscience, San Jose, USA). Analyses were carried out with FlowJo software (FlowJo, Ashland, USA)

3.5 *In vivo* characterization

3.5.1 Mouse model

Protocols used in this study were approved by the Animal Ethical Committee of the University of Liège (ethical approval number 2846) and male BALB/cJRj mice and Athymic nude mice weeks aged 6 to 8 weeks (Janvier Labs, St. Berthevin, France) have been used. Mice were randomly divided into experimental groups. Total sample size was determined with the “G Power” software using the “Wilcoxon-Mann-Whitney” type t test.

3.5.2 Dual Targeting protein plasma clearance

To capacity of the Dual-Targeting protein to reach the plasma compartment was evaluated in 12 male BALB/CJRj mice (8 weeks old, Janvier labs). Mice received 100 µL of intraperitoneal injections of endotoxin-free Dual-Targeting protein at 40 mg/kg (1 µmol/kg), 10 mg/kg (0.25 µmol/kg) and 1 mg/kg (0.02 µmol/kg) or control. As control, cells were treated with complete medium containing the same concentrations of Dual Targeting protein storage buffer used for the tested recombinant proteins, in order to account for any buffer-related effects. Each mouse received two injections, administrated 24 h apart.

Blood samples were collected from the tail vein 1 h post-injection via tail vein puncture using microhematocrit tubes, and complete blood was obtained from the abdominal aorta at 4 h post-injection following euthanasia. Blood was transferred into Microtainer K2E blood collection tubes (365975, BD, New Jersey, USA). Plasma was obtained by centrifuging at maximum speed for 15 min at 4°C, and the supernatant was stored at -80°C until further analysis.

Quantification of the Dual Targeting protein in plasma was carried out using a VHH Affinity Ligand ELISA (LO1033, Genscript, Piscataway, USA). This ELISA uses a high affinity anti VHH antibody immobilized on the plate to capture the dual Targeting protein from plasma, followed by detection with an HRP-conjugated antibody, generating a colorimetric signal proportional to the protein concentration. Plasma samples were diluted 1:10 in Sample Dilution Buffer (LO1033, Genscript) to ensure that their concentration fell within the range of the calibration curve (from 10 pg/mL to 640 pg/mL). Samples were further revealed at 450 nm at SpectraMax i3 (Molecular Devices). Data was analyzed using GraphPad Prism version 8.0. The statistical significance was determined using the unpaired student's t-test or one-way ANOVA with Dunnet's multiple comparison analysis.

3.5.3 Dual Targeting protein tumor progression evaluation

To evaluate the ability of the Dual Targeting protein to slow down tumor progression, 25 male Athymic nude mice (6 weeks, Janvier labs) were subcutaneously injected with MSTO-211H cells. For each injection, $2x10^6$ cells were resuspended in a 1:1 mixture of Matrigel (Corning 354234, NY, USA) in complete medium. Mice were anesthetized with isoflurane for approximately 6 min, and 200 µL of 1:1 Matrigel-cell suspension were injected subcutaneously into both flanks.

Following tumor cell implantation, mice were treated three times per week with the endotoxin-free 40mg/kg or 10mg/kg of Dual-Targeting protein (1 µm/kg or 0.25 µm/kg), 40mg/kg or 10mg/kg ADAM10 Prodomain (2.23 µm/kg or 0.56 µm/kg), or control. As control, cells were treated with PBS containing the same concentrations of Dual Targeting protein storage buffer used for the tested recombinant proteins, in order to account for any buffer-related effects.

Tumor volume was monitored starting on day 7 post-implantation and it was performed three times per week using a caliper. The volume (mm^3) was calculated according to:

$$Tumor\ volume\ (mm^3) = 0.4 * Flank\ length * (Flank\ width^2)$$

The mean tumor volume per mouse was calculated from the two flanks. Body weight was also recorded three times per week. After 38 days, mice were anesthetized by isoflurane for 6 min followed by cervical dislocation, and tumors were excised and weighed.

3.5.4 Immunohistochemical evaluation of Ki-67 in xenograft tumors

To evaluate the effects of the drug treatments on cell proliferation, MSTO-211H xenograft tumors were excised and fixed in 4% paraformaldehyde solution (ThermoFisher). Tissue section (5 µm) made using Leica Biosystems microtome (Nussloch, Germany) were mounted on glass microscope slides. Sections were deparaffinized by sequential incubations in xylene (from 100% to 70%) and rehydrated through decreasing concentrations of ethanol to distilled water (from 100% to 70%), using a Leica Autostainer XL System (Nussloch, Germany).

Antigen retrieval was performed by heat-induced epitope retrieval at 120°C for 10 min in citrate buffer (pH 6.0 S369 Dako, Carpinteria, USA). Endogenous peroxidase activity was quenched with 3% [v/v] hydrogen peroxide (Merck) for 20 min, and non-specific binding was minimized by incubation with animal-free blocking buffer (Cell Signaling, Danvers, USA) for 10 min at room temperature. The slides were then incubated with an anti Ki-67 antibody (1:500 ab16667, Abcam) for 1 h at room temperature to assess cell proliferation. In parallel, adjacent tissue sections were incubated with an anti CD31 antibody (1:200 Ab28364, Abcam) for 1 h at room temperature to evaluate tumor vascularization.

After two washing in PBS, sections were incubated for 30 min at room temperature with EnVision+HRP-labelled (K4003, Dako). Signal detection was performed using 3,3' diaminobenzidine tetrachloride (DAB) substrate (Cell Signaling Technology, #877-616) for 15 min at room temperature. Sections were counterstained with hematoxylin (Merck) for 30 s, dehydrated through graded alcohols (from 70% to 100%), cleared in xylene (ThermoFisher), and mounted using Eukitt mounting medium (25608, SigmaAldrich). Slides were digitized using the NanoZoomer 2.0-HT (Hamamatsu Photonics, Hamamatsu, Japan) at 10x magnification with manual focus. Quantification of DAB of the digitized images was performed using QuPath 0.6.0 (University of Edinburgh, Edinburgh, UK). The statistical significance was determined using one-way ANOVA with Dunnet's multiple comparison.

4 – Results

4 – Results

4.1 Recombinant ADAM10 extracellular domain expression in *E. coli*

Our initial project aimed to produce recombinant human ADAM10 in *E. coli* to perform phage display selections of inhibitory peptides using self-produced ADAM10 ECD [221]. To this end, we cloned the extracellular domain of human ADAM10 ECD (amino acids 218-672) into a pET28a expression vector for production in *E. coli*. However, due to the absence of the prodomain (required for proper folding) and the lack of eukaryotic post-translational modifications such as glycosylation, ADAM10 was predominantly expressed as inclusion bodies. Several refolding strategies were tested. Inclusion bodies separated from other cellular debris, were solubilized using different concentrations of urea or guanidine hydrochloride, followed by refolding attempts based on immobilized metal affinity chromatography (IMAC), in which the denaturant was gradually removed to promote correct folding. Despite extensive optimization we were unable to obtain properly folded and functional ADAM10.

To improve solubility, we also tested the expression of the extracellular domain fused to a SUMO tag at the C-ter, which is known to enhance solubility, stability and expression levels of recombinant proteins. Although this approach was already been successfully used to produce ADAM10 ECD by Wang *et al* [221]*, A*DAM10 ECD still accumulated as inclusion bodies under paper described conditions.

Given the inability to obtain soluble, correctly folded ADAM10 in *E. coli* this production strategy was discontinued, and subsequent experiments were performed using commercially available recombinant human ADAM10 (rhADAM10) for phage display applications.

4.2 Phage Display and peptide discovery

4.2.1 Peptides isolation, with phage display, against recombinant human ADAM10

To identify peptides inhibiting ADAM10, a phage display approach was used. rhADAM10 ECD (R&D System) was immobilized onto a 96 well plate by direct adsorption overnight at 4°C. Two rounds of biopanning were performed starting from the 12-mer NEB phage display library (New England BioLabs) with a diversity of approximately $1x10^{13}$ pfu/mL. A third round of selection was carried out in the presence of an excess of GI254023X, a small inhibitor of ADAM10, to perform a counter-selection, aimed at enriching peptides that compete with the GI254023X binding site, and thus targeting the ADAM10 active site. From each round, thirty individual colonies were randomly selected, and the peptide-coding gene were sequenced. A substantial proportion of the analyzed clones (in a range of 33% up to 100%) lacked a peptide insert and therefore correspondent to wild-type phages. Interestingly, the proportion of wild type phage increased with successive panning rounds, likely reflecting their high prevalence in the naïve library and their replicative advantage, as previously reported by Sloth *et al* [215]. These results are summarized in Table 3 A, where A10-1 and A10-2 correspond to the first and second biopanning rounds, respectively. A10-N3 denotes the round of counter selection round performed in the presence of GI254023X excess.

Using rhADAM10 as target for the bio-panning may lead to the selection of peptides failing to recognize the enzyme on the surface of the cells, as the recombinant protein may exhibit a different glycosylation profile, alternative folding, or expose epitopes that are masked when ADAM10 is in the membrane context. To address these potential limitations, an alternative phage display strategy based on whole-cell panning was implemented using H28 cell line. This cell line was selected since it overexpresses ADAM10 at the cell surface [66]. Panning was carried out using the 12-mer NEB phage display library (New England BioLabs), as described above. Two rounds of selection were carried out on H28 cells to enrich peptides bindings to surface-expressed ADAM10. An additional round of counter selection was performed in the presence of the ADAM10 inhibitor GI254023X to preferentially enrich peptides targeting the catalytic region of ADAM10.

From each selection round, thirty individual colonies were randomly selected, and the peptides coding genes were sequenced. Due to the high prevalence of wild type phages observed at each cycle (~70 %), an additional screening step was introduced following DNA extraction. The DNA fragment encompassing the randomized peptide insert within the G3P gene was amplified by PCR and analyzed by agarose gel electrophoresis. Clones containing 12-mer peptide were identified by the presence of a fragment approximately 50 bp larger than the wild type amplicon. This strategy reduced the proportion of wild type clones sent to sequencing, as shown in Table 3 B. In this table CA10-1 and CA10-2 correspond to the first and second rounds of cell-based biopanning, respectively. CA10-N3 denotes the counter selection round performed in the presence of an excess of GI254023X.

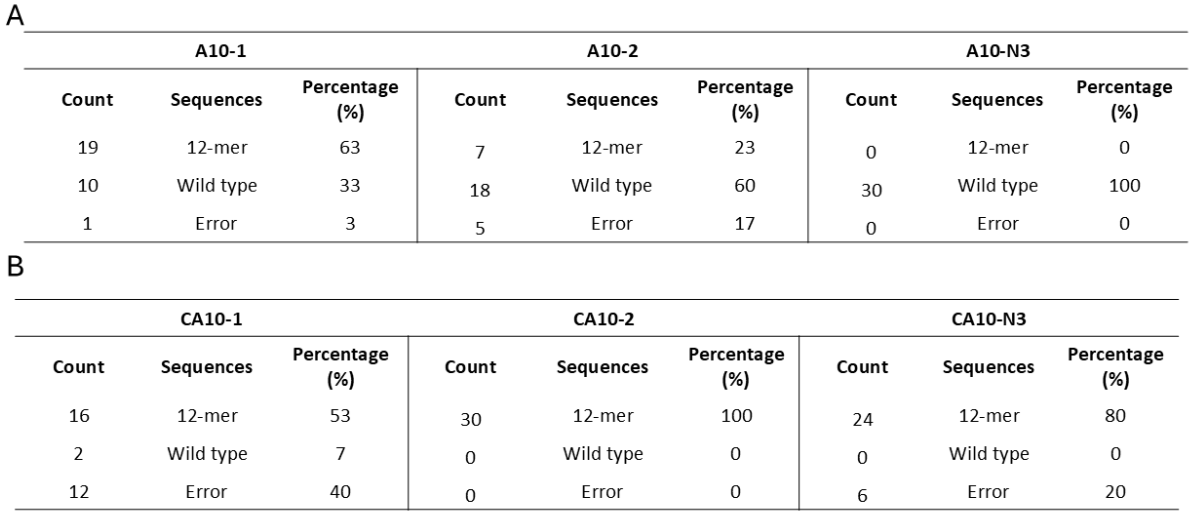

A

A10-1			A10-2			A10-N3		
Count	Sequences	Percentage (%)	Count	Sequences	Percentage (%)	Count	Sequences	Percentage (%)
19	12-mer	63	7	12-mer	23	0	12-mer	0
10	Wild type	33	18	Wild type	60	30	Wild type	100
1	Error	3	5	Error	17	0	Error	0

B

CA10-1			CA10-2			CA10-N3		
Count	Sequences	Percentage (%)	Count	Sequences	Percentage (%)	Count	Sequences	Percentage (%)
16	12-mer	53	30	12-mer	100	24	12-mer	80
2	Wild type	7	0	Wild type	0	0	Wild type	0
12	Error	40	0	Error	0	6	Error	20

Table 3) Phage display peptide sequences identified by Sanger sequencing, A) Peptides identified at each round of biopanning using recombiant ADAM10 extracellular domain as the target (A10 libraries). A10-n indicates the biopanning round. A10-N3 represents the round of counter selection round performed in the presence of an excess of GI254023X, an ADAM10 inhibitor. Thirthty clones were sequenced per round. Wild type phages lacking the pepitde insert, as well as sequencing error, are reported together with their relative frequencies. B) Peptides identified from biopanning on H28 cells overexpressing ADAM10 (CA10 libraries). CA10-n indicates the biopanning round. CA10-N3 represents the counter selection round with GI254023X. The reduced proportion of wild type phages observed in the CA10 libraries is attributable to an additional PCR-based screening step, as describes in the main text, which selectively enriched for peptide-displaying phages prior to sequencing.

Despite the implementation of both selection strategies, Sanger sequencing did not reveal a consistent enrichment of specific peptide sequences probably due to the limited number of sequences analyzed. These findings suggest that Sanger sequencing is insufficient to comprehensively assess peptide enrichment and diversity in phage display experiments.

4.2.2 Peptides found with Next Generation Sequencing (NGS)

Given the limited resolution of Sanger sequencing, NGS was used to improve peptides discovery as demonstrated by Sell *et al.* [216]. NGS analysis was performed on phage pools derived from both the rhADAM10 ECD based panning and the H28 cell-based panning strategies. This approach substantially increased the number of sequences analyzed, with up to ~80,000 reads per condition, enabling a more robust evaluation of peptide enrichment. Notably, a high proportion of wild type phages (~95%) were detected, in agreement with Sanger results discussed above. This phenomenon may arise from several factors, including non-specific interaction mediated by native phage coat proteins or selective replicative advantage of wild type phages, which can rapidly outgrow during amplification [217]. Importantly, the predominance of wild-type phages, may itself contribute to reduced enrichment efficiency, as their overrepresentation can competitively suppress the amplification and detection of insert-bearing phages, ultimately limiting the number of selected peptide sequences recovered. In terms of sequence diversity, a greater variety of peptides was identified when using the rhADAM10 (~86%, A10-n libraries) as the selection target than the H28 cell (~27%, CA10-n libraries).

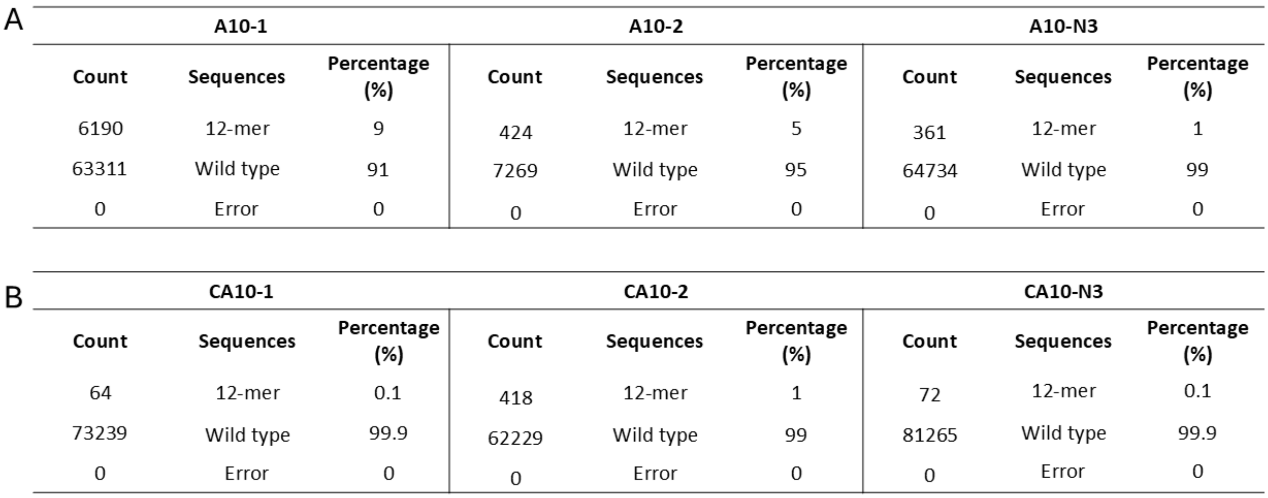

A

A10-1			A10-2			A10-N3		
Count	Sequences	Percentage (%)	Count	Sequences	Percentage (%)	Count	Sequences	Percentage (%)
6190	12-mer	9	424	12-mer	5	361	12-mer	1
63311	Wild type	91	7269	Wild type	95	64734	Wild type	99
0	Error	0	0	Error	0	0	Error	0

B

CA10-1			CA10-2			CA10-N3		
Count	Sequences	Percentage (%)	Count	Sequences	Percentage (%)	Count	Sequences	Percentage (%)
64	12-mer	0.1	418	12-mer	1	72	12-mer	0.1
73239	Wild type	99.9	62229	Wild type	99	81265	Wild type	99.9
0	Error	0	0	Error	0	0	Error	0

Table 4) NGS analysis of phage display peptide libraries across biopanning rounds A) peptide sequences identified at each round of biopanning performed against the recombinant extracellular domain of ADAM10 (A10 libraries) B) peptide sequences obtained from biopanning on H28 cells overexpressing ADMA10 (CA10 libraries). For each condition, the total number of reads corresponding to 12-mer peptide insert, wild-type phages, and sequencing errors are reported together with their relative percentage (%).

The combined dataset obtained from Sanger and NGS sequencing was filtered using SAROTUP suite to eliminate known target-unrelated peptides (TUPs). TUPs are peptide sequences that become enriched during phage display selections due to non-specific interactions with experimental components, such as plastic, blocking reagents, or phage coat proteins, rather than specific binding to the intended target. The SAROTUP suite identifies such sequences by comparison with databases of peptides repeatedly reported across unrelated phage display experiments. Using this approach, several high-frequency sequences, including GTNWSIHENNMG and YRVDLRPD, were identified as plastic binders and excluded from further analysis. The top five sequences from each round were compared to assess potential enrichment as shown in Table 5.

A

		CA10-1		CA10-2		CA10-N3	
Name	**Sequence**	**Count**	**Percentage of enrichment (%)**	**Count**	**Percentage of enrichment (%)**	**Count**	**Percentage of enrichment (%)**
Anti ADAM10-1	TSGTMQTNPLPV	4	6	29	7	3	4
Anti ADAM10-2	RLPLTHEADFSM	3	5	-	-	-	-
Anti ADAM10-3	FNPAASTAARFS	1	2	1	0.2	-	-
Anti ADAM10-4	GMWRGYHEGHAH	1	2	10	2	17	24
Anti ADAM10-5	THASTRQPASSS	1	2	14	3	-	-
Anti ADAM10-6	SFSSHSSVFSVV	-	-	9	2	-	-
Anti ADAM10-7	TNAAETVP	-	-	7	2	1	2
Anti ADAM10-8	GGPAHLIVPG	-	-	-	-	1	2
Anti ADAM10-9	DLGHGRPGTGGN	-	-	-	-	1	2

B

		A10-1		A10-2		A10-N3	
Name	**Sequence**	**Count**	**Percentage of enrichment (%)**	**Count**	**Percentage of enrichment (%)**	**Count**	**Percentage of enrichment (%)**
Anti ADAM10-1	TSGTMQTNPLPV	138	2	16	4	21	5.8
Anti ADAM10-6	SFSSHSSVFSVV	19	0.3	-	-	9	2.5
Anti ADAM10-8	GGPAHLIVPG	-	-	-	-	4	1.0
Anti ADAM10-9	DLGHGRPGTGGN	-	-	2	0.5	-	-
Anti ADAM10-10	AYTVEDSKLARH	22	0.3	3	0.7	-	-
Anti ADAM10-11	GLQTAYKRDVNN	15	0.2	-	-	-	-
Anti ADAM10-12	RFHHDITRHIVP	15	0.2	-	-	1	0.3
Anti ADAM10-13	TLKNNAVSLARN	-	-	4	1	-	-
Anti ADAM10-14	DVRLSRTPPTTS	-	-	5	1.1	-	-
Anti ADAM10-15	ASKHIYHGPSAA	4	0.1	3	0.7	-	-
Anti ADAM10-16	AVRYGYHQANNN	-	-	-	-	9	2.5
Anti ADAM10-17	SGTNWSIHENNMG	17	0.3	15	3.5	3	0.8

Table 5) Representative phage display peptides identified by phage display across biopanning rounds. A) Peptides selected against recombinant ADAM10 ECD (CA10-n), including a negative selection step using the ADAM10 inhibitor GI254023X (CA10-N3).Peptide sequences were identified by NGS and Sanger sequencing, and their relative enrichment (%) across rounds is reported. A marked enrichment was observed the for peptide anti ADAM10-4. B) Peptides identified by biopanning on H28 cells overexpressing ADAM10 (A10-n), with counter selection performed using GI254023X (A10-N3). The peptide anti ADAM10-1 was consistently detected across multiple rounds. Although only modest enrichment was observed. Several peptides, including anti ADAM10-1, anti ADAM10-6, anti ADAM10-8, anti ADAM10-9, were isolated using both recombinant protein based and cell based selection strategies (blue) .

Despite the high background of wild type phages, a modest enrichment of the anti ADAM10-4 sequence was observed (23.61%) following counter-selection with the ADAM10 inhibitor GI254023X. While presence of wild-type phages may have influenced the apparent enrichment efficacy, the consistent selection of anti ADAM10-4 across rounds suggests an interaction with ADAM10. Using two complementary panning strategies, rhADAM10 ECD based panning and H28 cell-based panning, four peptides sequences (anti ADAM10-1, -6, -8, -9) were independently identified by both approaches.

4.2.3 Docking analysis between peptides and ADAM10

The nine most representative peptide-candidates identified at the third round of biopanning by NGS were subjected to structural docking using CABS-Dock 2.0 server. These peptides were chosen based on their enrichment profiles across both rhADAM10 based and H28 cell-based panning strategies, although not all candidates were shared between the two approaches. Initial attempts to model peptide-ADAM10 complexes via AlphaFold 3 yielded low ipTM scores below 0.8, indicating unreliable predictions. Therefore, docking simulations were performed using CABS-Dock 2.0, with the mature extracellular domain of ADAM10 (220AA-672AA) as the receptor and each peptide as input.

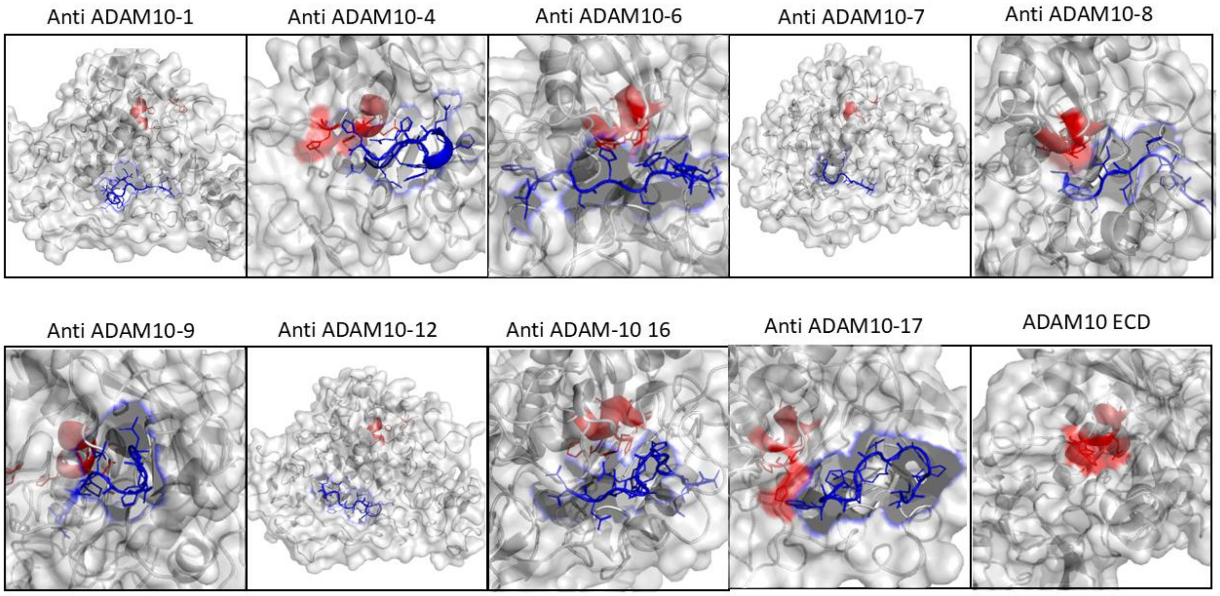

Figure 25) CABS-Dock 2.0 interaction prediction between selected peptides and ADAM10. Predicted binding of the most promising peptides (blue) to ADAM10 (grey), with proximity to the HEXXH (red), the conserved zinc-binding catalytic motif of the ADAM10 metalloprotease domain. Peptides anti ADAM10-4, 6, 8, 9, 16, 17 binds closely to the active site of ADAM10. Anti ADAM10-1, 7 and 12 are considered non relevant due to their distal binding locations. ADAM10 ECD is the representation of the extracellular domain of ADAM10 with no peptide interactions.

Despite the absence of a clear third-round enrichment, several peptides from the A10 and CA10 libraries were found to bind near the ADAM10 active site using the CABS-Dock 2.0 server [Figure 25]. The peptide models generated by CABS-Dock 2.0 that interacted in proximity of the active site exhibited a low average RMSD of less than 5 Å which indicates a high convergence of peptide docking positionings across independent simulations. These low RMSD values indicate high structural similarity suggesting stable binding and specific interactions of the predicted complex [211]. To assess structural stability, molecular dynamics simulation was performed using CABS-Flex 3.0 suite. Selected CABS-Dock 2.0 models, that were positioned in proximity to the ADAM10 catalytic site and exhibited a root mean square deviation (RMSD) below 5 Å, were further analyzed using the CABS-Flex 3.0 suite. These complexes were used to compare the root mean square fluctuation (RMSF) profiles of peptides in their unbound state versus when complexed with ADAM10. RMSF describes residue-level flexibility, therefore, this comparison provides insight into how the flexibility of individual amino acids changes upon binding, reflecting the stability and tightness of peptide-ADAM10 interaction. Initially, RMSF values of each free peptide were compared to the peptides bound with ADAM10, to assess whether binding resulted in reduced conformational flexibility, serving as a proxy for relative binding strength [Figure 26].

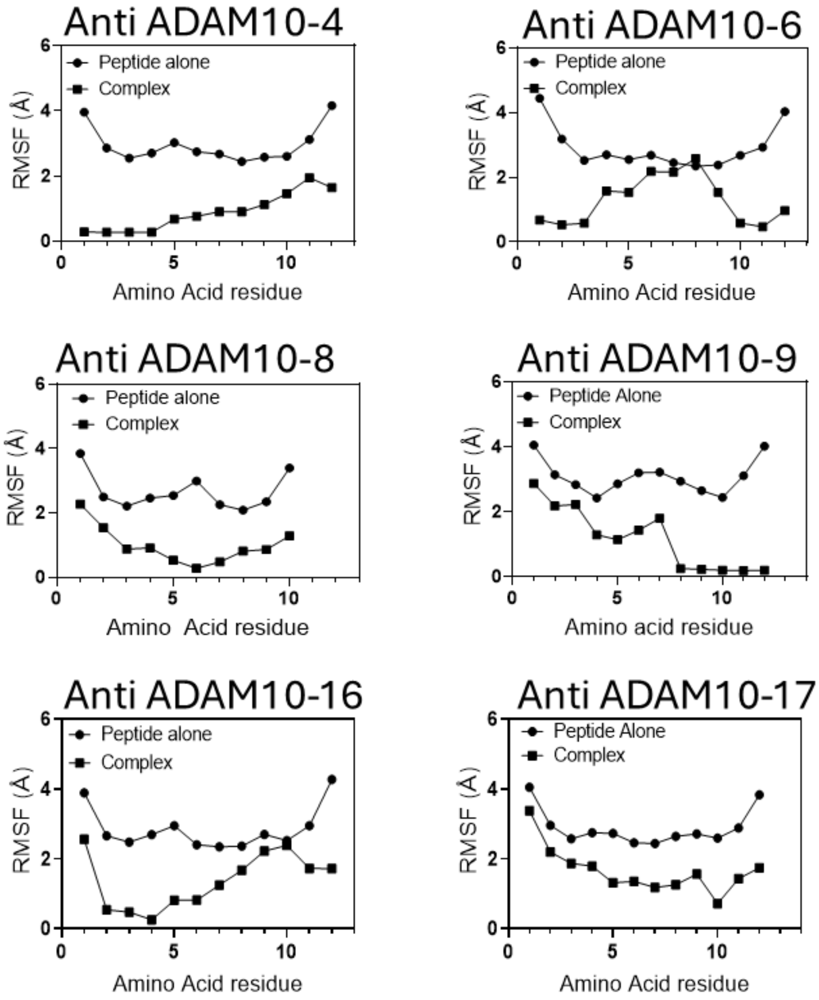

Figure 26) Flexibility analysis of peptides and ADAM10 active site using CABS-Flex 3.0. (A) RMSF (Å) profiles of peptides alone and in complex with ADAM10. A reduction in peptide flexibility upon binding indicates interaction strengh and highlights key residues involved in ADAM10 recognition.

Anti ADAM10-4 and anti ADAM10-8 peptides showed the most pronounced reduction in RMSF upon binding indicating strong peptide stabilization of their structures. Anti ADAM10-16 retained flexibility profile closer to its unbound state from the residue 7 to 12, although a decrease in RMSF was observed between residue 2 and 6. Anti ADAM10-9 exhibited a marked reduction in flexibility starting from residue 8, whereas anti ADAM10-17 showed decreased mobility beginning at residue 4. In contrast, the central residues of anti ADAM10-6 (position 6-8) remained flexible, suggesting limited or partial engagement with ADAM10. Collectively these patterns confirm that different peptides interact with ADAM10 using either their full sequence or specific segments.

To assess whether peptide binding affects the mobility of ADAM10's catalytic region, RMSF values were analyzed for residues 379-394, which include the conserved HEXXH zinc-binding motif (residues 383-387) [Figure 27]. This region was intrinsically rigid due to its predominantly helical secondary structure, whereas the adjacent histidine-containing loop (His393), which is involved in the zinc coordination, displayed increased flexibility. This analysis strategy was specifically employed to evaluate potential peptide interactions with histidine residues involved in zinc coordination, which represents the proposed mechanism by which the small molecule inhibitor GI254023X suppresses ADAM10 activity.

Among the tested peptides, anti ADAM10-8, anti ADAM10-9, anti ADAM10-16 reduced the flexibility of this loop, suggesting possible interference with histidine's involved in zinc coordination and a potential destabilizing effect on ADAM10's catalytic function. However, most peptides did not substantially alter the flexibility of the HEXXH motif. Anti ADAM10-4, anti ADAM10-6 and anti ADAM10-17 showed the least impact on histidine residues participating in zinc coordination.

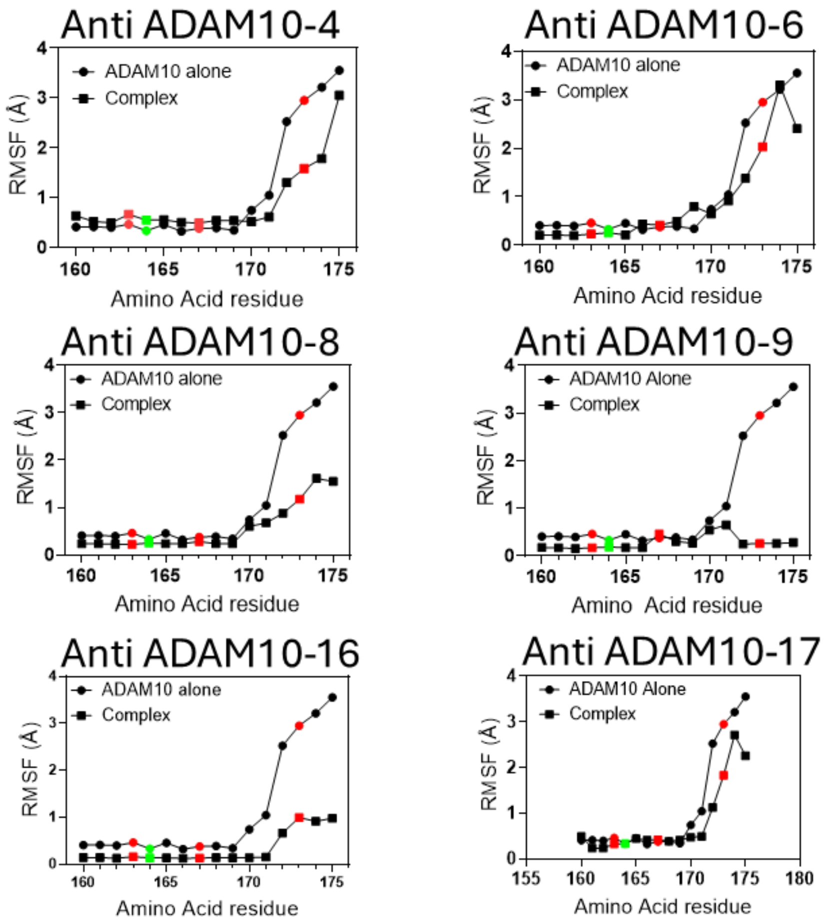

Figure 27) RMSF profiles of ADAM10 active site residues alone and in complex with peptides. Histidines involved in zinc coordination are shown in red, and glutamate responsible for substrate cleavage is in green. The third histidine, located on a flexibile loop, exhibits higher RMSF values. Peptides anti ADAM10-8, anti ADAM10-9 and anti ADAM10-16 notably reduce active site flexibility, suggesting potential inhibitory binding.

To further validate peptide binding to the catalytic region, hydrogen bond geometry between each peptide and the histidine residues involved in zinc coordination was analyzed using Protein-Ligand Interaction Profiler server (PLIP). Donor-acceptor (D-A) distances and angles were evaluated to assess potential hydrogen-bond stability [Figure 28]. In accordance with McDonald *et al.* [218], interactions with D-A angles below 120° were considered weak or transient, whereas those closer to 180° indicate stronger and more linear hydrogen bonds, similarly D-A distances greater than 3.5 were considered non-stable.

Most peptides such as anti ADAM10-4, -6, -8, -9 and -17 did not form stable hydrogen bonds with the histidine’s coordinating the zinc ion due to the length or the angle. In contrast, anti-

ADAM10-16 exhibited favorable hydrogen bond geometry with His393, characterized by short D-A distances and angles compatible with stronger interactions. These findings support the RMSF results obtained with CABS-Flex 3.0, which indicate reduced flexibility of the His393 when anti ADAM10-16 is bound.

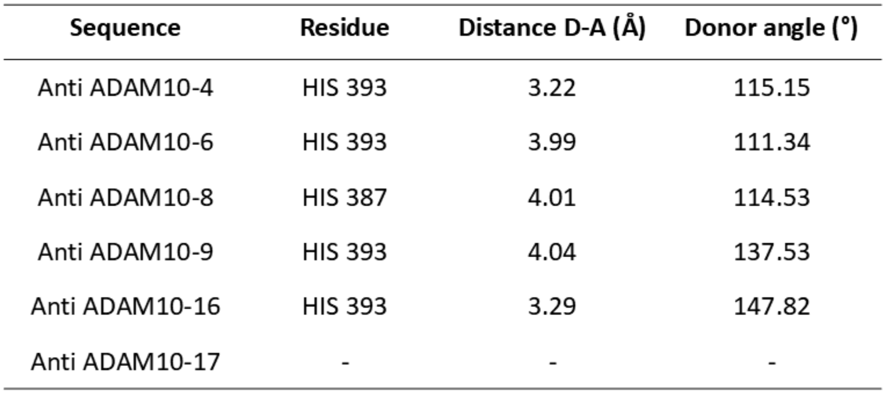

Sequence	Residue	Distance D-A (Å)	Donor angle (°)
Anti ADAM10-4	HIS 393	3.22	115.15
Anti ADAM10-6	HIS 393	3.99	111.34
Anti ADAM10-8	HIS 387	4.01	114.53
Anti ADAM10-9	HIS 393	4.04	137.53
Anti ADAM10-16	HIS 393	3.29	147.82
Anti ADAM10-17	-	-	-

Figure 28) Hydrogen bond geometry between peptides and ADAM10 active site histidine's coordinated with zinc. Peptide-ADAM10 complexes were analyzed using the PLiP webserver to identify hydrogen bond interactions involving histidine residues (His387 and His 393) that coordinate the catalytic zinc ion. For each interaction, the donor-acceptor (D-A) distance and donor angle are reported. Although hydrogen bonds are detected in several complexes, most interactions display suboptimal distances and/or distorted angles, suggesting weak or geometrically unfavorable contacts that are unlikely to effectively disrupt zinc coordination. Among the analyzed peptides, only anti ADAM10-16 shows a hydrogen bond with geometrical parameters compatible with a relevant interaction.

Although not all peptides directly interact with the zinc-coordinated histidine residues, peptide binding in close proximity to the catalytic site could themselves be susceptible to proteolytic cleavage and act as substrate rather than stable inhibitors. Therefore, to identify peptides capable of inhibiting ADAM10 activity while avoiding hydrolysis, we next assessed whether they could still exert inhibitory potential by targeting the substrate-binding pockets. Specifically, we evaluated the ability of the peptides to interact with residues defining the P1, P2, and P3 substrate pockets of ADAM10, which could sterically avoid substrate access even in the absence of direct interactions with the catalytic zinc site. Reduced flexibility of pocket residues was interpreted as evidence of peptide-induced stabilization and possible steric inhibition. Notably, all the predicted peptides displayed interactions near these pockets, supporting their potential to block substrate entry [Figure 29].

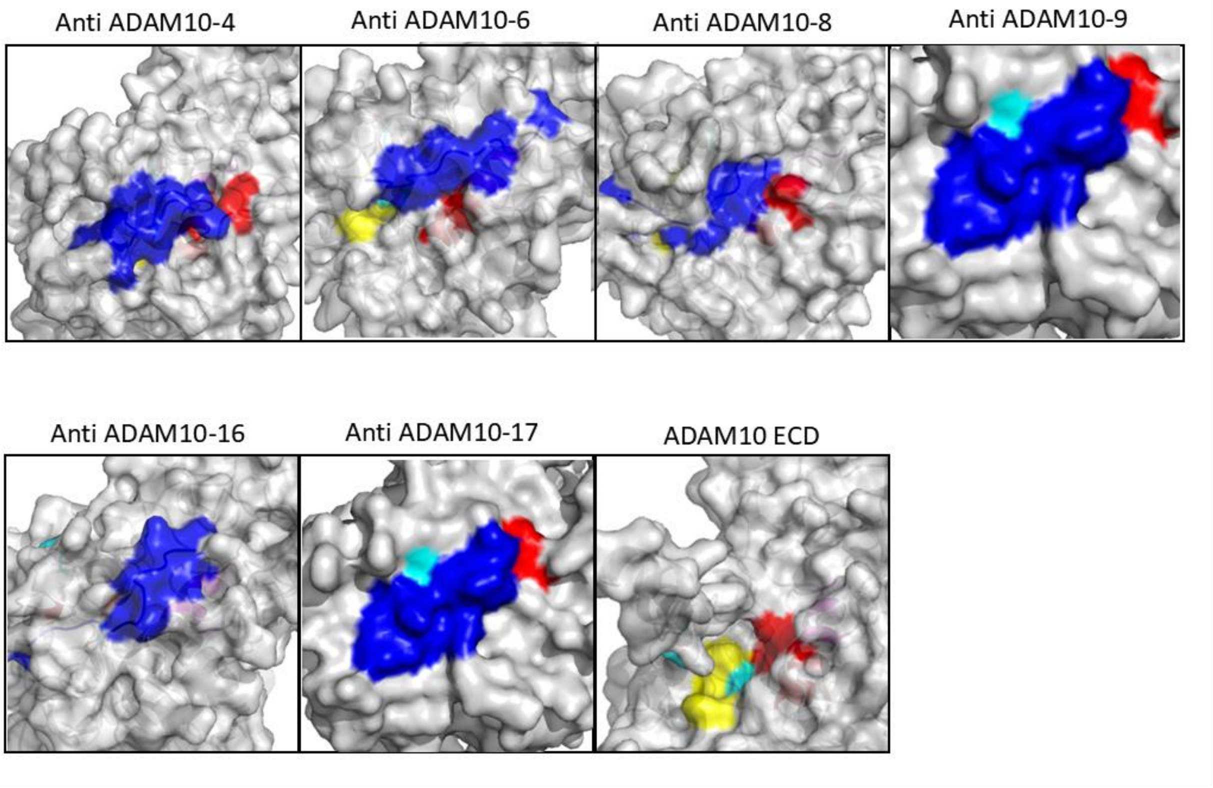

Figure 29) Peptide-ADAM10 complex obtained with CABS-Dock 2.0. the extracellular domain (ECD) of ADAM10 is shown with its three binding pockets highlighted in yellow (first pocket), cyan (second pocket) and magenta (third pocket). The active site is marked in red, while the bound peptides are shown in blue. This figure illustrates the ability of selected peptides to bind and occlude the active site, potentially inhibiting substrate cleavage. Peptides were selected based on their predicted affinity for the active site. Among all tested peptides, anti ADAM10-16 demonstrates the most complete blockage of the active site, suggesting strong inhibitory potential and effective prevention of substrate interaction. The image was realized with Pymol

Moreover, we evaluate the difference in flexibility of the amino acids defining the ADAM10 substrate-binding pockets when bound with the peptides [Figure 30]. Reduced flexibility in these residues reflects peptide-induced stabilization, indicating potential steric interference with substrate access.

For the P1 pocket, anti ADAM10-6 and 16 induced a decrease in flexibility at residues V376, I379, and T380, while anti ADAM10-9 decreased the flexibility of all the P1 residues, highlighting its potential inhibitory relevance. In contrast, anti ADAM10-4 increased flexibility at V376, I379, T380 and I416, suggesting that peptide binding increases local flexibility, which may reduce protein structural stability. Anti ADAM10-8 reduced the flexibility of I379, T380 and I416, while anti ADAM10-17 only decreased the flexibility of T380.

Analysis of the P2 pocket showed no substantial flexibility changes for most peptides. The only exception was anti ADAM10-9, which exhibited increased flexibility compared to the unbound ADAM10 structure.

Within the P3 pocket, anti ADAM10-16 demonstrated a marked reduction flexibility across all residues, supporting its potential role as a steric inhibitor. Anti ADAM10-4 and 7 also reduces flexibility, specifically at L330 and W332. Anti ADAM10-8 and anti ADAM10-17 showed more localized effects, with a decrease in flexibility observed at L301.

Overall, these results indicate that although most peptides exert limited influence on the catalytic core, anti ADAM10-16 demonstrates promising steric inhibition by stabilizing substrate-binding pockets. In contrast, anti ADAM10-4, anti ADAM10-6 and anti ADAM10-9 display mixed behavior decreasing the flexibility of only certain residues. Anti ADAM10-8 and anti ADAM10-17 appear to have minimal impact overall.

Although hydrogen bond formation was observed only for anti ADAM10-16, peptides anti ADAM10 -4, 6, 9 reduced the flexibility of substrate-binding pocket residues. This flexibility reduction may interfere with ADAM10 substrate recognition, suggesting potential inhibitory activity. Therefore, these peptides were selected for *in vitro* inhibition assay.

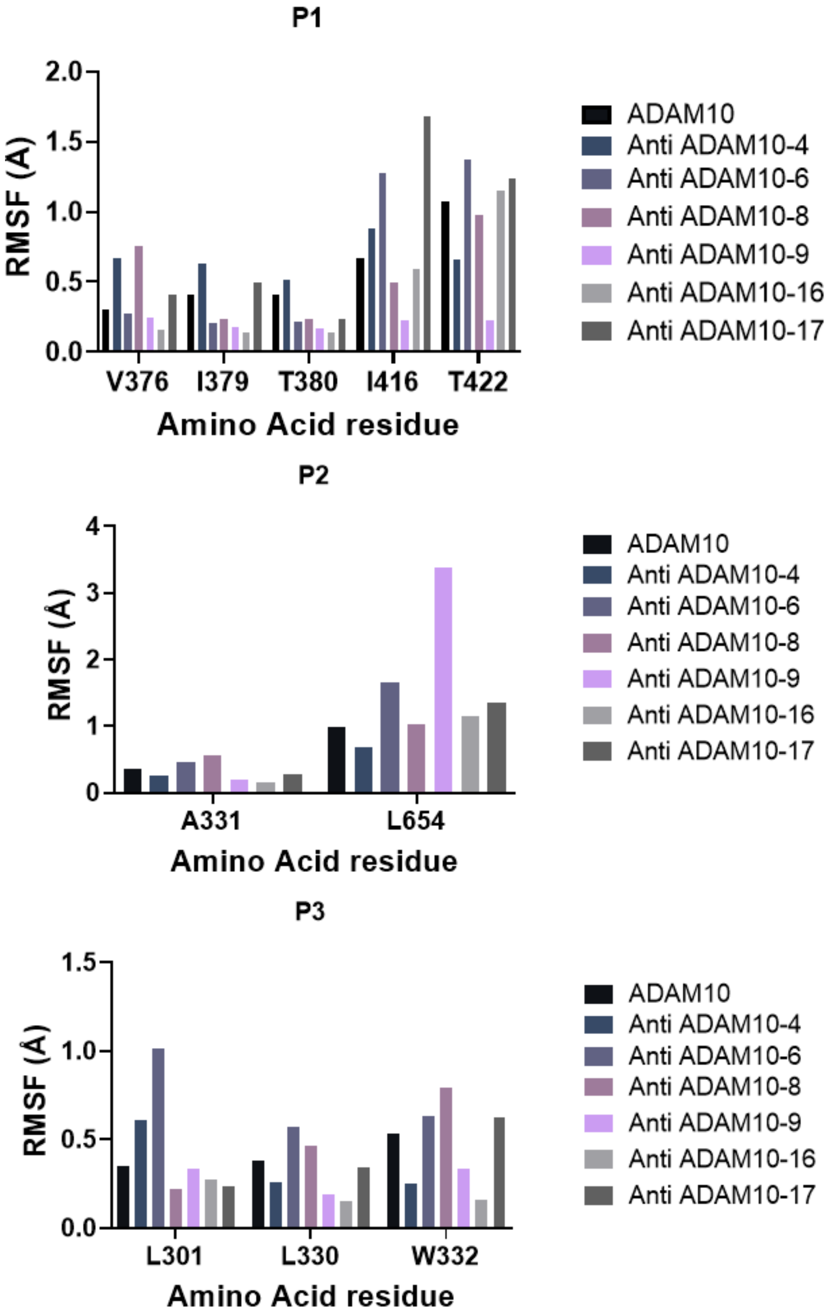

Figure 30) Amino acid flexibility analysis of ADAM10 substrate binding pockets using RMSF. Root Mean Square Fluctuation (RMSF) values were calculated to assess the flexibility of amino acid residues within the three ADAM10 substrate binding pockets (P1, P2 and P3) upon peptide binding. P1 includes residues V376, I379, T380, I416, and T422; P2 includes A331 and L654, P3 includes L301, L330 and W332 [76] *. Each bar graph compares RMSF values for ADAM10 alone (black) and complex with peptides anti-ADAM10-4 (dark blue), anti-ADAM10-6 (dark purple), anti-ADAM10-8 (purple), anti-ADAM10-9 (light purple), anti-ADAM10-16 (light grey) and anti-ADAM10-17 (dark grey). A reduction in RMSF indicates stabilization of the pocket residues upon peptide binding, suggesting effective interaction and potential inhibition. Anti-ADAM10-16 shows the most pronounced reduction in flexibility across all pockets, supporting its role as a strong active site blocker.*

4.2.4 Anti ADAM10-4 partially inhibits recombinant ADAM10 ECD but has no effect on cells

The top four peptides (anti ADAM10-4, -6, -9 and -16) selected through phage display and *in silico* analysis were synthesized by PepMic Co (Suzhou, China) to evaluate their potential to inhibit ADAM10 enzymatic activity. Peptides were incubated at concentrations of 100 µM ,20 µM, 5 µM, 1 µM and 0.5 µM with rhADAM10 (R&D Systems) for 15 min in assay buffer to allow interaction with the enzyme's active site. Subsequently, the fluorogenic substrate Mca-Lys-Pro-Leu-Gly-Leu-Dpa-Ala-Arg-NH_2 (FS-6) was added, and fluorescence emission at 405 nm was monitored as a measure of substrate cleavage.

Among the tested peptides, anti ADAM10-6 did not exhibit any inhibitory effect on rhADAM10 activity (data not shown). Anti ADAM10-9 and anti ADAM10-16 could not be evaluated due to their insolubility in the assay buffer, which led to aggregation and precipitation. Interestingly, anti ADAM10-4 displayed a partial inhibitory effect of rhADAM10 activity [Figure 31]. Increasing the peptide concentration above 1 µM did not further enhance inhibition, as comparable residual enzymatic activity was observed at 20 µM and 100 µM (~63%). These findings indicate that anti ADAM10-4 functions as a partial inhibitor. Given its limited inhibitory capacity, no additional concentrations were tested. Consistent with these functional data, molecular docking analyses indicated that anti ADAM10-4 does not establish stable hydrogen bonds with the histidine required for zinc coordination, while stabilizing some amino acid residues in the binding pocket. This structural effect may reduce, but not completely prevent, substrate cleavage by ADAM10.

To assess whether this partial inhibition translates into a cellular context, we next evaluated the effect of anti ADAM10-4 on ADAM10 expressed in MSTO-211H, H28 mesothelioma cells, as well as in non-cancerous Met5a mesothelial cells. A scratch (wound-healing) assay was performed to monitor cell migration following peptide treatment and to assess potential biological effects on tumor cell behavior [Figure 32]. After generating a uniform scratch, cells were incubated with anti ADAM10-4 and monitored every 2 h using the Incucyte live-cell imaging system. No significant difference in migration was observed between treated and control conditions. This contrasts with the findings reported by Sépult *et al* [66], who described a reduction in cell migration following ADAM10 knockdown or pharmacological inhibition using GI254023X. These results indicate that the partial inhibition of ADAM10 observed *in vitro* with anti ADAM10-4 does not translate into a measurable effect on cell migration at the cell surface level. In conclusion, although a peptide with *in vitro* inhibitory potential against ADAM10 was identified for the first time, anti-ADAM10-4 did not exhibit sufficient efficacy to impair ADAM10 dependent on tumor migration.

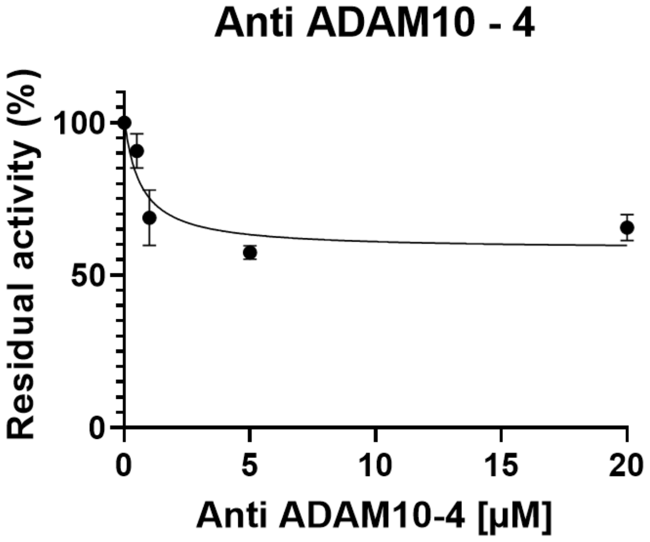

Figure 31) Dose-response curves showing the residual ADAM10 enzymatic activity (%) in the presence of increasing concentrations of the anti ADAM10-4. Each experiment was performed in triplicate (N=3). Data points represent the mean of independent measurements, and error bars indicate the SEM.

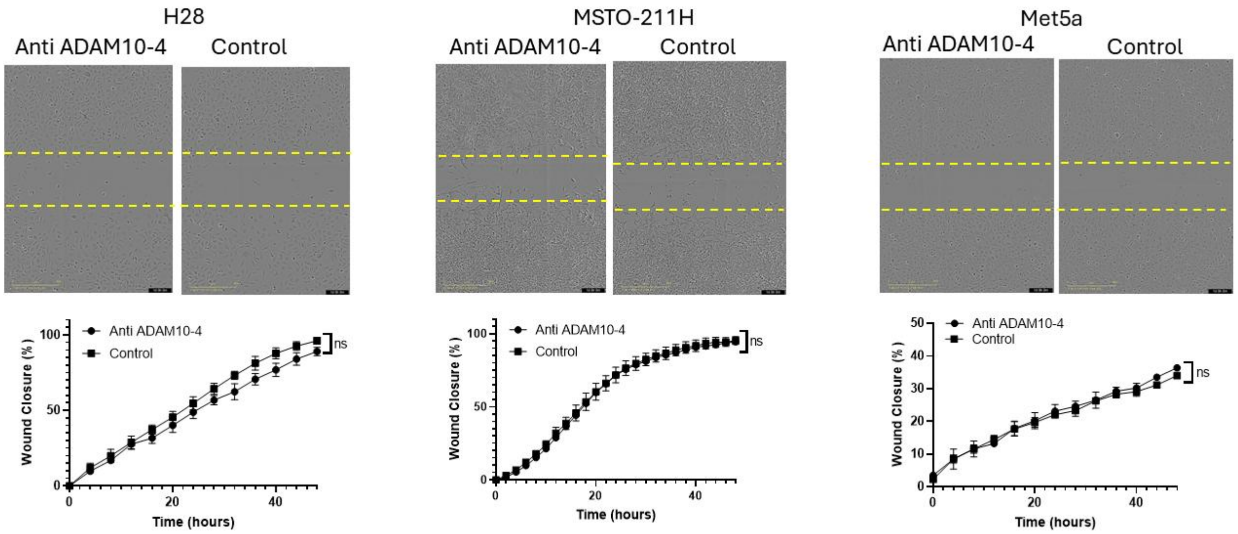

Figure 32) Scratch assay of anti ADAM10-4. H28 (sarcomatoid PM), MSTO-211H (biphasic PM), and Met-5A (non-malignant mesothelial) cells were grown to confluence, scratched, and treated with 10 µM anti ADAM10-4. Wound closure was monitored over time using live-cell imaging. Quantification of wound density revealed no significant difference between treated and control conditions across all cell lines (Two-way ANOVA followed by Sidak multiple comparison test, $^*p<0.05$, ns = not significant).

4.3 A1 VHH, ADAM10 Prodomain and Dual Targeting protein biochemical characterization

4.3.1 A1 VHH production

The A1 VHH selected by Prantner *et al* [206] was expressed as a soluble protein in the periplasm of *E. coli* WK6 cells. The protein was purified by metal ion affinity chromatography (IMAC) via its C-terminal His_6-tag [Figure 33 A], followed by dialysis against 50 mM NaPi (pH 8.0) and filtration through a 0.45 µm cut-off PVDF membrane. SDS-PAGE analysis followed by band intensity quantification using ImageJ software 1.53k, confirmed a purity exceeding 95% of the total lane signal [Figure 33 B].

Starting with 1 L of culture, ~4 mg of protein was obtained. The UV absorbance spectrum [Figure 33 C] indicated the absence of nucleic acid contamination (A280/A260 > 2) and no detectable aggregates (A310 ≤0.02), while the far-UV Circular Dichroism (CD) spectrum exhibited a typical VHH immunoglobulin domain spectrum [214] [Figure 33 D]. Additionally, the intrinsic fluorescence spectrum of A1 VHH showed a maximum at 351 nm [Figure 33 E], indicating that at least one of the two tryptophan residues is exposed.

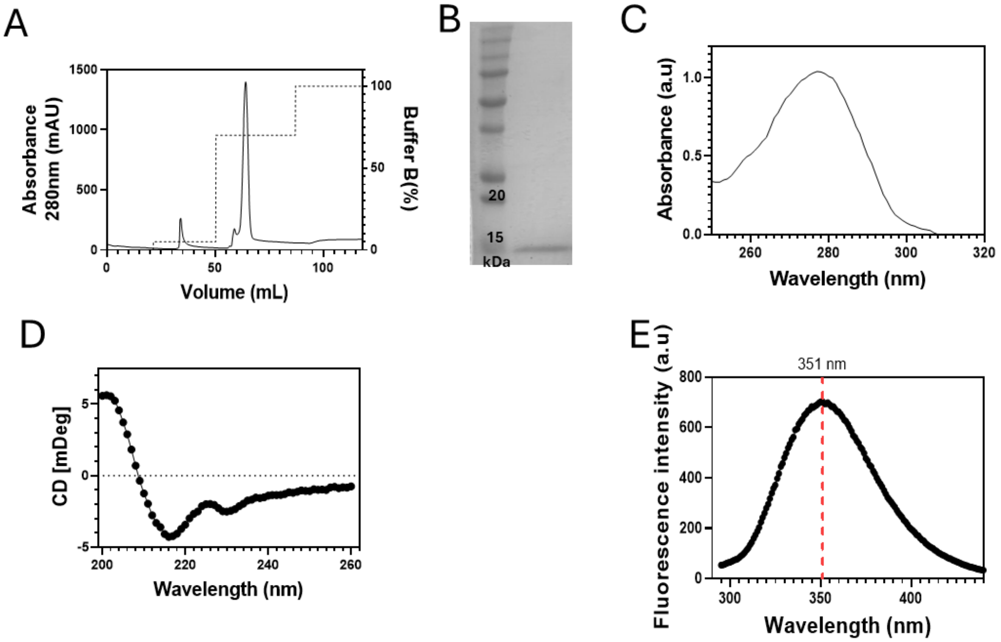

Figure 33) A) The chromatogram of the A1 VHH purified by His Trap 5mL column is shown. Buffer A was 50mM KPi buffer pH8.0 and buffer B was 50mM KPi buffer pH8.0 with 500mM imidazole. B) SDS-PAGE analysis after purification on a 18% SDS-PAGE stained with Coomassie blue. Lane 1 corresponds to the molecular mass marker; Lane 2 corresponds to the A1 VHH. C) UV-vis spectrum of purified A1 VHH. D) Far-UV CD spectrum of A1 VHH in its native form. E) Intrinsic fluorescence spectrum from 290 to 440 nm of the A1 VHH in its native form.

4.3.2 ADAM10 Prodomain production

The C-Ter His6-Tag ADAM10 Prodomain was expressed as a soluble protein in the cytoplasm of *E. coli* BL21 (DE3). It was purified via immobilized metal affinity chromatography [Figure 34 A]. The fractions with purity higher than 95% evaluated by SDS-PAGE band intensity quantification, were pooled together [Figure 34 B]. They were then dialyzed against 100 mM NaCl, 25 mM Tris-HCl-pH 8.0 and filtrated through a 0.45 μm cut-off PVDF membrane. Starting from 1 L of culture, 38 mg of pure ADAM10 Prodomain were obtained. The UV spectrum analysis confirms the protein purity: the 280/260 ratio indicates the absence of

DNA contamination, while the absorbance at 310 nm was close to 0 confirming the absence of aggregates [Figure 34 C]. The Far UV-CD spectrum shows a profile consistent with that shown in Moss *et al* [73], confirming the folded structure. A minimum at 222 nm suggests the presence of α-helixes in the structure, but the non-well-defined bottom at 208 nm is coherent with the presence of a mix between α-helixes and β-strands in the structure [Figure 34 D]. The fluorescence spectrum obtained by exciting the protein at 280 nm and observing the emission from 295 nm up to 440 nm, shows only a peak centered at 305 nm [Figure 34 E]. This corresponds to the maximum of emission of the twelve tyrosine residues, while there is no tryptophan in the sequence of the prodomain. Altogether, these data confirm that recombinant ADAM10 Prodomain produced in *E. coli*, is pure and folded.

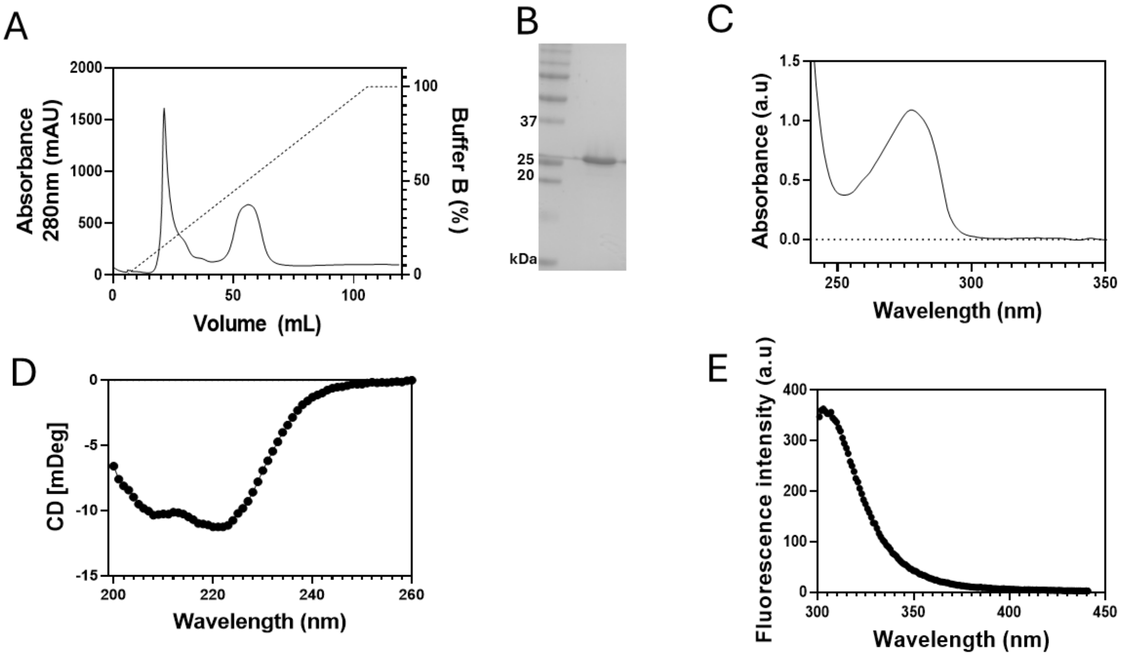

Figure 34) A) The chromatogram of ADAM10 Prodomain purified using a His Trap 5mL column is shown. Buffer A was 50mM phosphate buffer pH8.0, 300mM NaCl, 10mM imidazole and buffer B was phosphate buffer pH8.0 with 300mM NaCl and 500mM imidazole. B) SDS-PAGE analysis after purification on a 18% SDS-PAGE stained with Coomassie blue. Lane 1 corresponds to the molecular mass marker; Lane 2 corresponds to the ADAM10 Prodomain. C) UV-vis spectrum of purified ADAM10 Prodomain. D) Far UV-CD spectrum of ADAM10 Prodomain in its native form. E) Intrinsic fluorescence spectrum the ADAM10 Prodomain in its native form.

4.3.3 The Dual Targeting protein preserves the structure and functional integrity of its two domains

The Dual Targeting protein was expressed as a soluble protein in *E. coli* BL21 (DE3). The recombinant protein was purified by metal ion affinity chromatography [Figure 35 A] followed by dialysis against to remove imidazole and filtration through a 0.45 μm cut-off PVDF membrane. Protein purity was analyzed via SDS-PAGE, only fractions with a purity greater than 95% were collected [Figure 35 B]. The UV spectrum showed the absence of nucleic acid contamination (280/260 >2), and no aggregates were detectable (A310 ≤ 0.02) [Figure 35 C]. Starting from 1 L of culture, 0.5 mg of protein was obtained. The far-UV CD spectrum revealed a profile consistent with a folded protein containing a mix of α-helix and β-sheets. Notably, the minimum of 208 nm and 222 nm, typically associated with the α-helical content of the ADAM10 Prodomain, were altered due to the contribution of the A1 VHH [Figure 35 D]. Due to this contribution, the Dual Targeting protein far-UV CD profile presents a shift with a bottom at 218 nm, due to the presence of both A1 VHH and ADAM10 Prodomain profiles. Interestingly, the computed CD spectrum of the individual domains (A1 VHH and ADAM10 Prodomain in equimolar amount) closely resembled the experimental far-UV CD spectrum of the Dual Targeting protein [Figure 35 E]. This observation suggests that fusion of ADAM10 prodomain to the A1 VHH does not alter the overall secondary structure of the individual domains. The intrinsic fluorescence emission spectrum of the Dual Targeting Protein exhibits a maximum at 351 nm, consistent with the presence of exposed tryptophan in the tertiary structure of the A1 VHH of the Dual Targeting protein [Figure 35 F]. Interestingly, a smaller emission peak is observed around 305 nm, attributable to the contribution of the ADAM10 Prodomain, which contains 12 tyrosine, but no tryptophan as already mentioned. Due to the relatively low contribution of the ADAM10 Prodomain to the fluorescence signal, the overall emission profile of the Dual Targeting protein is largely dominated by the VHH component. Accordingly, the theoretical fluorescence spectrum generated by summing the individual emission profiles of the ADAM10 Prodomain and the A1 VHH closely matches the experimental Dual Targeting protein spectrum [Figure 35 G]. This concordance indicates that, within the fusion construct, both the ADAM10 prodomain and the A1 VHH retain their native tertiary structures without significant mutual perturbation.

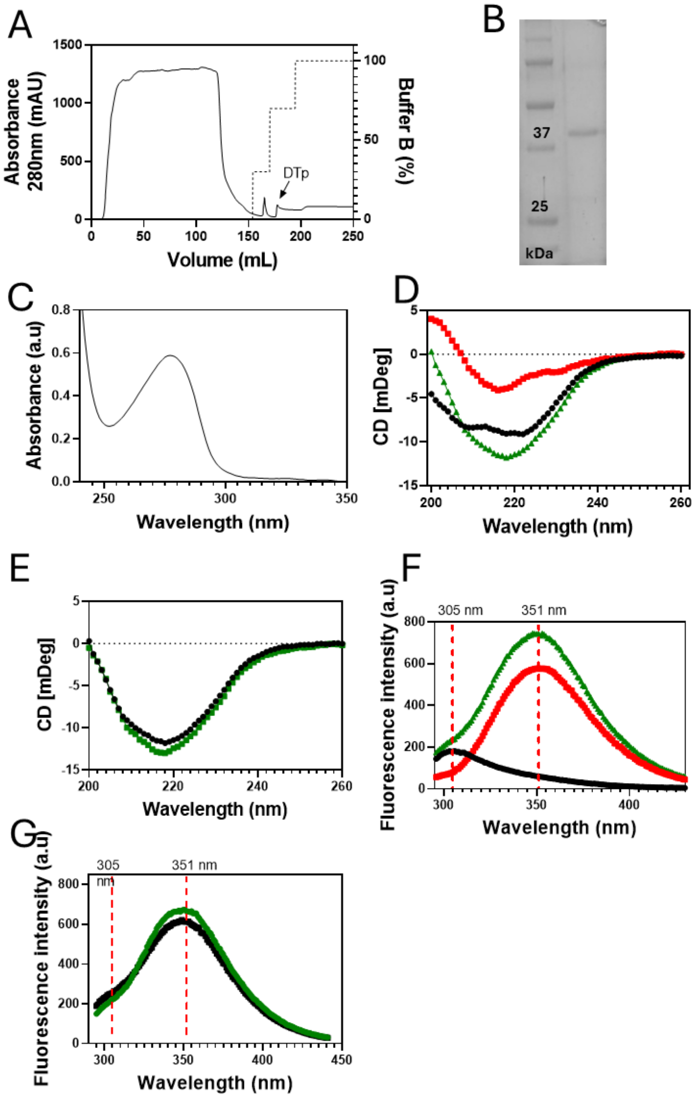

Figure 35) A) The chromatogram of the Dual Targeting protein purified via a His Trap 5mL column is shown. Buffer A was 50mM KPi buffer pH8.0 and buffer B was 50mM KPi buffer pH8.0 with 500mM imidazole. B) SDS-PAGE analysis after purification. Lane 1 corresponds to the molecular mass marker; Lane 2 corresponds to the purified Dual Targeting protein. C) UV-vis spectrum of the purified Dual Targeting protein. D) Far-UV CD spectrum of the Dual Targeting protein (green), A1 VHH (red), and ADAM10 Prodomain (black). E) Far UV-CD spectrum of the Dual Targeting protein (green) and its computed spectrum (black) obtained by summing the spectrum of each protein. F) Intrinsic fluorescence emission spectrum of Dual Targeting protein (green), anti VHH 1 (red) and ADAM10 Prodomain (black). The intrinsic fluorescence emission spectrum of the Dual Protein displays a maximum centered at 351 nm, consistent with the presence of tryptophan exposed. G) Intrinsic fluorescence emission spectrum of the Dual Targeting protein (green) and its computed spectrum (black) obtained by summing the spectrum of each protein.

4.3.4 Thermal stability Dual Targeting protein

To evaluate the contribution of the ADAM10 Prodomain and the A1 VHH to the thermal stability of the Dual Targeting protein, heat-induced denaturation was monitored by far-UV CD and intrinsic fluorescence emission spectroscopy. Each recombinant protein was analyzed in both its native form and heat-denatured states.

For CD measurements, spectrum was recorded between 185 nm and 260 nm at 25°C and 97°C. Wavelengths used for thermal unfolding analysis were selected to maximize the signal difference between the native and denatured states while ensuring reliable measurements by maintaining the high-tension (HT) voltage below 350 V (data not shown), as higher HT values are associated with increased noise and reduced signal reliability. Based on this combined criteria, 208 nm was selected for A1 VHH, 222 nm for the ADAM10 Prodomain and 218 nm for the Dual Targeting protein [Figure 36 A].

Intrinsic fluorescence emission spectrums were collected from 290 nm to 440 nm at 25°C and 90°C. The maximal difference between folded and unfolded states was observed at 351 nm for A1 VHH and the Dual Targeting protein, while 305 nm for ADAM10 Prodomain [Figure 36 B].

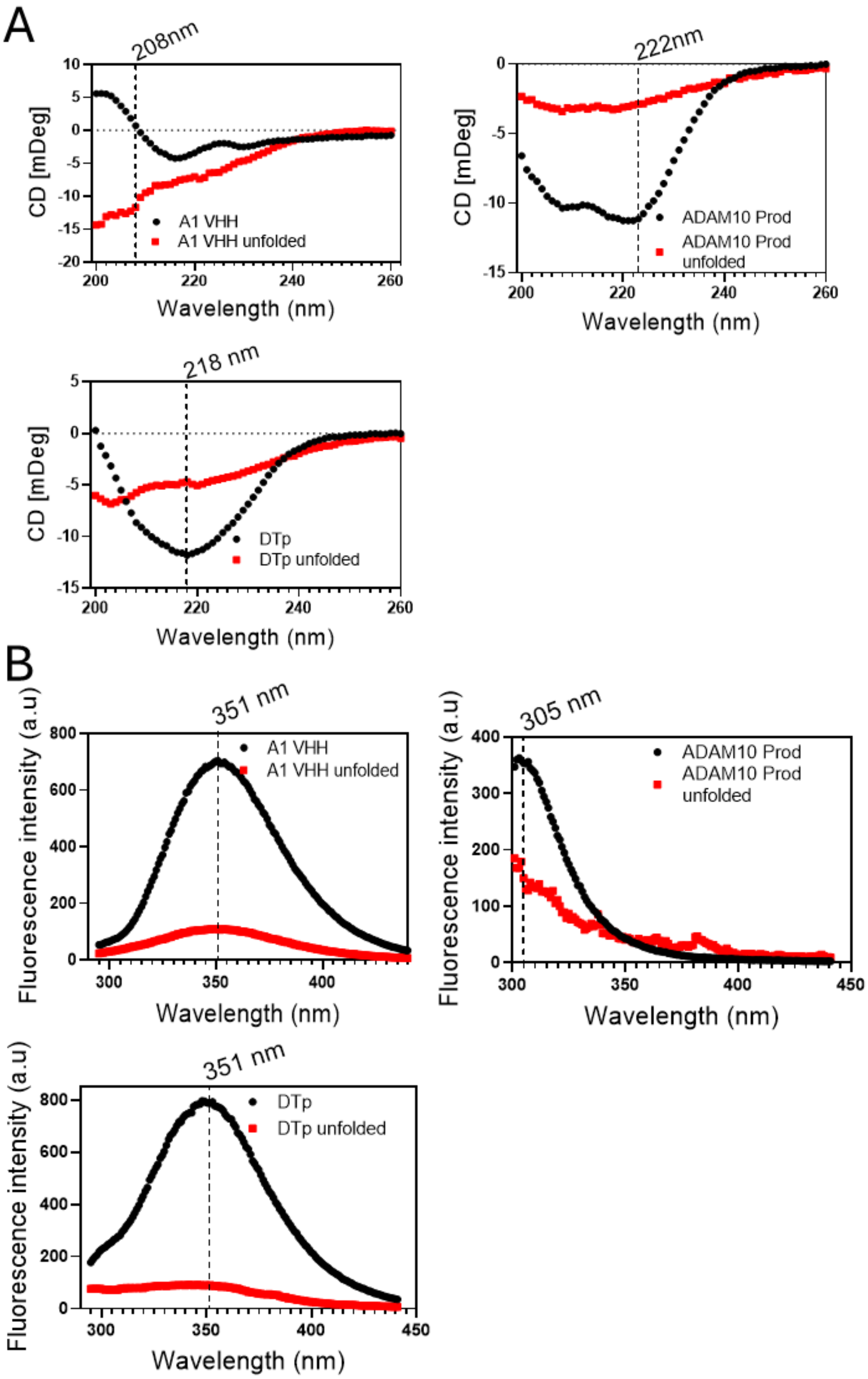

Figure 36 A) Circular Dichroism spectrum from 185 and 260nm of A1 VHH, ADAM10 Prodomain or Dual Targeting protein in their native form (black) and unfolded form (red). The largest signal difference between the spectrum of the native and unfolded state is 208 nm for the A1 VHH, 222 nm for the ADAM10 prodomain and 218 nm for the Dual Targeting protein (DTp) B) Intrinsic fluorescence spectrum of A1 VHH, ADAM10 Prodomain or Dual Targeting protein in their native form (black) and unfolded form (red). The largest difference between folded and unfolded states occurred at 351 nm for A1 VHH and the Dual Targeting protein, and 305 nm for ADAM10 Prodomain.

Thermal unfolding curves were recorded during upon a linear temperature increase by monitoring the changes is CD and fluorescence signals at the wavelength selected for each protein [Figure 37].

CD thermal unfolding analysis revealed that A1 VHH unfolds at high temperature, indicative of high thermal stability. The unfolding transition exhibits a sigmoidal shape characteristic of a two-state unfolding process. Such a process is consistent with previously reported VHH unfolding profiles [214]. In contrast, the ADAM10 Prodomain exhibited a transition at a lower temperature, indicating reduced thermal stability relative to A1 VHH. Aggregation was clearly visible upon the thermal denaturation of the ADAM10 Prodomain.

The Dual Targeting protein displayed a reduced thermal stability comparable to that of the isolated ADAM10 Prodomain. As observed by the ADAM10 Prodomain alone, thermal denaturation of the Dual Targeting protein was accompanied by visible aggregation.

Intrinsic fluorescence data further supports the CD analysis [Figure 37]. For A1 VHH, the fluorescence intensity decreased linearly with increasing temperature during the pre-transition region, reflecting the intrinsic temperature dependence of tryptophan fluorescence properties within the VHH native state. The unfolding transition occurred at higher temperatures and coincided with the unfolding event detected by CD.

For the ADAM10 Prodomain, the unfolding transition occurred in the same temperature range as that observed with CD. Similarly, for the Dual Targeting protein the unfolding transition coincided with that monitored by CD. However, thermal denaturation of both the ADAM10 prodomain and the Dual Targeting protein led to aggregation, resulting in increased light scattering and preventing accurate fitting of the data to a two-state unfolding model.

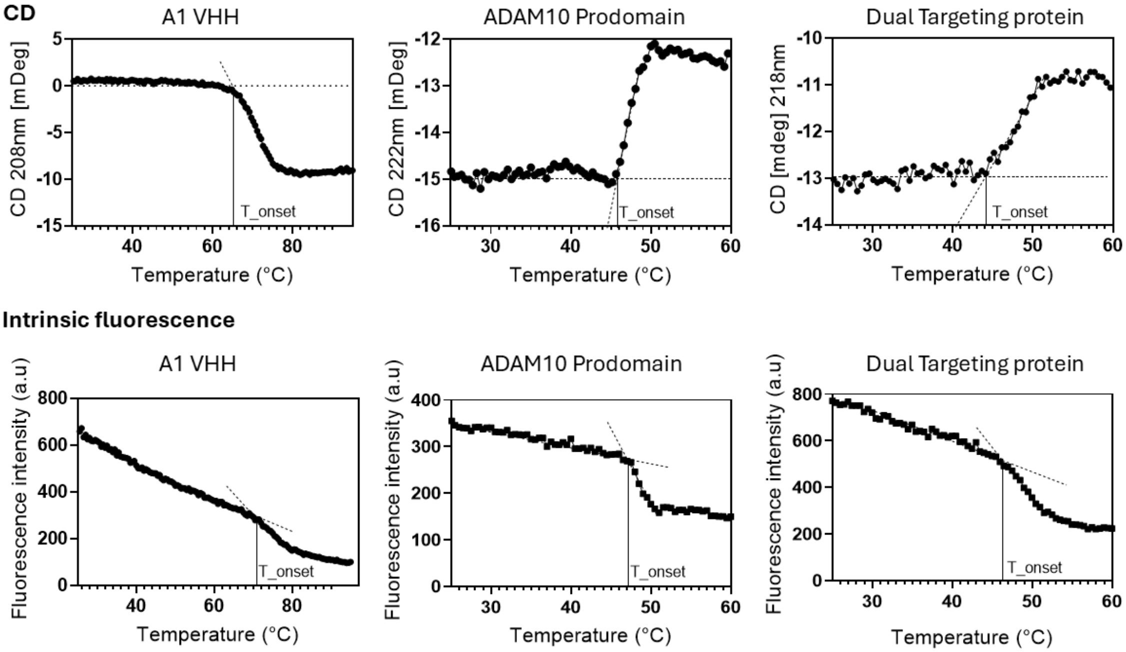

Figure 37) Thermal unfolding of A1 VHH, ADAM10 Prodomain, and the Dual Targeting protein monitored by far UV-CD and intrinsic fluorescence. CD measurements (top panels) were used to monitor changes in the secondary structure upon heating, while intrinsic fluorescence (bottom panels) was used to monitor changes in the environment of tryptophan and tyrosine residues and thus to monitor changes in the tertiary structure. Temperature-dependent CD measurements were recorded at wavelengths selected to maximize the difference between the native and denatured states while maintaining acceptable HT values: 208 nm (A1 VHH), 222 nm (ADAM10 prodomain), and 218 nm (Dual Targeting protein). Intrinsic fluorescence emission was recorded at 305 nm for the ADAM10 Prodomain and at 351 nm for A1 VHH and Dual Targeting protein.. A1 VHH displays the highest thermal stability, whereas the ADAM10 prodomain and Dual Targeting protein unfold at lower temperatures. For each recombinant protein, the T_onset was determined from both CD and fluorescence data using a tangent-based analysis of the pre-transition baselines and transition region. T_onset corresponds to the temperature at which the first detectable deviation from the pre-transition occurs, reflecting the beginning of structural destabilization.

Despite aggregation, the onset temperature of denaturation (T_onset) was determined for each recombinant protein using both CD and fluorescence measurements [Figure 37]. T_onset values were estimated by extrapolating tangents to the pre-transition baseline and the transition region. The T_onset of the Dual Targeting protein was 45.4±0.3°C, closely matching that of the ADAM10 Prodomain of 45.8±0.2°C, and significantly lower than that of the A1 VHH of 62.7±0.4°C [Figure 38 A, B]. Taken together, these data demonstrate that fusion to the A1 VHH does not destabilize ADAM10 Prodomain, resulting in a Dual Targeting protein with a T_onset comparable to that of the prodomain alone.

A

T_onset	Circular Dichroism	Fluorescence
A1 VHH	62.70±0.43°C	64.45±0.45°C
ADAM10 prodomain	45.83±0.24°C	46.97±0.05°C
Dual Targeting Protein	45.37±0.26°C	47.37±0.83°C

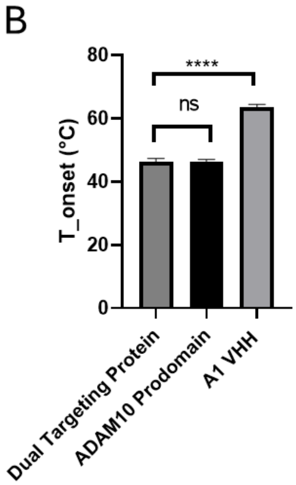

*Figure 38) Summary of T_onset values of A1 VHH, ADAM10 Prodomain, and Dual Targeting protein. A) A1 VHH displays a markedly higher T_onset compared with the ADAM10 Prodomain and the Dual Targeting protein, indicating greater thermal stability. In contrast, the Dual Targeting protein exhibits a T_onset nearly identical to that of the ADAM10 Prodomain, demonstrating that fusion to the VHH does not destabilize the prodomain within the Dual Targeting protein. B) Comparison of average T_onset values. The stability of the Dual Targeting protein does not differ significantly from that of the ADAM10 prodomain, whereas both are significantly less thermally stable than the A1 VHH. Data are shown as mean ± SEM. Statistical analysis was performed using one-way ANOVA followed by Dunnett's multiple comparison test, using the Dual Targeting protein as the reference group (**** p<0.0001). These results support the conclusion that the VHH does not destabilize the ADAM10 Prodomain in the Dual Targeting protein.*

Due to the aggregation during unfolding of the ADAM10 Prodomain and Dual Targeting protein, normalization of unfolding transitions was only feasible for A1 VHH. The absence of aggregation allowed the thermal unfolding curves obtained by far-UV CD and intrinsic fluorescence spectroscopy to be normalized and directly compared. The normalized curves were superimposable, supporting a two-state unfolding mechanism (native ⇌ unfolded). Temperature-dependent CD analysis yielded a melting temperature (Tm) of 69.9±0.9°C [Figure 39].

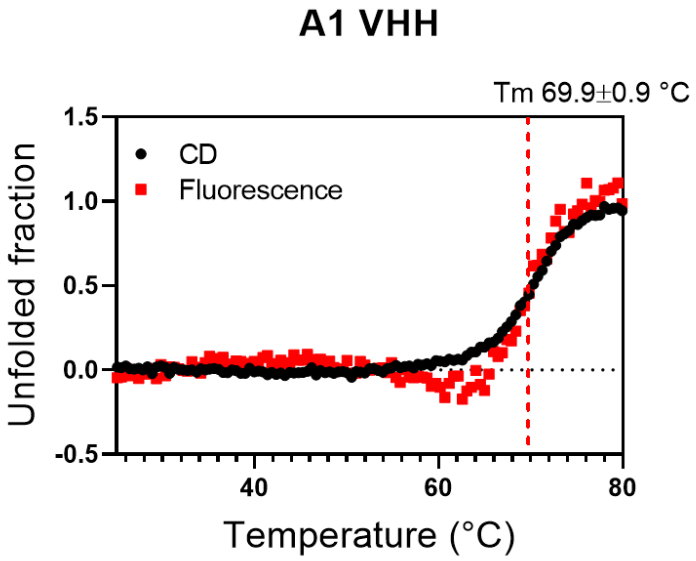

Figure 39) Heat-induced unfolding of A1 VHH monitored by Far-UV CD (black) and intrinsic fluorescence (red). The normalized unfolding profiles obtained by CD and fluorescence are superimposable, indicating that changes in the structure detected by CD and fluorescence changes occur over the same temperature range. This behavior is consistent with a two-states unfolding process. The red dashed line indicates the melting temperature (Tm) of A1 VHH of 69.9±0.9°C.

4.3.5 Dual Targeting protein via its ADAM10 prodomain inhibits ADAM10 *in vitro* and prevents the N-Cadherin cleavage in cells

The inhibition of ADAM10 by its prodomain (C173S 23-213 C-terminal His Tag) has been previously described by Moss *et al* [73], which confirms to be an ADAM10 inhibitor with an apparent inhibition constant (Ki) of 36±9 nM. The FS-6 substrate, which is based on the cleaved sequence of TNF-α added with a quencher (fluorescent 7-methoxycoumarin group) and a fluorescent group (2, 4-dinitrophenyl group) was used to follow the residual activity of ADAM10 in the absence and the presence of different concentrations of ADAM10 Prodomain or Dual Targeting protein [Figure 40 A]. The concentration of rhADAM10 was 1 nM and the concentration in substrate was 15 μM. The experiment was repeated with three different lots of production of ADAM10 Prodomain and Dual Targeting protein. The average IC_{50} was 0.24±0.03 μM and 0.32±0.04 μM [Figure 40 B] for respectively ADAM10 Prodomain and the Dual Protein. No statistical differences between ADAM10 Prodomain and Dual Targeting protein were observed [Figure 40 C], confirming that the capacity of ADAM10 Prodomain in the Dual Targeting protein to inhibit the ADAM10 catalytic activity is not altered by the fusion with the A1 VHH.

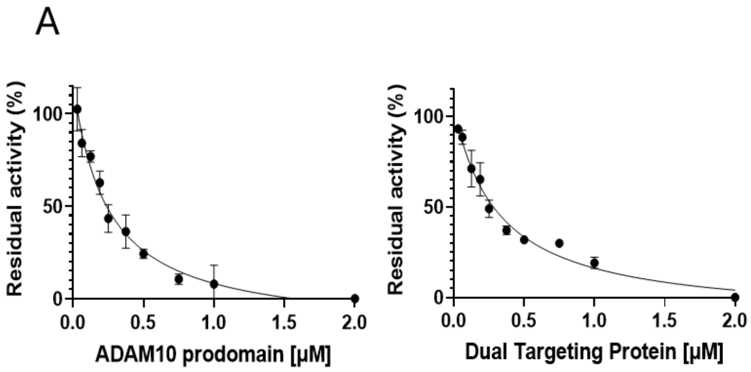

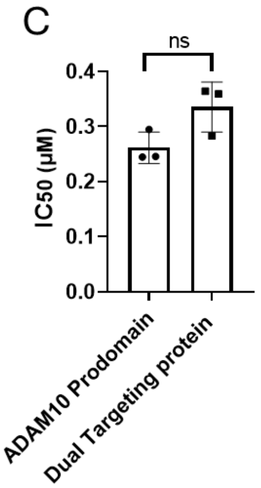

B

	ADAM10 Prodomain	Dual targeting Protein
IC50	0.24±0.03 µM	0.32±0.04 µM

*Figure 40 A) Dose-response curves showing the residual ADAM10 enzymatic activity (%) in the presence of increasing concentrations of the ADAM10 prodomain or the Dual Targeting protein. Each experiment was performed in triplicate (N=3). Data points represent the mean of independent measurements, and error bars indicate the SEM. B) IC$_{50}$ values of the ADAM10 Prodomain and Dual Targeting protein, expressed in µM as mean ± SEM. C) Comparison of the IC$_{50}$ values between ADAM10 Prodomain and the Dual Targeting protein. Results are presented as mean ± SEM. Ststistical significance was evaluated with the unpaired student's t-test: * P<0.05.*

To evaluate the inhibitory capacity of the ADAM10 Prodomain and the Dual Targeting protein in a cellular context, ADAM10 expressing human mesothelioma cell lines (H28 and MSTO-211H) as well as non-malignant human mesothelial Met5a cells were treated with the ADAM10 Prodomain and Dual Targeting protein. The impact of these treatments on the N-cadherin cleavage, a known substrate of ADAM10 was subsequently assessed. As reported by Sépult *et al* [66], genetic knockdown of ADAM10 or pharmacological inhibition of ADAM10 using GI254023X reduces the N-cadherin cleavage. This limits the release of the soluble NTF and consequently its binding to the Fibroblast Growth Factor Receptor (FGFR) associated with cancer cell migration [66] [Figure 41].

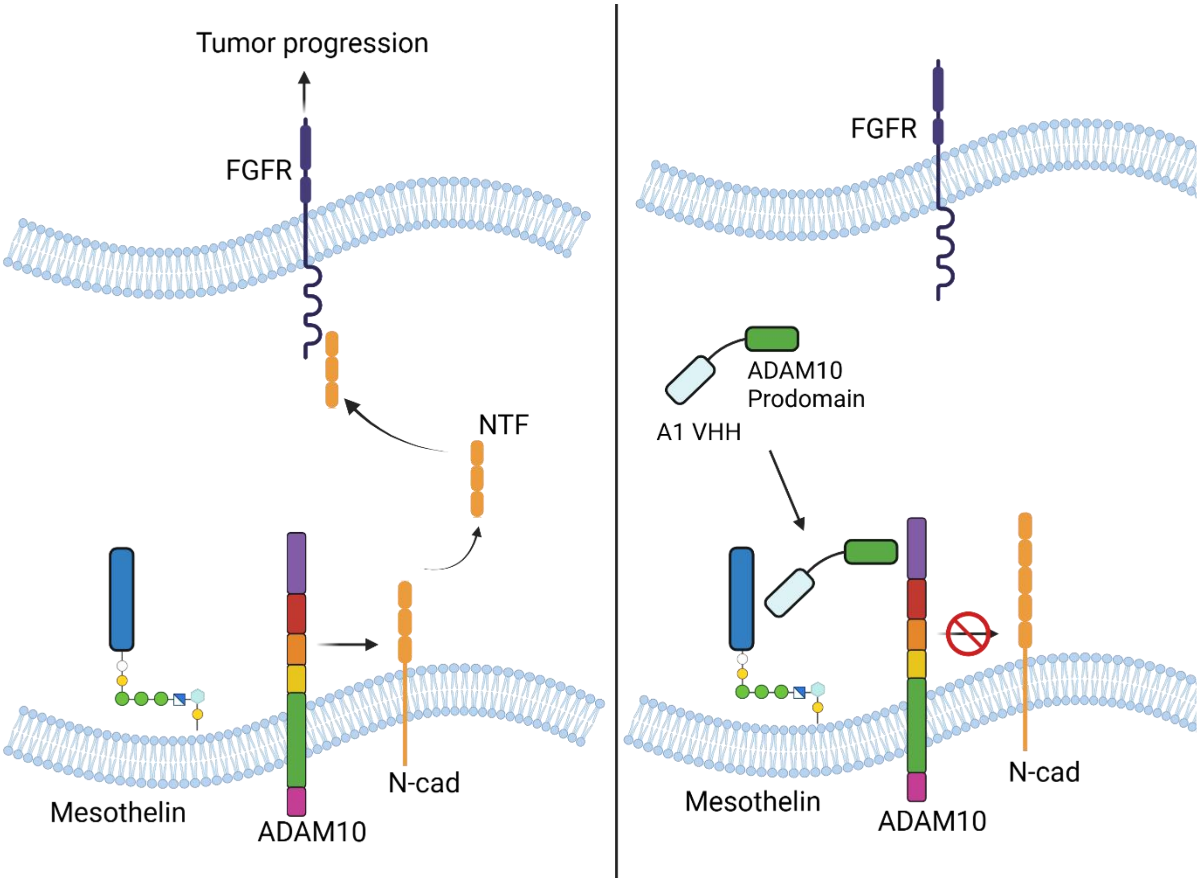

Figure 41) ADAM10-mediated cleavage of N-cadherin and its impact on FGFR signaling in mesothelioma. Overexpression of ADAM10 at the surface of PM cells promotes proteolytic cleavage of the N-cadherin, resulting in the release of a soluble N-terminal fragment (NTF, ~95 kDa). The NTF can interact with fibroblast growth factor receptors (FGFRs), stabilizing it and contributing to sustained pro-tumorigenic signaling pathways involved in cell migration and tumor progression. Pharmacological inhibition of ADAM10 using the Dual Targeting protein prevents N-cadherin cleavage, thereby limiting NTF release and attenuating FGFR-dependent tumor-promoting signaling [66]*. This image was realized with BioRender.*

Western blot analysis confirmed that ADAM10 is overexpressed on the surface of the two PM cancer cell lines (H28 and MSTO-211H) compared to the non-cancerous Met5a cell lines [Figure 42 A]. To assess whether the ADAM10 Prodomain and the Dual Targeting protein could inhibit ADAM10 activity, all the three cell lines were treated with the recombinant proteins. To evaluate N-cadherin shedding, conditioned media were concentrated using 50 kDa Amicom filters, allowing the enrichment of the 95 kDa N-terminal fragment (NTF) while minimizing interference from low-molecular-weight proteins. Concentrated media together with corresponding cell lysates were analyzed by western blot. Across all the PM cell lines, the treatment with either the ADAM10 Prodomain or the Dual Targeting protein resulted in a clear reduction of N-cadherin cleavage. This latter is accompanied by a marked decrease in the NTF detected in the conditioned medium compared to untreated controls [Figure 42 B]. A significant reduction of N-cadherin cleavage was further observed in Met5a cells treated with ADAM10 Prodomain or Dual Targeting protein. These data confirm the ability of the Dual Targeting protein to inhibit ADAM10 activity through its ADAM10 Prodomain and are consistent with previously reported findings by Sèpult *et al* [66].

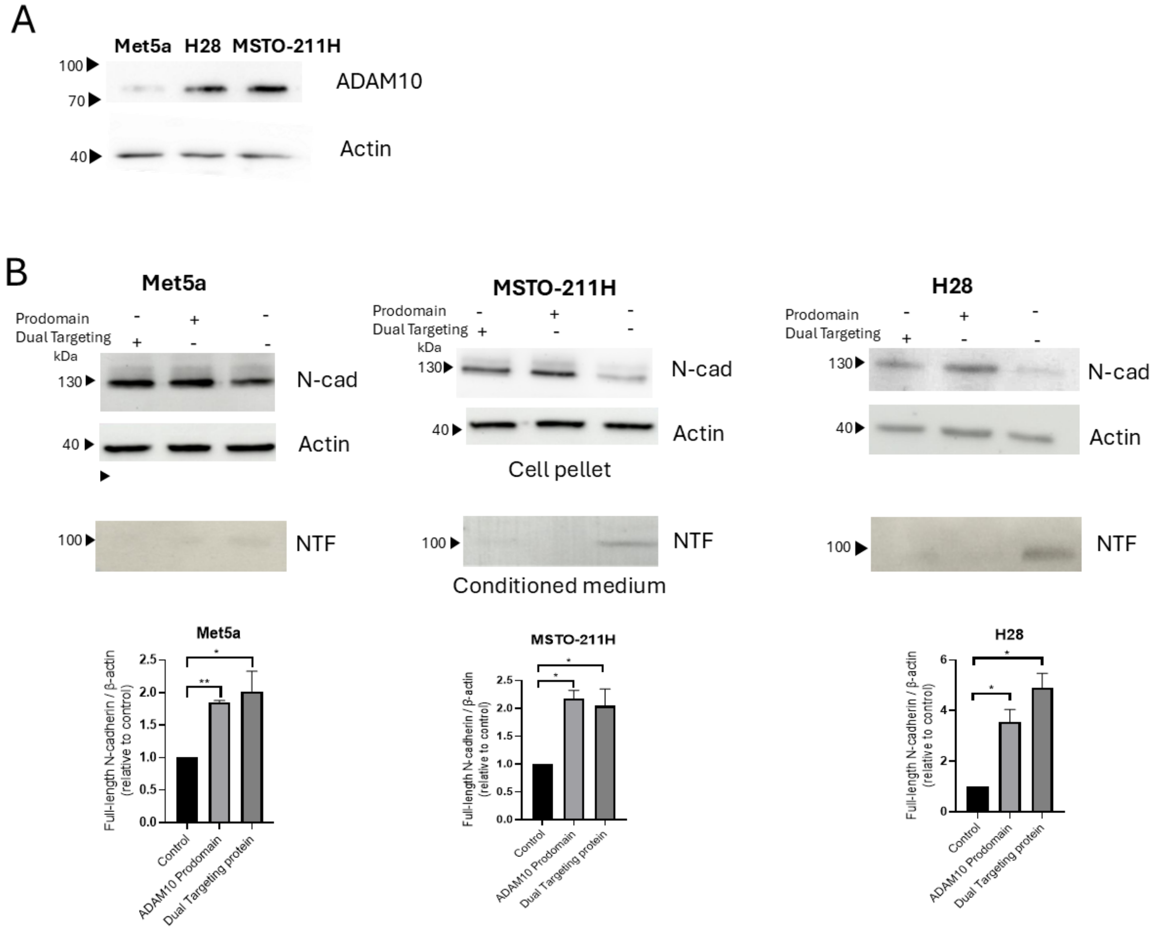

*Figure 42) ADAM10 expression and N-cadherin shedding in mesothelial and mesothelioma cell lines. A) Western blot analysis of ADAM10 expression in Met5a, MSTO-211 and H28 cells. B) Western blot analysis of full-length N-cadherin (~130kDa) in cell pellet fractions (lysates) and soluble NTF (~95kDa) in conditioned media, detected with an anti N-cadherin antibody. Actin was used as a loading control for cell pellet fractions. Increased NTF in conditioned media indicates ADAM10 mediated shedding. Treatment with the Dual Targeting protein or ADAM10 Prodomain reduced N-cadherin cleavage, as shown by increased full-length N-cadherin and decreased soluble NTF. Full length N-Cadherin band intensities were normalized to actin and expressed relative to control. Data are shown as mean ± SEM. For each cell line, statistical analysis was performed using the one-way ANOVA with Dunnett's multiple comparison test versus control (*p <0.05, ** p<0.01).*

4.3.6 The Dual Targeting protein recognizes, *in vitro,* the recombinant human mMSLN via its A1 VHH domain

The binding of the Dual Targeting protein and A1 VHH to recombinant human mMSLN (rhmMSLN) was assessed using western blot analysis and native PAGE. Western blot analysis of rhmMSLN incubated with either A1 VHH or Dual Targeting protein and detected with a rabbit anti VHH-HRP antibody confirmed the protein's ability to bind human mature mesothelin [Figure 43 A]. The binding capacity of A1 VHH was further confirmed by native PAGE. A single band corresponding to the A1 VHH and rhmMSLN was observed, consistent with their presence as monomers. Upon incubation at a 1:1 molar ratio, a mobility shift relative to the unbound proteins was detected, indicating complex formation. The absence of additional bands suggests the formation of a predominant complex, consistent with a defined binding interaction between A1 VHH and rhmMSLN [Figure 43]. The native PAGE for the Dual Targeting protein incubated with mature mesothelin in a 1:1 molar ratio shows a migration shift compared to the Dual Targeting protein or rhmMSLN alone. This data confirms the capacity of the Dual Targeting protein to bind the human mesothelin [Figure 43C].

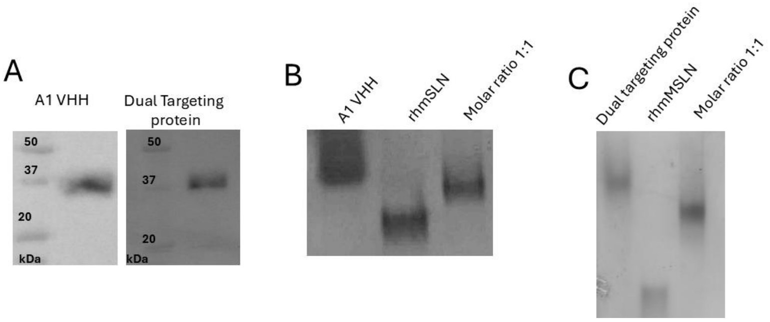

Figure 43) Recognition of the rhmMSLN by A1 VHH and Dual Targeting protein. A) The ability of A1 VHH and Dual Targeting protein to recognize rhmMSLN was assessed by western blot. Following protein transfer, membranes were incubated with either A1 VHH or the Dual Targeting protein. Bound VHH-based constructs were detected using an anti VHH antibody conjugated by HRP. Lane 1 corresponds to the molecular mass marker, lane 2 rhmMSLN detected at approximately 37 kDa using A1 VHH or Dual Targeting protein. B) Native PAGE of A1 VHH and human mature mesothelin. Lane 1 and Lane 2 correspond respectively to the migration of A1 VHH and human mature mesothelin. Lane 3 shows the migration pattern of an equimolar amount of A1 VHH and rhmMSLN, indicating complex formation. C) Native PAGE of Dual Targeting protein and human mature mesothelin. Lane 1 and lane 2 correspond to the Dual Targeting protein and rhmMSLN alone, respectively. Lane 3 shows the migration of an equimolar ratio of Dual Targeting protein and rhmMSLN, consistent with complex formation.

The binding kinetics of the A1 VHH and the Dual Targeting protein to rhmMSLN were quantitatively evaluated using Bio-Layer Interferometry (BLI) [Figure 44 A-B]. Biotinylated A1 VHH was immobilized on streptavidin biosensor, and a baseline was established by immersing the sensors in 1x KB. Association rate kinetic was measured by exposing the immobilized A1 VHH to six increasing concentrations of rhmMSLN. Dissociation rate kinetics were monitored by transferring the sensors into 1x KB. The association rate constant (k_{on}), dissociation rate constant (k_{off}), and equilibrium dissociation constant (k_D) were determined by global fitting of the sensorgrams obtained at the six rhmMSLN concentrations using a 1:1 binding model.

A K_D of 3.0±0.01 nM and 2.4±0.01 nM was determined for the A1 VHH and Dual Targeting protein, respectively [Figure 44 C]. Both proteins exhibited rapid association rate kinetics, with associates rate constant for approximately $3.3*10^5$ $M^{-1}s^{-1}$ for A1 VHH and ~$1.4*10^6$ $M^{-1}s^{-1}$ for the Dual Targeting protein, together with slow dissociation rate constant ~$1.1*10^{-3}$ s^{-1} for A1 VHH and ~$3.4*10^{-3}$ s^{-1} for the Dual Targeting protein. No statistically significant difference was observed between the K_D values of A1 VHH and the Dual Targeting protein for binding to rhmMSLN [Figure 44 D]. Importantly, this observation confirms that fusion of the ADAM10 Prodomain does not interfere with ability of the VHH to bind to mesothelin. Altogether, these results confirm the ability of A1 VHH to bind human mature mesothelin with a strong high affinity in a low nanomolar range even when fused to the ADAM10 Prodomain.

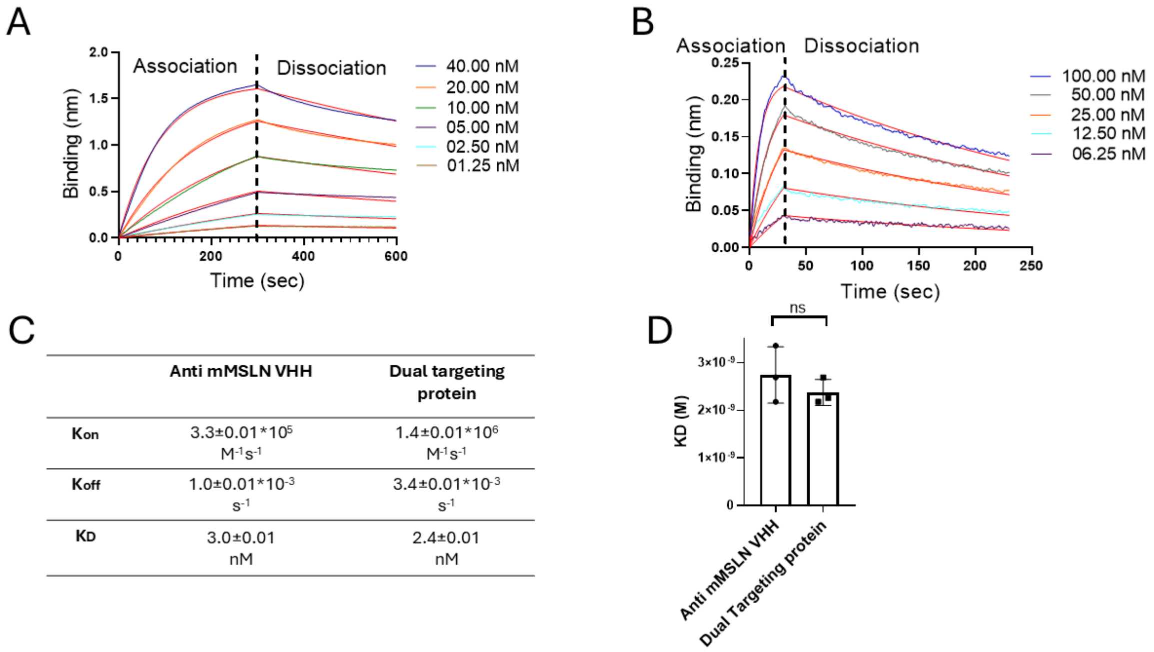

	Anti mMSLN VHH	Dual targeting protein
K_{on}	$3.3\pm0.01*10^{5}$ $M^{-1}s^{-1}$	$1.4\pm0.01*10^{6}$ $M^{-1}s^{-1}$
K_{off}	$1.0\pm0.01*10^{-3}$ s^{-1}	$3.4\pm0.01*10^{-3}$ s^{-1}
K_D	3.0 ± 0.01 nM	2.4 ± 0.01 nM

*Figure 44) A) Representative measurement of the affinity of A1 VHH for recombinant human mature Mesothelin by BLI. A vertical line divides the association from the dissociation step. The curves represent the binding of a single concentration of A1 VHH. In red, is the fitting of the data from which the K_D is obtained. Data were globally fitted accordingly to a 1:1 binding model by using the Data Analysis Octet Software Version 10.0 (Sartorius) B) Representative measurement of the affinity between the Dual Targeting protein and rhmMSLN. C) K_D, K_{on} and K_{off} values and their own mean ±SEM of A1 VHH and Dual Targeting protein. Three independent replicates were carried out. D) K_D values of V1 VHH and Dual Targeting protein are shown as mean ± SEM of three independent experiments and were compared using an unpaired students t-test ("ns" non significative, * $p<0.05$).*

4.4 Recombinant proteins cell-based characterization

4.4.1 A1 VHH shows no impact on healthy mesothelial and cancerous cell lines

To identify if the binding of A1 VHH to the mature mesothelin has any effects on mesothelium cell lines (Met5a) or cancerous cell lines (MSTO-211H and H28), changes in the cell metabolic activity, proliferation, and migration were assessed. Each experiment was carried out in triplicate, starting with different A1 VHH batches.

The MTT assay was used to evaluate the A1 VHH capacity to affect metabolic activity. No significant differences in cell metabolic activity were observed between A1 VHH treated cells and the corresponding controls across mesothelioma cell lines (H28 and MSTO-211H) as well as the non-malignant mesothelial cell line Met5a. This data indicates that binding of

A1 VHH to mesothelin does not affect cell metabolic activity [Figure 45 A]. The control condition consisted of the A1 VHH storage buffer (PBS supplemented with 50 mM sodium phosphate), applied at the same final dilutions as the protein treatments. A modest reduction in cell metabolic activity was observed at the highest concentrations for both A1 VHH and the control. Since this effect was also present in buffer-treated cells, it is attributed to the buffer composition, most likely the increased sodium phosphate concentration, rather than to a VHH specific effect.

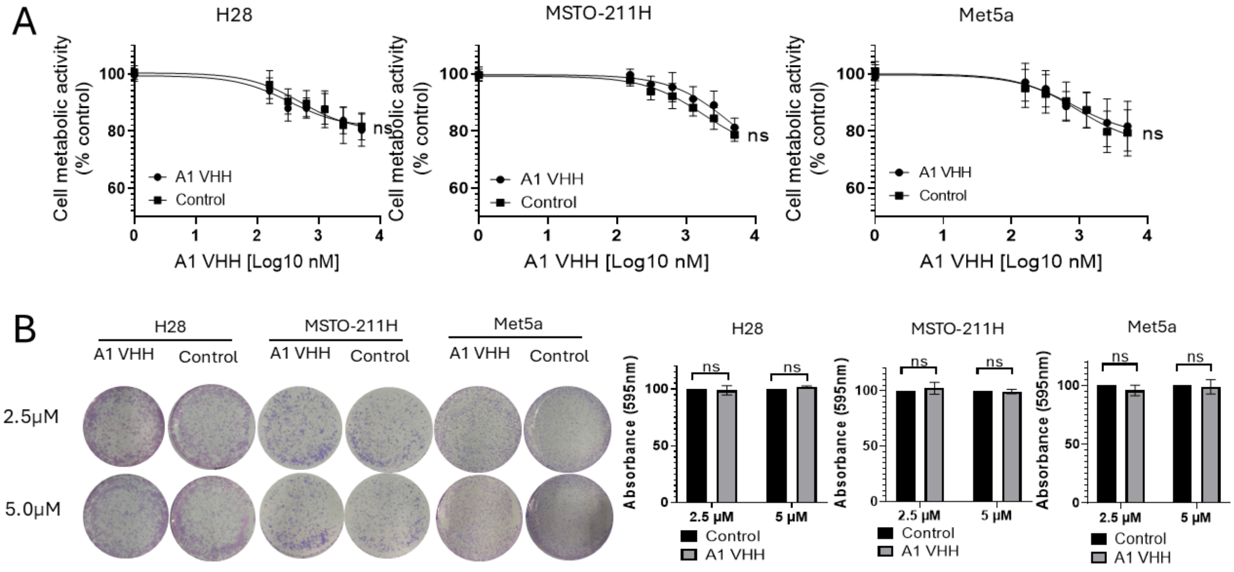

*Figure 45) A) MTT assay of H28, MSTO-211H and Met5a cells treated with A1 VHH or control. A1 VHH was tested at concentrations of 5, 2.5, 1.25, 0.6, 0.3, 0.1 and 0,05 µM. Cell metabolic activity is expressed as mean ±SEM. Statistical analysis was performed using two-way ANOVA followed by Sidak's multiple comparison test ("ns" non significative, *p <0.05). No significative differences were observed between treated and control samples for any cell lines. B) Clonogenic assay performed on H28, MSTO-211H and Met5a cells treated with A1 VHH or control at 2.5 and 5 µM. After colony formation, cells were fixed and stained with crystal violet. Representative colony images are shown. Colony formation was quantified by measuring crystal violet absorbance at 595 nm. Data are expressed as mean ± SEM. Statistical analysis was performed using unpaired student's t-test (*p < 0.05) comparing A1 VHH versus control at each concentration. No significant differences were observed between treated and control groups*

No significant differences have been observed in the proliferation assay [Figure 45 B] and in the wound healing assay [Figure 46], suggesting that the A1 VHH does not affect cell proliferation and migration, respectively. All this data confirms that the A1 VHH can be used to address the ADAM10 Prodomain safely since it does not affect cells.

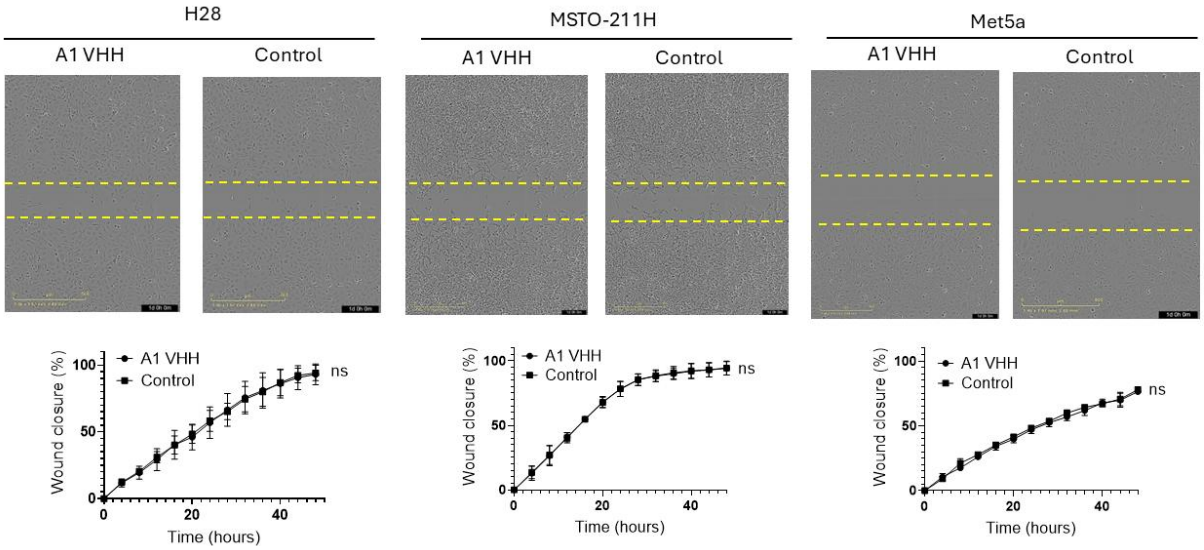

Figure 46) Wound-healing assay of A1 VHH and control in H28, MSTO-211H, and Met5a cells. Cells were seeded and allowed to adhere for 24 h before scratch wounding. Cell migration was monitored for 48 h using the Incucyte system, and wound closure was quantified every 4 h. Images taken 24 h after wounding (10× magnification) are shown for each condition. Graphs display the percentage of wound closure over time. Data are shown as mean ± SEM. Statistical analysis was performed using two-way ANOVA followed by Sidak multiple comparison test (*$p < 0.05$, *"ns" indicates no statistically significant difference between A1 VHH and control conditions).*

4.4.2 Dual Targeting protein and A1 VHH bind cells expressing mesothelin

The Dual Targeting protein and A1 VHH capacity to recognize mesothelin exposed at the surface of cell lines was evaluated by western blot and flow cytometry using 2 types of PM cell lines (H28, not expressing mesothelin and MSTO-211H, expressing mesothelin) and mesothelium cell line (Met5a, expressing mesothelin).

Western blot analysis of the 3 cell lysates [Figure 47 A] confirmed the expression of mMSLN on MSTO-211H and Met5a but not on H28 cells [219]. These data are consistent with the western blot results obtained using the A1 VHH [Figure 47 C]. A similar mesothelin-binding capacity was observed using the Dual Targeting protein, confirming its ability to bind mMSLN expressed on cells.

To further validate these results, flow cytometry experiments were carried out. Mesothelioma cell lines (MSTO-211H and H28), and mesothelium cells (Met5A) were incubated with A1 VHH or Dual Targeting protein. Cells were washed and stained with an anti VHH Ab. A fluorescence shift was observed with MSTO-211H and Met5a cells treated with A1 VHH. No shift was observed with the H28 cells [Figure 47 D]. The same shift pattern was observed using the anti mMSLN Antibody Alexa Fluor 647 [Figure 47 B]. Interestingly, the H28 cell line treated with the Dual Targeting protein displayed a different shift profile compared to cells treated with A1 VHH or anti mMSLN antibody alone. As previously reported, H28 cells do not express mesothelin [219], and the A1 VHH does not bind H28 cells. However, a fluorescence shift was observed in H28 cells treated with the Dual Targeting protein, suggesting a possible binding via the ADAM10 Prodomain component on ADAM10 proteins exposed on H28.

This evidence supports the ability of the A1 VHH and Dual Targeting protein to bind mesothelin-expressing cells and indicates that the ADAM10 Prodomain may contribute to additional binding properties. Moreover, these data confirm the capacity of the A1 VHH to recognize cells expressing mMSLN.

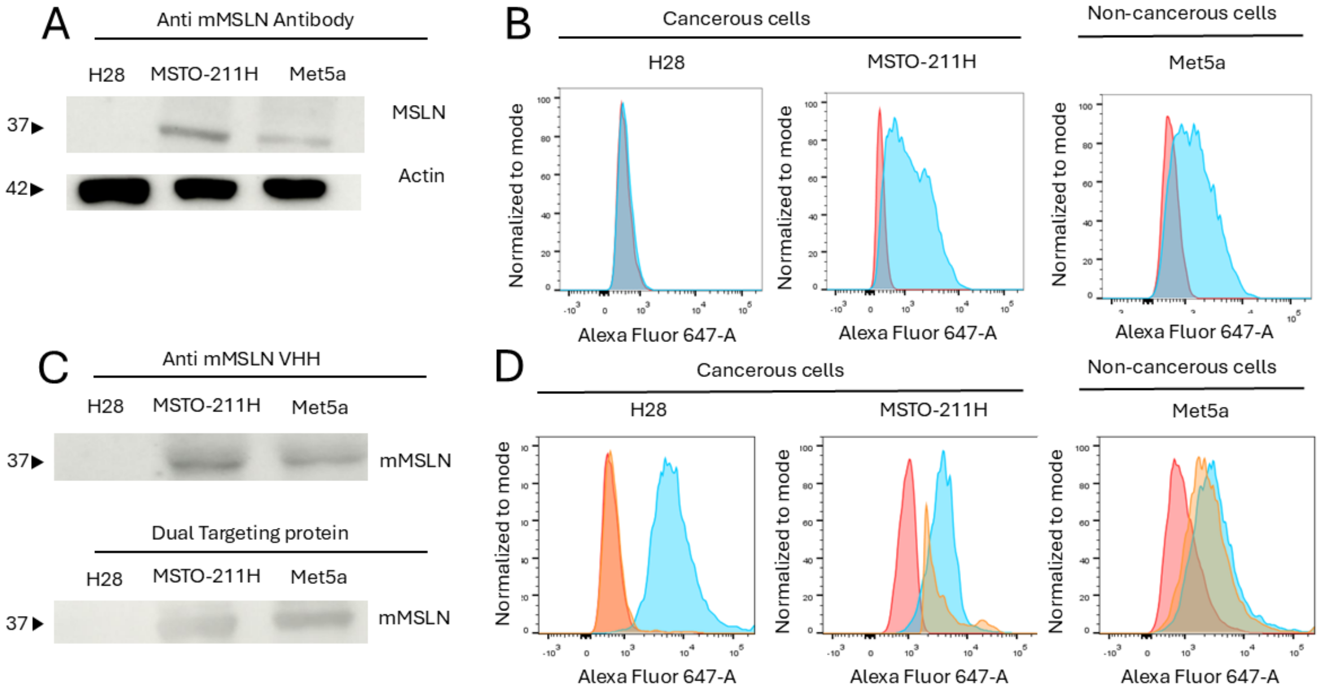

Figure 47 A) Western blot analysis of mMSLN expression on the surface of H28 and MSTO-211H mesothelioma cell lines and Met5a non-cancerous mesothelial cells using an anti mMSLN antibody. B) Flow cytometry analysis of H28, MSTO-211H, and Met5a cells labelled with anti mMSLN antibody conjugated to Alexa Fluor 647 (cyan) compared to unstained controls (red). C) Western blot analysis of A1 VHH or Dual Targeting protein binding to mMSLN expression in H28, MSTO-211H, Met5a cell. D) Flow cytometry of H28, MSTO-211H and Met5a cell treated with A1 VHH (orange), or Dual Targeting protein (cyan) compared to the control (red).

4.4.3 The Dual Targeting protein affects cell metabolic activity and cell proliferation on cancerous cells via its ADAM10 Prodomain

The effects of ADAM10 Prodomain and the Dual Targeting protein on cell metabolic activity, proliferation, and migration were evaluated in mesothelioma cell lines (H28, MSTO-211H) and non-malignant Met5a cells. Both proteins significantly reduced the metabolic activity of H28 and MSTO-211H cells in a dose-dependent manner, while Met5a cells remained largely unaffected [Figure 48 A]. Clonogenic assays [Figure 48 B] confirmed these findings: with H28 cells, ADAM10 Prodomain and Dual Targeting protein exhibited comparable anti-proliferative effects at 1.25 µM and 2.5 µM, whereas with MSTO-211H cells, the Dual Targeting protein was less effective than the ADAM10 Prodomain, likely due to its preferential binding to mMSLN, limiting interaction with ADAM10 molecules not co-localized with mMSLN.

Interestingly, Met5a cells showed no significant response to the Dual Targeting protein, but treatment with 2.5 µM ADAM10 Prodomain resulted in a significant reduction in proliferation. Migration analysis using scratch assay revealed that both proteins markedly impaired wound closure in H28 and MSTO-211H cells [Figure 49], consistent with previous reports of delayed migration upon ADAM10 inhibition [62]. Notably, migration was also reduced in Met5a cells despite minimal changes in metabolic activity and proliferation. Collectively, these results highlight the potential of ADAM10 Prodomain and Dual Targeting protein to selectively disrupt malignant cell growth and migration, with the ADAM10 Prodomain exerting an effect even in non-cancerous cell types.

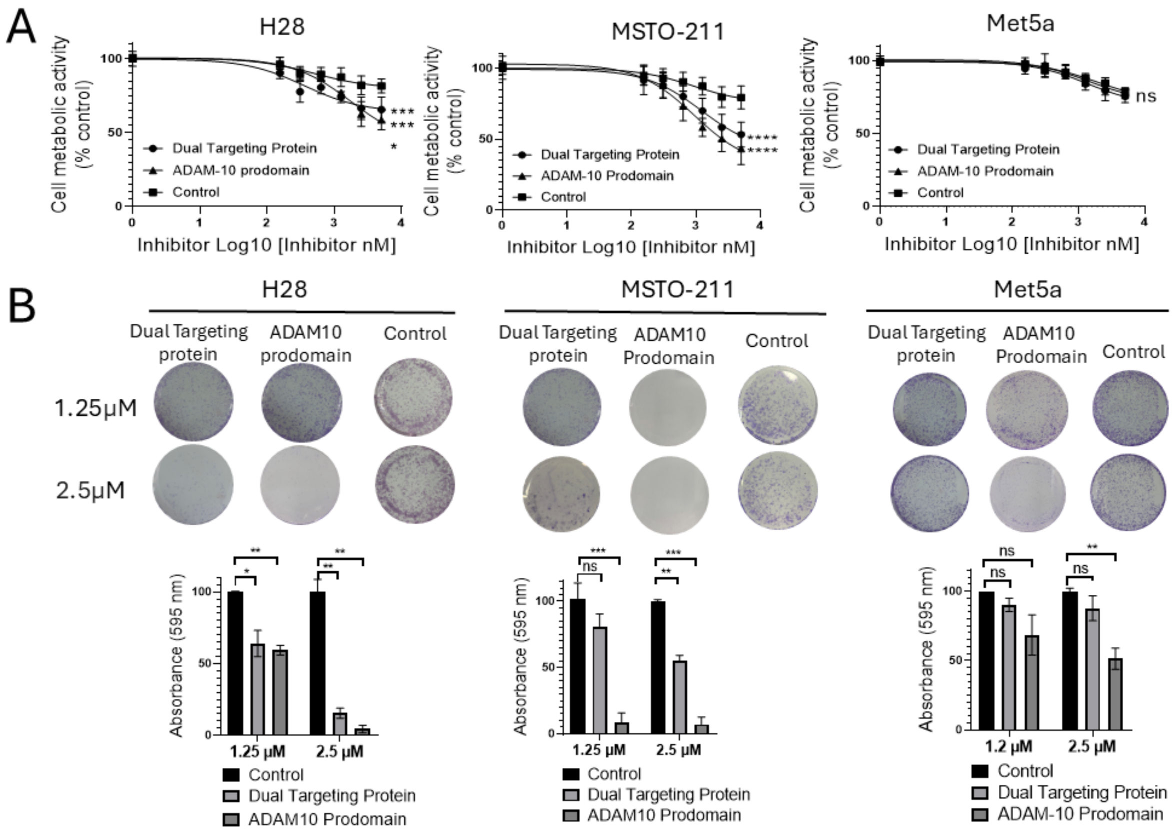

*Figure 48) Effect of ADAM10 Prodomain and Dual Targeting protein on cell metabolic activity and clonogenic growth. A) MTT assay of H28, MSTO-211H and Met5a cells treated with Dual Targeting protein, ADAM10 Prodomain and control. Proteins were tested at different concentrations (5, 2.5, 1.25, 0.6, 0.3 and 0.15µM). Data are shown as mean ± SEM. Statistical analysis was performed using two-way ANOVA followed by Dunnett's multiple comparison test versus control ("ns" non significative, *p <0.05, **p<0.01, ***p<0.001. B) Clonogenic Assay of H28, MSTO-211H and Met5a cells treated with Dual Targeting protein, ADAM10 Prodomain and Control (1.25 and 2.5 µM). Colony formation was quantified by crystal violet absorbance at 595 nm. Data is shown as mean ± SEM. For each concentration, statistical differences among groups were analyzed separately using one-way ANOVA followed by Dunnett's multiple comparison ("ns" non significative, *p <0.05, **p<0.01).*

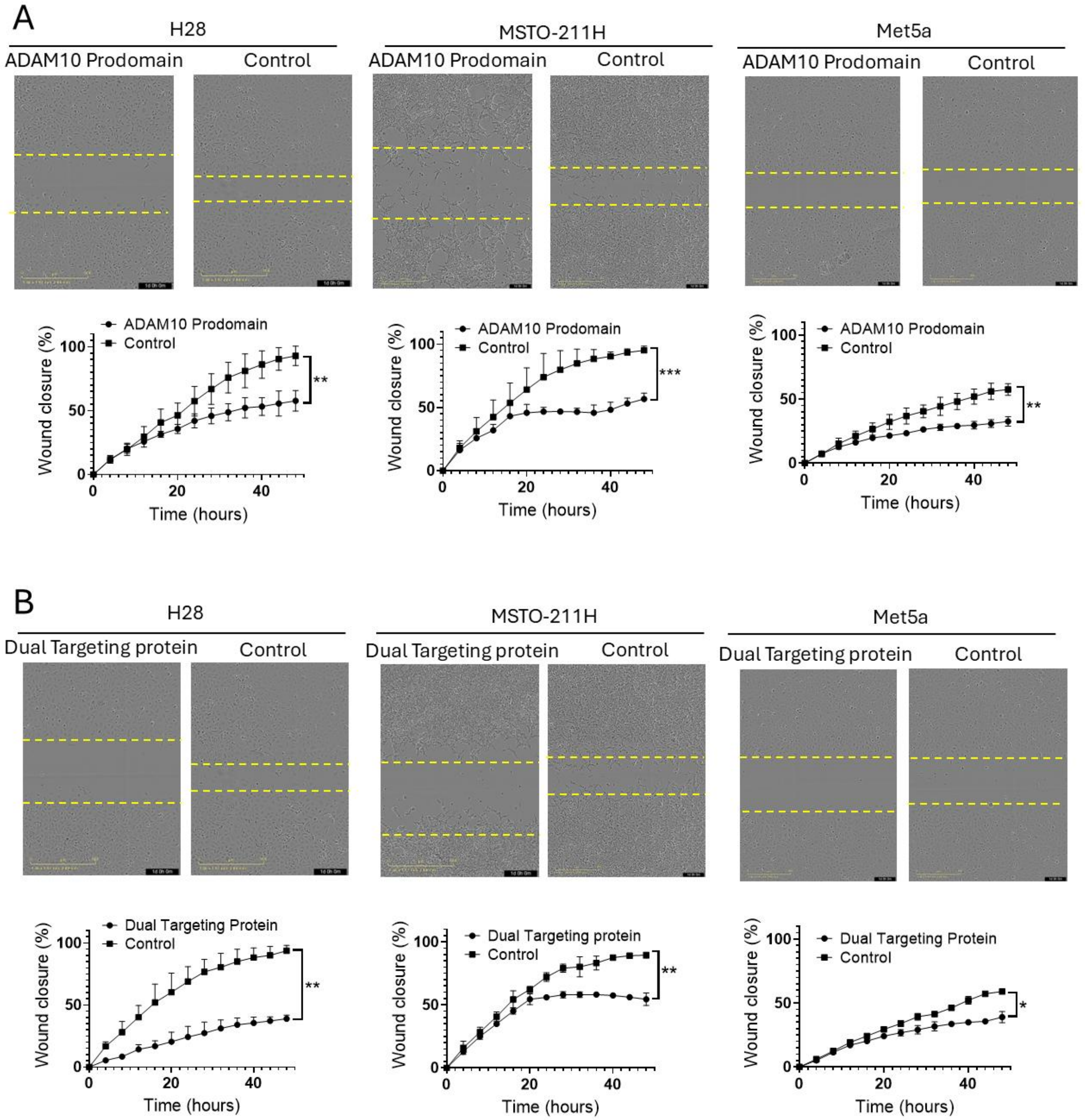

Figure 49) Effect of ADAM10 Prodomain and Dual Targeting protein. A) Wound Healing Assay performed on H28, MSTO-211H and Met5a cells treated with ADAM10 Prodomain or control. Cells were seeded and allowed to adhere for 24h before scratch wounding. Cell migration was monitored for 48 h using Incucyte system, and wound closure was quantified every 4h. Representative images acquired 24 h after wounding are shown, while graphs depict the percentage of wound closure over time. Data are shown as mean ± SEM. Statistical significance was performed using two-way ANOVA followed by Sidak multiple comparison test (**p < 0.05, **p < 0.01, ***p<0.001). B) Wound Healing Assay performed on H28, MSTO-211H and Met5a cells treated with the Dual Targeting protein or control. Experimental conditions and data acquisition were performed as described in (A). Data are shown as mean ± SEM. Statistical analysis was performed using two-way ANOVA followed by Sidak's multiple comparison test (*p < 0.05, **p < 0.01).*

To assess the specificity and the avidity of the Dual Targeting protein in PM cells, wound healing assays were performed on MSTO-211H, H28, and Met5A cell lines following treatment with ADAM10 Prodomain, A1 VHH, or the Dual Targeting protein. After incubation, extensive washes were performed to remove unbound proteins, and a scratch was performed to monitor cell migration over time.

Treatment with the ADAM10 Prodomain or A1 VHH alone did not significantly affect migration in any cell line compared to untreated controls. ADAM10 Prodomain likely dissociates during the washing steps due to its probable limited binding avidity and faster dissociation rates. Consistently, Dual Targeting protein treatment did not alter migration in H28 cells, which lack of mesothelin expression, resulting in low surface retention of the fusion protein [Figure 50 A]. Met5A cells, although expressing both ADAM10 and mMLSN, showed no significant change in migration, likely due to their relatively low expression levels compared to malignant cells, limiting efficient dual engagement [Figure 50 B].

In contrast, MSTO-211H cells, which overexpress both targets, exhibited a pronounced reduction in migration upon Dual Targeting protein treatment [Figure 50 C]. This effect was not observed with either monovalent construct alone and reflects the requirement for simultaneous binding of both targets. By engaging in the mesothelin through the A1 VHH and ADAM10 Prodomain, the Dual Targeting protein achieves increased binding avidity and prolonged cell surface retention, allowing it to remain associated after washing and to exert biological effects.

These findings demonstrate that the functional activity of the Dual Targeting protein relies on dual receptor engagement mediated by its two moieties, conferring selectivity toward PM cells with high co-expression of ADAM10 and mesothelin and supporting its therapeutic potential.

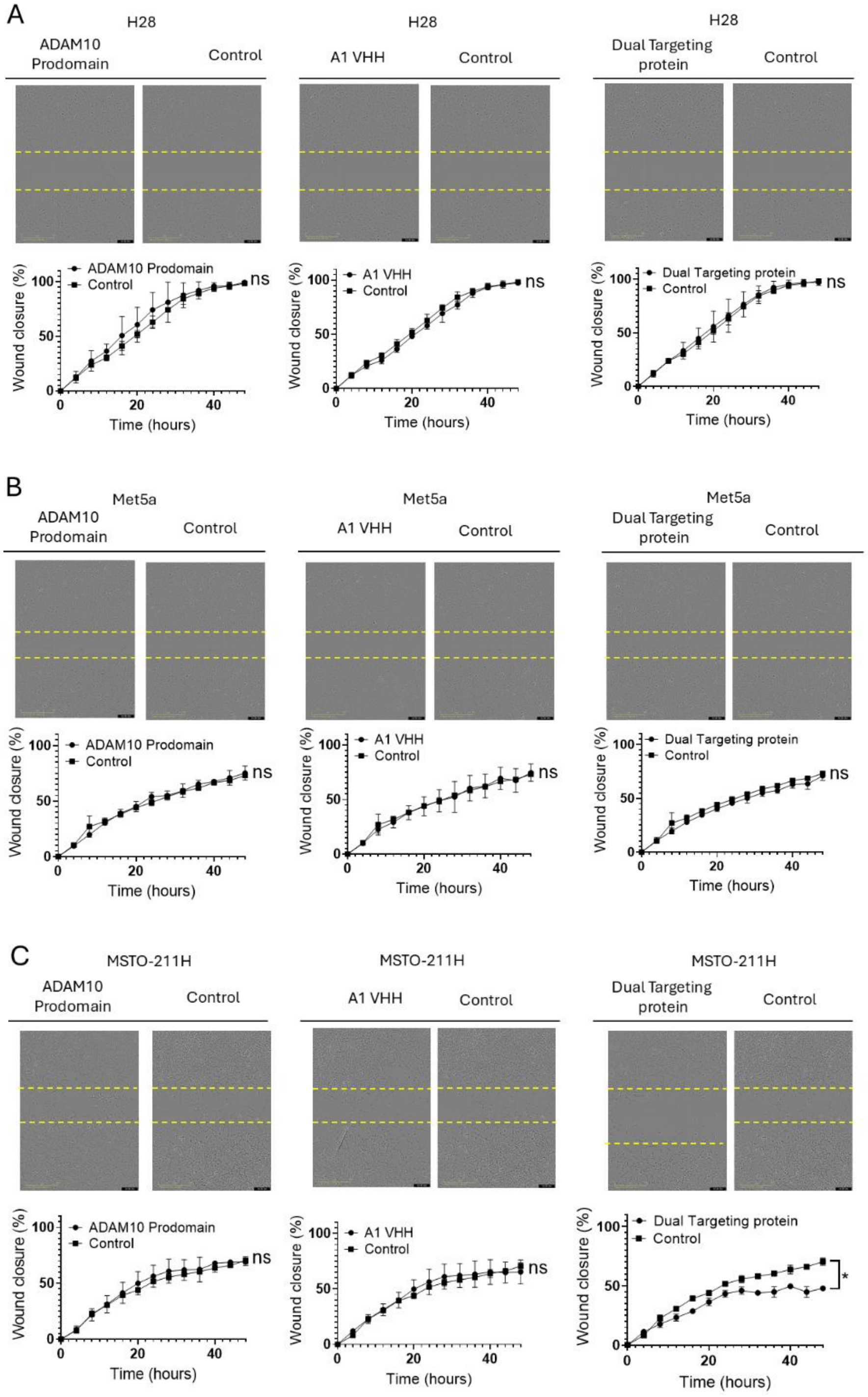

*Figure 50) Wound Healing Assay to evaluate the specificity of Dual Targeting protein. Cells were pre-incubated with ADAM10 Prodomain, A1 VHH, or the Dual Targeting protein and then washed to remove weakly bound recombinant proteins. A scratch wound was generated, and cell migration was monitored for 48 h using Incucyte system, with wound-closure quantification acquired every 4 h. Images were acquired 24 h after wounding are shown, and graphs depict the percentage of wound closure over time (mean ± SEM). For each cell line, statistical analysis was performed using two-way ANOVA followed by Sidak's multiple comparison test to compare each treatment with its matched control ("ns" non significative, *p < 0.05). A) Wound Healing Assay of ADAM10 Prodomain, A1 VHH and Dual Targeting protein and control on H28. B) Wound Healing Assay of ADAM10 Prodomain, A1 VHH and Dual Targeting protein and control on Met5a C) Wound Healing Assay of ADAM10 Prodomain, A1 VHH and Dual Targeting protein and control on MSTO-211H.*

4.5 *In vivo* characterization of the Dual Targeting protein

4.5.1 The Dual Targeting protein reaches mice bloodstream

The systemic exposure of the Dual Targeting protein was evaluated using an anti VHH ELISA. Mice received intraperitoneal injections of the Dual Targeting protein at doses of 1 mg/kg (0.02 µmol/kg), 10 mg/kg (0.25 µmol/kg) and 40 mg/kg (1 µmol/kg), or vehicle control. Blood samples were collected from the tail vein 1 h post-injection, and complete blood was obtained from the abdominal aorta at 4 h post-injection following euthanasia. Plasma was analyzed to quantify the Dual Targeting protein. At the 40 mg/kg dose, the protein was detectable at 1 h (2.43±0.67 ng/mL n=3) but exhibited a significant decrease at 4 h (0.26±0.23 ng/mL n=3), indicating a fast clearance [Figure 51 A]. A similar trend was observed at 10 mg/kg at 1 h (0.86±0.12ng/mL n=3) and 4 h (0.34±0.25 ng/mL n=3) [Figure 51 B], although the difference between 1 and 4 h was not statistically significant. No detectable signal was observed in mice treated with 1 mg/kg even after 1 h post-injection. A clear-dose dependent plasma concentration was observed at 1 h, with the highest Dual Targeting protein plasma concentration corresponding to the 40 mg/kg dose, the highest administrated dose [Figure 51 C]. By 4 h post-injection, plasma levels had markedly decreased across all dose groups and were low and highly variable, resulting in overlapping values and no statistically significant differences between doses [Figure 51 D]. This profile is consistent with the capacity of the Dual Targeting protein to reach the plasma and being able to reach the tumor site.

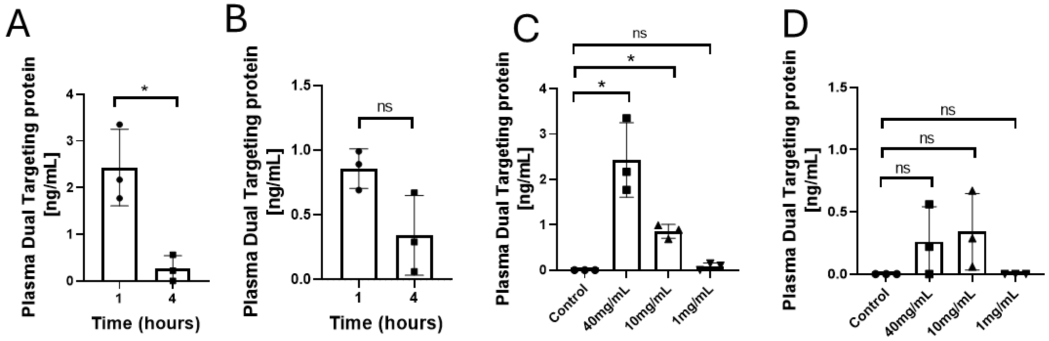

*Figure 51) ELISA quantification of Dual Targeting protein levels in mouse plasma. Plasma samples were collected via tail vein at 1 h post injection and via abdominal aorta at 4 h post-injection. A) Mice treated with 40 mg/kg of Dual Targeting protein showed a significant reduction in plasma concentration at 4 h compared to 1 h post-injection. B) Mice treated with 10 mg/kg of Dual Targeting protein displayed detectable plasma levels at both time points, with no significant decrease between 1 h and 4 h. For panels A B, data are shown as mean ± SEM (ng/mL). Statistical significance was assessed using unpaired student's t-test (ns, not significant; *p<0.05). C) At 1 h post-injection, plasma concentrations of the Dual Targeting protein increased in a dose-dependent manner across the tested doses. D) At 4h post-injection, plasma levels were low and highly variable, with no statistically significant differences among dose groups. For panels C) and D), data are shown as mean ± SEM (ng/mL). Statistical significance was performed using one-way ANOVA with Dunnett's multiple comparison test versus control (ns, not significant; *p<0.05).*

4.5.2 The Dual Targeting protein decreases tumor progression *in vivo*

To assess the efficacy of the Dual Targeting protein in reducing tumor progression, mice bearing MSTO-211H xenografts were treated starting three days post-tumor implantation. Treatments were administered intraperitoneally three times per week for 35 days with either 10 mg/kg (0.25 µmol/kg) or 40mg/kg (1 µmol/kg) of the Dual Targeting protein, 10mg/kg (0.56 µmol/kg) or 40 mg/kg (2.23 µmol/kg) ADAM10 Prodomain or control [Figure 52].

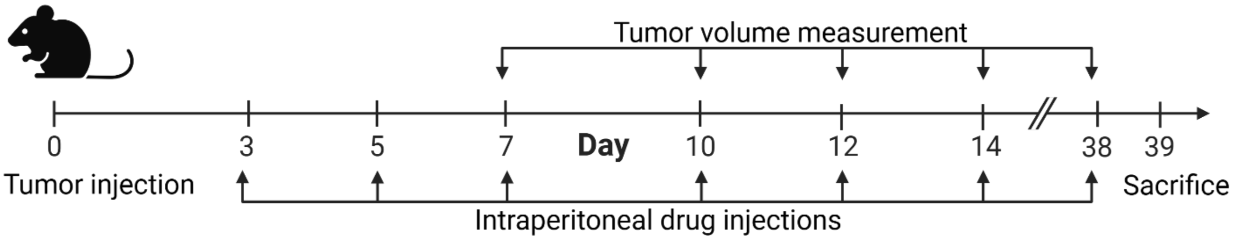

Figure 52) Schematic timeline of the mouse experiments. Nude Athymic mice (n=4 per group) were subcutaneously injected with MSTO-211H cells in both flanks. On day 3, mice received intraperitoneal injections of 10 mg/kg, 40mg/kg of Dual Targeting protein, 10 mg/kg or 40mg/kg of ADAM10 prodomain or control, administered three times per week. Tumor volume was measured using caliper starting on day 7, three times per week. Mice were sacrificed on day 39.

Mouse body weight was monitored three times per week throughout the treatment period [Figure 53 A]. No signs of toxicity were observed in any treatment group, including mice treated with the highest dose of the Dual Targeting protein or the ADAM10 Prodomain. This is particularly relevant given the essential role of ADAM10 in normal physiology and the embryonic lethality observed in ADAM10 knockout mice [81].

Tumor volume was measured three times per week using a caliper. A significant reduction in tumor volume was observed in mice treated with 10 mg/kg of the Dual Targeting protein compared to the control group [Figure 53 B]. In contrast, no significant differences were detected in mice treated with 10 mg/kg or 40mg/kg of ADAM10 Prodomain alone, indicating that ADAM10 inhibition without tumor targeting is insufficient to elicit an anti-tumoral effect [Figure 53 C,E]. Interestingly, treatment with 40mg/kg of the Dual Targeting Protein did not result in tumor volume reduction, which limits the benefit of higher dosing for small, VHH-based constructs [Figure 53 D].

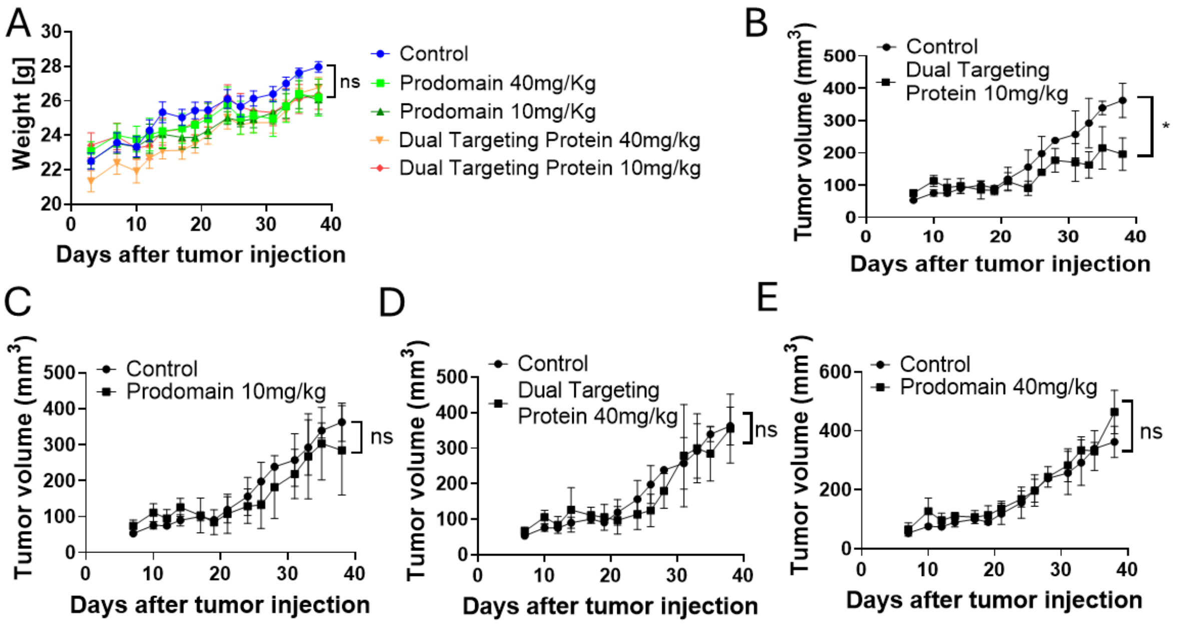

Figure 53) Evaluation of Dual Targeting protein and ADAM10 Prodomain effects on MSTO-211H tumor growth in nude athymic mice. A) Body weight monitoring of nude athymic mice bearing MSTO-211H tumors during the treatment period. Body weight is expressed in grams as mean ± SEM. Statistical analysis was performed using two-way ANOVA followed by Dunnett's multiple comparisons test versus control ("ns", non-significant). No statistically significant differences in body weight were observed between treated and control groups, indicating the absence of treatment-related toxicity. B-E) Tumor

volume progression over time for each treatment group. Tumor volume is expressed as mm^3 *and data are shown as mean ± SEM. Statistical significance was evaluated using two-way ANOVA followed by Sidak's multiple comparison test ("ns", not significant; *p<0.05).*

After euthanasia, tumors were excised and weighed. Although no statistically significant differences in tumor weight were observed between the control and the 10 mg/kg Dual Targeting protein group, a trend toward reduced tumor mass was noted, consistent with the caliper-based volume measurements [Figure 54 A]. No significant differences in tumor weight were observed in mice treated with the highest concentrations of either ADAM10 Prodomain or the Dual Targeting protein [Figure 54 A]. These observations are supported by visual inspection of the excised tumors [Figure 54 B]. An additional study including a larger cohort of mice and evaluating the same treatment conditions must be performed to increase statistical power and validate these findings.

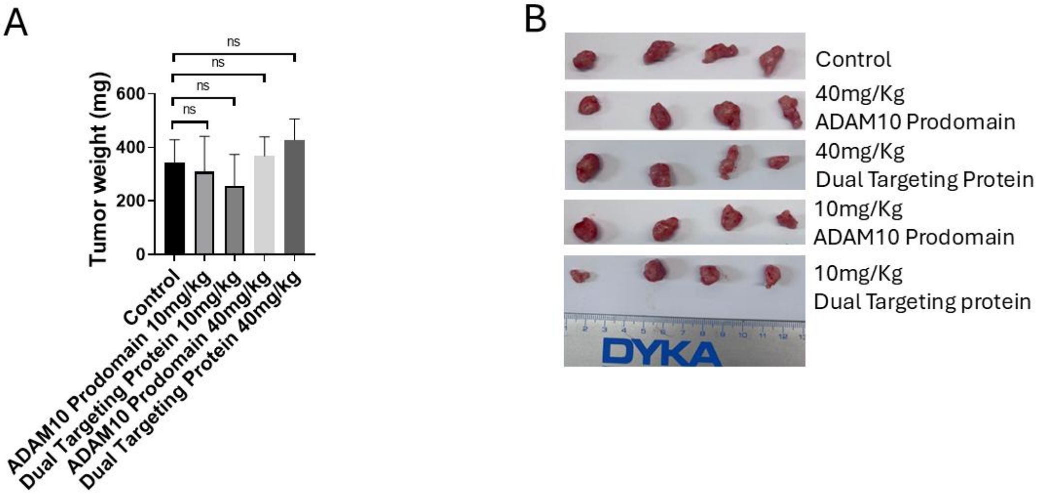

*Figure 54) A) Tumor weight comparison at endpoint (day 39). No statistical differences have been observed between the samples treated and the control. Statistical significance was performed using One-Way ANOVA followed by Dunnet's multiple comparison test versus control ("ns", not significant; *p<0.05). B) Macroscopic appearance of the resected tumors from the five treatment groups, shown from top to bottom: Control, 40mg/Kg ADAM10 prodomain, 40mg/Kg Dual Targeting protein, 10mg/kg ADAM10 prodomain, 10mg/kg Dual Targeting protein.*

4.5.3 The Dual Targeting protein affects the cell proliferation measured in tumors

To evaluate the effect of the treatment on tumor cell proliferation and tumor vascularization, paraffin embedded sections of MSTO-211H xenografts were deparaffinized, subjected to antigen retrieval, and incubated with a primary antibody against Ki-67 or CD31, followed by an HRP-conjugated secondary antibody.

Ki-67 is a nuclear protein expressed during all active phase of the cell cycle (G1, S, G2 and M) but absent in quiescent cells (G0), making it a well-established marker of cell proliferation. High Ki-67 expression indicates rapid cell division. Detection was performed using DAB, and counterstaining was applied to visualize tissue morphology. The analysis revealed no significant differences in Ki-67 expression following treatment with the Dual Targeting protein or ADAM10 Prodomain [Figure 55 A].

CD31 is an endothelial cell marker commonly used to assess tumor vasculature and micro vessel density. Analysis of CD31 staining, revealed a non-significant difference in the percentage of CD31 positive areas in tumors treated with both the Dual Targeting protein and the ADAM10 Prodomain compared to control samples.

Overall, these results indicate that, under the experimental conditions employed, neither treatment significantly impacted tumor proliferation or vascularization.

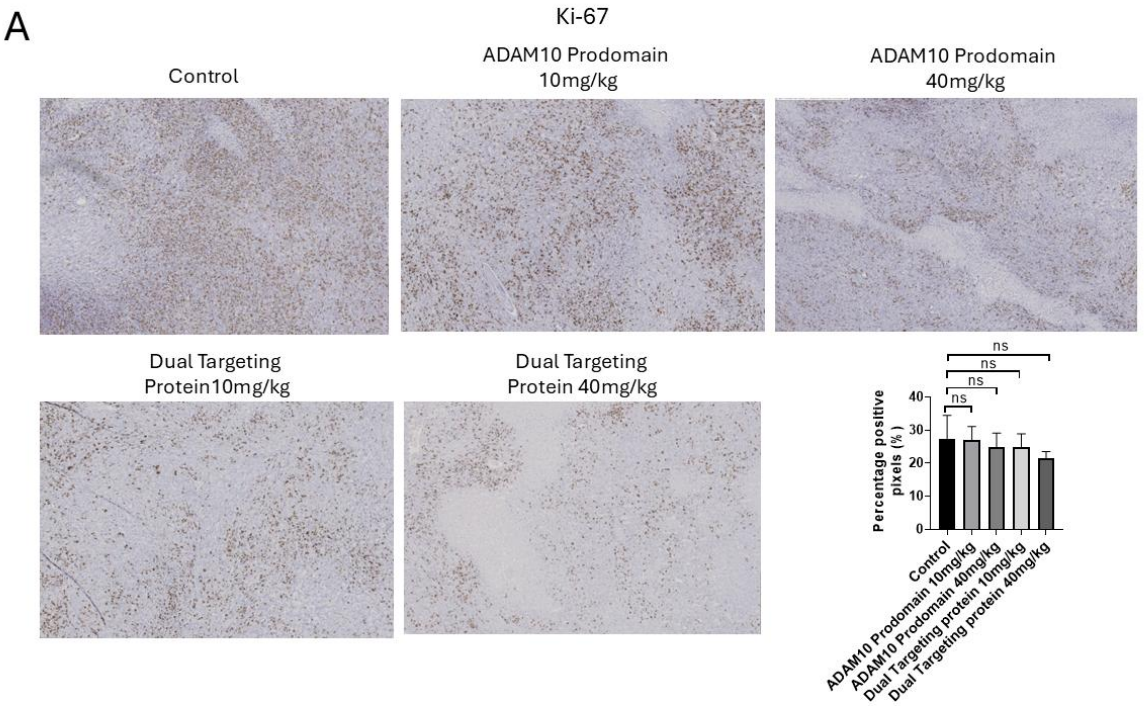

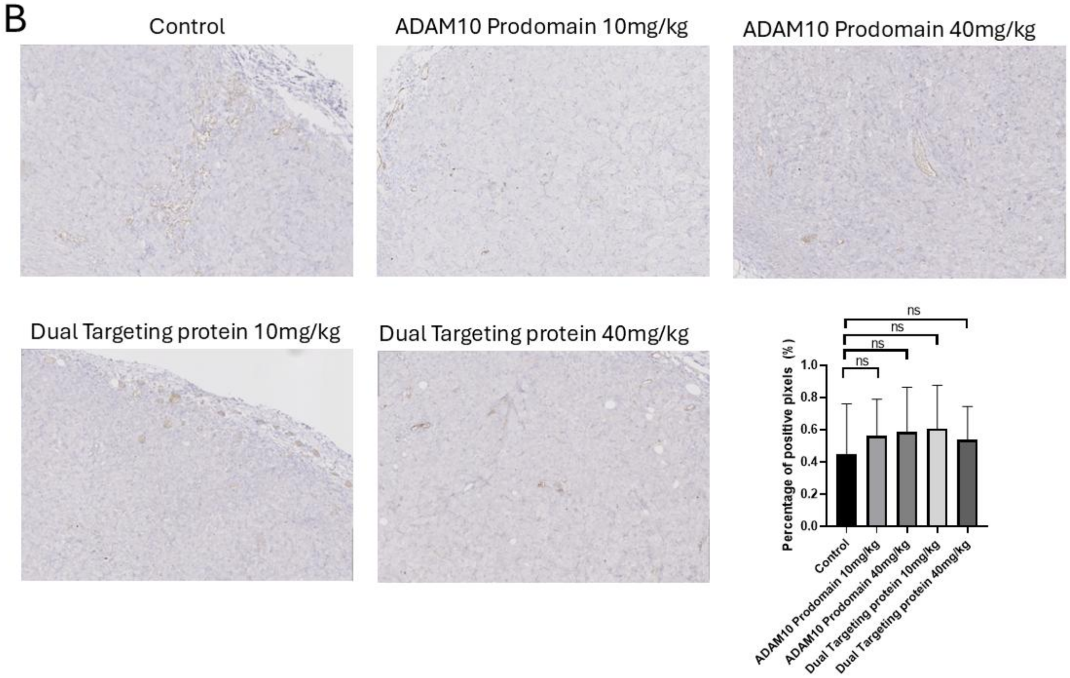

*Figure 55) Histological analysis of cell proliferation and vascularization in tumor tissue samples following treatment with ADAM10 Prodomain and Dual Targeting protein. A) Immunohistochemical staining for Ki-67, a marker of cell proliferation, in tissue section from Control, ADAM10 Prodomain (10mg/kg, 40mg/kg) and Dual Targeting protein (10mg/kg, 40mg/kg). B) Immunohistochemical staining for CD31 in the same experimental groups. For each sample, the percentage of positive pixels was quantified using QuPath software and expressed as a percentage of the total analyzed area. Data are presented as mean ± SEM. Statistical analysis was performed using the one-way ANOVA with Dunnet's multiple comparison, comparing each treatment group to the control. ns indicates non-significant differences (ns, *p<0.05).*

5 - Discussion

5 - Discussion

PM is a clinical challenge despite decades of research, due to its aggressive nature, long latency period, and limited response to available therapies [48]. Significant efforts have sought to understand the molecular mechanisms driving PM progression and to identify new therapeutic targets. Among these, ADAM10 has emerged as a central player in processes such as cell migration [66]. Parallel to this, mMSLN has been widely recognized for its highly selective overexpression on malignant mesothelial cells [206]. This combination offered a strong rationale for designing a targeted therapeutic strategy aimed at modulating ADAM10 activity specifically on PM cells. The purpose of this project was therefore to engineer, characterize, and evaluate a Dual Targeting protein capable of simultaneously binding to mesothelin and inhibiting ADAM10 activity, with the goal of developing a biologically selective inhibitor suitable for translational application.

The selection of ADAM10 as a therapeutic target is based on its capacity to regulate the shedding of numerous substrates implicated in tumorigenesis, including growth-factor receptors and adhesion molecules. In PM, ADAM10 has been linked to increased cell migration and tumor progression [66]. Previous studies demonstrated that silencing ADAM10 impairs the invasive properties of mesothelioma cells and reduces key proteolytic events such as N-cadherin cleavage [66]. Given that the NTF (N-cadherin terminal fragment) can promote pro-tumorigenic signaling such as FGFR activation, thus reducing ADAM10 activity could have substantial therapeutic benefit.

However, ADAM10 is also ubiquitously expressed in normal tissues and plays essential roles in embryonic development, and neuronal function, and more generally in the body homeostasis. Systemic inhibition of ADAM10 is therefore not feasible as it will perturb a series of essential processes. This is reflected in the lethality of ADAM10 knockout mice [81], and the toxicity observed following the uses of broad-spectrum metalloprotease inhibitors as observed for the small molecule GI254023X [220]. This duality, high therapeutic potential of inhibiting ADAM10 but high risk, motivated the strategy of employing the ADAM10

Prodomain as an intrinsically selective inhibitor, and its inhibiting activity was restricted to tumor cells through mesothelin-mediated targeting.

Thus, the overall therapeutic rationale rests on two pillars: i) ADAM10 is a validated target that drives PM progression, and ii) selective, localized inhibition is necessary to avoid systemic toxicity. The Dual Targeting protein approach developed in this work directly addresses both challenges.

5.2 Assessment of the phage display approach for identifying ADAM10 inhibitors

The first objective of this research was to explore whether short inhibitory ADAM10 peptides could be identified using M13 phage display. Although inhibitory peptides have been successfully developed for several proteases using this approach, including ADAM17 [98], the success of phage display strongly depends on the selection stringency, the biophysical nature of the proteases, and the extent to which phage library diversity is effectively sampled during biopanning [222–224].

In this study, two complementary phage display strategies were implemented: one using commercial recombinant human ADAM10 ECD as the target, and the other using H28 cells overexpressing ADAM10. In both strategies, a competitive counter-selection step was introduced using the small-molecule inhibitor GI254023X. GI254023X was used to occupy the catalytic pocket of ADAM10, thereby enabling discrimination between peptides whose binding depends on an accessible active site and those interacting with non-catalytic regions. Under these conditions, phages retaining binding properties in the presence of GI254023X were considered non active site binders and were removed from the selection pool, whereas phages that failed to bind when the active site was blocked were retained, as their interaction was presumed to depend on the catalytic pocket. While this strategy is theoretically suitable for identifying active site-depending binders, several key limitations emerged.

A critical constraint was the limited sequencing depth, as only the G3P gene of 30 phages per round were analyzed by Sanger sequencing. Given that the diversity of a phage library can exceed 10^{13} unique variants, and that enrichment typically requires the evaluation of thousands of clones, particularly in early rounds, sampling only 30 sequences severely restricted the ability to detect selection patterns. To address this limitation, NGS was implemented to increase the number of analyzed sequences and improve enrichment detection. However, NGS analysis revealed a persistent dominance of wild-type phages across selection rounds.

The overrepresentation of wild type phages (i.e., phages lacking a peptide insert) has been previously reported for NEB phage libraries. Sloth *et al* [215] described both a high proportion of non-insert phages and deviations from full peptide sequence randomness. Such wild type phages can acquire a selective propagation advantage, as the absence of a displayed peptide reduces structural constraints on the G3P fusion protein during membrane translocation and periplasmic folding. Allowing these clones to outcompete peptide-displaying phages during amplification [215]. This propagation bias likely masked the enrichment of ADAM10 binders in our selections, resulting in only a modest increase in the anti ADAM10-4 peptide frequency.

An additional limitation relates to the structural nature of ADAM10 itself. As a multi-domain metalloprotease with a complex extracellular domain folding and glycosylation pattern [76], recombinant ADAM10 expressed *in vitro* may not fully recapitulate the native conformation present at the cell surface. This discrepancy may influence peptide binding and selection outcomes. Although this limitation was partially addressed through cell-based biopanning on ADAM10-overexpressing H28 cells, whole cell selections introduce additional biases related to receptor density, and steric accessibility [225].

More generally, the phage display approach for selecting short inhibitory peptides presents intrinsic limitations. The small size of linear peptides restricts the available binding interface, which may limit both affinity and selectivity toward ADAM10, particularly in crowded cellular environment. This constraint is especially relevant for protease such as ADAM10, whose catalytic cleft and substrate-recognition regions are embedded within a large, multidomain architecture [76].

Following phage display selection, candidate peptides were prioritized through *in silico* docking on the ADAM10 extracellular domain, with particular attention to binding proximity to the catalytic site and reductions in local protein flexibility. Among the identified candidates, anti ADAM10-4 displayed partial inhibitory activity against recombinant ADAM10 *in vitro*. However, its lack of activity in cell-based assays suggests that its binding affinity, stability, or binding mode may be insufficient under physiological conditions.

To overcome these limitations and improve binding affinity and functional efficacy, alternative strategies had to be considered. These include the use of alternative or more diverse peptide libraries, as well as the immunization of camelids to generate ADAM10-specific VHHs. Notably, several VHHs targeting and inhibiting proteases have been successfully described in the literature [214]. In parallel, the affinity of the candidate peptides such as anti ADAM10-4 could be quantitatively characterized using biolayer interferometry to determine kinetic parameters (K_{on}, k_{off} and K_D). Finally, peptide optimization strategies, such as in silico-guided amino acid substitution followed by experimental validation, could be applied prior to further functional evaluation in cell-based assays.

5.3 The ADAM10 Prodomain as a biologically validated inhibitor

The ADAM10 Prodomain is a natural autoinhibitory domain that maintains ADAM10 in a latent state during maturation. Importantly, ADAM10 Prodomain mediated inhibition is highly specific to its metalloprotease, making it an attractive alternative to synthetic inhibitors that often display broad off-target activity, due to the high degree of conservation within metalloprotease active sites [73,76]. Recombinant expressiion of the ADAM10 Prodomain in *E. coli* yielded protein of high purity, suitable for structural and functional analyses. Circular dichroism analysis confirmed the expected secondary structure composition, with a combination of α-helices and β-sheets, consistent with the known3D structure of ADAM10 Prodomain [73]. Thermal denaturation analysis revelated moderate stability, with unfolding onset temperature around 46°C. Although this limited stability under elevated temperatures may affect long-term shelf life, it does not preclude functional activity in cellular to tumor microenvironments. Moreover, ADAM10 Prodomain stability could potentially be enhanced in future iterations through sequence optimization or rational engineering approaches.

At the molecular level, the precise interactions between the ADAM10 prodomain, the catalytic site of ADAM10, and associated membrane protein complexes remain unresolved. High-resolution structural studies, such as molecular docking, molecular dynamics simulations, or X-ray crystallography, will be necessary to map the residues involved in prodomain binding and inhibition. Such structural insight would guide rational mutagenesis approaches aimed at improving inhibitory potency, specificity, and thermal stability.

In addition, determination of the K_D of the ADAM10 Prodomain for ADAM10 would enable a quantitative comparison with the A1 VHH and allow a better assessment of its binding strength and selectivity. We therefore attempted to characterize the binding kinetics between rhADAM10 and the ADAM10 Prodomain using Bio-Layer Interferometry (BLI).A major limitation was the inability to use anti-His biosensors, since both interaction partners carry a C-terminal His-tag, which would lead to the direct capture of both proteins on the sensor. To overcome this issue, the ADAM10 Prodomain was cloned into a vector containing a trypsin cleavage site between the prodomain sequence and the His-tag to allow tag removal. However, despite multiple optimization attempts, we were not able to obtain a homogeneous preparation of fully cleaved, tag-free ADAM10 Prodomain.

We also attempted to biotinylate the ADAM10 Prodomain for immobilization on streptavidin biosensors. However, since lysine residues are present close to the functional interface, random NHS-biotinylation likely impaired binding. Under these conditions, immobilized

ADAM10 Prodomain did not show measurable interaction with rhADAM10. Conversely, immobilization of biotinylated rhADAM10 also did not yield detectable binding to the ADAM10 Prodomain; further evaluation revealed that the lysine NHS-biotynilation impairs ADAM10 activity probably interfering with ADAM10 Prodomain capacity to bind ADAM10.

An alternative strategy that could be explored in future experiments would be site-selective biotinylation of the ADAM10 Prodomain via cysteine residues, which may reduce the risk of blocking the binding interface.

Functionally, the ADAM10 Prodomain effectively inhibited N-cadherin cleavage in PM cancer cells, demonstrating suppression of endogenous ADAM10 activity. This finding is particularly relevant in the context of PM biology, as N-cadherin cleavage generates the NTF fragment, that has been implicated in tumor progression [66]. Consistently, reduced N-cadherin proteolysis was associated with decreased cell migration, in agreement with previous reports linking ADAM10 activity to tumor progression behavior [66].

Interestingly, inhibition of cell migration was also observed in non-cancerous Met5a cells, in contrast with earlier studies based on ADAM10 knockdown [66]. One possible explanation is that genetic depletion of ADAM10 induces compensatory mechanisms that preserve migratory pathways, notably through functional compensation by ADAM17 [226]. Nevertheless, despite its inhibitory potency, the ADAM10 Prodomain lacks tumor selectivity and suppress the activity of ADAM10 on non-malignant cells. This limitation represents a critical concern for therapeutic development and strongly supports the need for a targeting strategy, here provided by the A1 VHH, which confers specificity toward mesothelin expressing tumor cells.

5.4 Mesothelin as a selective target for PM therapy

Mesothelin represents an ideal docking molecule for targeted therapies due to its low expression in healthy tissues and pronounced overexpression in several cancers, particularly PM. The A1 VHH used in this study is derived from camelid heavy-chain antibodies and possesses several advantages: small size, high solubility, strong stability, and the ability to bind cryptic epitopes [166].

The recombinant A1 VHH displayed characteristics consistent with known VHH properties, including proper folding and high thermal stability (Tm 69.9±0.9°C). Binding assays confirmed strong affinity for recombinant mature mesothelin (~3 nM) as well as the recognition of surface expressed mesothelin in live cells. Importantly, the VHH alone did not induce cytotoxic effect or impair cell proliferation, supporting its suitability as a non-perturbing targeting module in case of off-targeting binding.

The A1 VHH itself represents an interesting subject for further investigation. Structural characterization of A1 VHH in complex with mature mesothelin would enable precise epitope mapping and clarify whether A1 sterically interferes with the mesothelin–MUC16 interaction, as reported for the anti-mesothelin antibody MORAb-009 (amatuximab). Our preliminary data suggest that A1 VHH binds an epitope overlapping the MUC16-binding site and can partially inhibit MUC16 binding. If confirmed, this blocking activity could contribute to reducing mesothelin-driven cell adhesion and metastatic dissemination. Additional experiments are required to validate this mechanism including a BLI or ELISA competition assay.

Finally, comprehensive pharmacokinetic and biodistribution studies will be essential to evaluate tissue penetration and long-term safety.

5.5 Engineering and evaluation of the Dual Targeting protein

The central innovation of this thesis is the development of the Dual Targeting protein, generated by covalently fusing, via a peptide linker, the A1 VHH with the ADAM10 Prodomain. This bifunctional design enables simultaneous targeting of mesothelin-expressing tumor selectivity with pathway-specific modulation.

The recombinant Dual Targeting protein was successfully expressed and purified from *E. coli* and retained the structural characteristics of its individual components. Circular dichroism and intrinsic fluorescence analyses demonstrated that both domains preserved their secondary or tertiary structure upon fusion. Notably, the far-UV CD spectrum calculated by summing the individual spectrum of the A1 VHH and ADAM10 Prodomain, closely matched the experimentally obtained spectrum of the fusion construct. These findings indicate that covalent linkage does not induce major structural perturbation and that the overall architecture of the Dual Targeting protein remains intact.

Consistent with the observations for the ADAM10 Prodomain alone, the Dual Targeting protein exhibited limited thermal stability, with aggregation preventing accurate determination of the Tm. The similar onset temperature of unfolding observed for the fusion protein and the ADAM10 Prodomain, suggests that the prodomain is the principal contributor to thermal instability, and that the incorporation of the A1 VHH does not further destabilize the ADAM10 Prodomain. Despite this limitation, the functional integrity of both domains was fully preserved.

Western blot, native PAGE and Bio-Layer Interferometry analyses demonstrated that mesothelin binding affinity was fully retained in the fusion construct, indicating the absence of significant steric interference between domains. Likewise, ADAM10 inhibition assays confirmed that the prodomain preserved its inhibitory activity when fused to the A1 VHH. This compatibility is not trivial, as fusion proteins can suffer from misfolding or altered domain orientation [227].

Effective binding of the Dual Targeting protein to living cells was further confirmed by flow cytometry. As expected, the fusion construct is bound efficiently to mesothelin expression MSTO-211H and Met5a cells, similarly as observed for the A1 VHH alone. Interestingly, binding was also observed in H28 cells, which do not express mesothelin. This interaction was not detected with the A1 VHH alone and is therefore likely mediated by the ADAM10 Prodomain, potentially through direct interaction with ADAM10 expressed at the cell surface.

Functionally, the Dual Targeting protein induced significant reductions in cell metabolic activity, proliferation, and migration in MSTO-211H and H28 cells. In contrast, no significant effects on PM cell metabolic activity and proliferation were observed following ADAM10 knockdown [66]. This discrepancy may be explained by compensatory mechanisms triggered by genetic depletion of ADAM10. ADAM10 and ADAM17 share overlapping substrate specificities and partially redundant functions. Upregulation of ADAM17 following ADAM10 knockdown has been reported [226]. Such compensation may preserve sheddase-dependent signaling pathways involved in cell proliferation and survival, thereby attenuating the phenotypic consequences of ADAM10 loss. In contrast, the Dual Targeting Protein inhibits ADAM10 activity at the cell surface without inducing complete depletion of the enzyme, potentially limiting the activation of compensatory ADAM17-dependent mechanisms [226].

Although compensatory mechanisms, particularly involving ADAM17, are suggested by these findings, they were not systematically investigated in this study. Further studies will be required to elucidate these mechanisms underlying the differential effects observed between the Dual Targeting protein and genetic ADAM10 inhibition. These could include quantitative analysis of ADAM17 expression. In addition, combinatorial inhibition of ADAM10 and ADAM17 could help determine the functional relevance of such compensation.

In non-cancerous mesothelial Met5a cells, the metabolic activity and proliferation effects of the Dual Targeting protein were reduced compared to those observed with the ADAM10

Prodomain alone, demonstrating a gain in selectivity conferred by mesothelial-mediated targeting. The absence of ADAM10 and mesothelin overexpression in these cells is likely contributed to reduced off-target activity.

From a biological standpoint, functional validation was performed using two pleural mesothelioma cell lines and one non-cancerous mesothelial cell line. While these models were sufficient to demonstrate proof of concept, extending the analysis to a broader panel of PM cell lines, would strengthen the generalizability of the conclusions.

To further assess binding specificity, an additional migration assay was performed following extensive washing steps after treatment with the Dual Targeting protein, the A1 VHH, or the ADAM10 Prodomain. This stringent washing procedure was designed to remove low-avidity transient interactions, thereby retaining only strongly and stably bound recombinant proteins. Under these conditions, neither the ADAM10 Prodomain nor the A1 VHH alone affected cell migration. In contrast, the Dual Targeting protein retained a significant inhibitory effect on migration exclusively in MSTO-211H cells, further supporting the requirement for simultaneous binding of both functional domains to achieve stable cell surface retention and effective inhibition of tumor cell migration.

In vivo experiments provide the most compelling evidence of therapeutic potential. Following intraperitoneal administration in BALB/cJRj mice, the Dual Targeting protein was detected in plasma without signs of acute toxicity, consistent with the favorable safety profile of VHH based molecules. A dose-dependent plasma concentration was observed, together with rapid systemic clearance. This behavior is consistent with the relatively small molecular weight of the construct, even when considering the contribution of the ADAM10 prodomain. Although the fusion increases the overall molecular weight compared to a single VHH, the protein likely remains below the renal filtration threshold (~60kDa) [181,230], thereby favoring rapid clearance. Indeed, unmodified VHHs typically display a short plasma half-life of approximately 1-2 h and are predominantly cleared via renal filtration [228,229]. The pharmacokinetic profile of the Dual Targeting protein is therefore low [181,230].

The therapeutic efficacy was evaluated using an MSTO-211H xenograft in an athymic nude mouse model. Treatment with the Dual Targeting protein at 10mg/kg resulted in a significant reduction in tumor volume, confirming that targeted ADAM10 inhibitor can suppress tumor growth. Although tumor weight at endpoint did not show a statistically significant difference, a clear trend toward reduced tumor mass was observed. Increasing the dose to 40mg/kg failed to enhance antitumor efficacy, revealing a nonlinear dose response relationship. Similar U-shaped responses have been reported for other peptide-based therapeutics, where excessive dosing results in altered pharmacokinetics and pharmacodynamics due to target saturation, tissue distribution, or accelerated clearance [231].

Future *in vivo* studies will therefore be required to validate and extend these findings. In particular, detailed pharmacokinetic and biodistribution analysis. Repeated dosing will help to define the optimal therapeutic window and further clarify the non-linear dose response relationship. Extended treatment schedules and survival studies will enable a more comprehensive evaluation of the drug efficacy. In addition, future experiments will normalize dosing based on molar concentration rather than mg/kg in order to allow a direct comparison between the ADAM10 Prodomain and the Dual Targeting protein. Importantly, preliminary observations indicate that even when administered at a higher molar concentration, the ADAM10 Prodomain alone did not produce significant antitumor effects nor signs of toxicity, further supporting the added therapeutic value conferred by the targeted dual construct.

Further optimization of the Dual Targeting construct should include systematic evaluation of linker length and flexibility to improve domain orientation, as well as site-directed mutagenesis to enhance affinity and stability. Pharmacokinetic optimization strategies, such as PEGylation or fusion to albumin-binding domains [180], could be explored to extend circulation half-life and reduce renal clearance. Finally, integration of the Dual Targeting protein into combination regimens with standard chemotherapy or immune checkpoint inhibitors may reveal synergistic effects and further enhance therapeutic efficacy. Addressing these challenges will be critical for translating this proof-of-concept strategy into a clinically viable therapy and for advancing the development of more selective and effective treatments for pleural mesothelioma.

6 - Conclusions

6 - Conclusions

The work presented in this thesis wants to address two central challenges in the treatment of pleural mesothelioma: the limited availability of effective targeted therapies and the difficulty of selectively modulating key proteolytic pathways involved in tumor progression. ADAM10, a metalloprotease implicated in cell migration, adhesion, shedding, and tumor progression, has emerged as a compelling target in several solid tumors, including PM [69]. However, its essential physiological functions have historically limited therapeutic development, as systemic inhibition may result in significant toxicity [69,220]. In parallel, mesothelin (MSLN) has gained recognition as a tumor-restricted antigen with limited expression in healthy tissues and a strong presence across several malignancies, particularly in epithelioid and biphasic mesothelioma.

This thesis demonstrates that the combination of these two molecular entities: ADAM10 as a target for inhibition and mesothelin as a docking receptor, enables the design of a Dual Targeting therapeutic protein that selectively inhibits ADAM10 activity within the tumor cells. Through biochemical, cellular, and *in vivo* analyses, we provide the first proof-of-concept that coupling the ADAM10 Prodomain with a mesothelin-specific VHH allows localized suppression of ADAM10-mediated processes and yields reduced PM cells migration.

A first major conclusion from this work is that phage display, while a valuable exploratory tool, did not yield short inhibitory peptides with sufficient potency or functional relevance for ADAM10. This justified the strategic transition toward the use of the ADAM10 Prodomain, a biologically validated and evolutionarily optimized natural inhibitor. In a second part of the work, we demonstrated that the recombinant ADAM10 Prodomain is properly folded, functionally active, and able to inhibit endogenous ADAM10 in multiple mesothelioma cell lines. Its capacity to suppress N-cadherin cleavage and reduce cell migration underscores its biological relevance. However, its effects on non-cancerous cells highlight a lack of intrinsic tumor selectivity, thereby reinforcing the need for a targeted delivery mechanism.

In a third part, we established the suitability of the A1 VHH as a targeting module. The VHH exhibited high affinity, folding stability, and no intrinsic cytotoxicity, making it an ideal candidate for tumor-restricted delivery of the ADAM10 Prodomain.

Finally, the engineering and characterization of the Dual Targeting protein represent the central contribution of this thesis. The fusion construct preserved the structural and functional integrity of both domains, selectively inhibited ADAM10 in mesothelin-expressing cells, and demonstrated reduced PM cell migration *in vitro*. Importantly, the Dual Targeting protein reduced tumor volume at 10 mg/kg without systemic toxicity, providing one of the first examples of mesothelin-anchored protease inhibition as a therapeutic modality. Collectively, this work establishes a conceptual and experimental framework for dual-targeted ADAM10 inhibition in pleural mesothelioma. Further studies will be required to optimize pharmacokinetics, assess long-term safety, and evaluate therapeutic efficacy in more advanced preclinical models before clinical translation can be considered.

7 - Annexes

7 - Annexes

7.1 Annex 1

Cytokine	**Cell-to-cell communication**	**Signaling receptor**	**Cell adhesion**	**Cell transport**	**Enzyme**	**Others**
CX3CL1	Betacellulin	CD23	CD44	LRP-1	Klotho	AOO
CX3CL16	C-Met	CD30	CDH-1		MEPRIN Beta	PrP
FAS-L	DLL-1	ErbB2	CDH-2			APLP-2
RANKL	EGF	Notch-1	CDH-5			ITM2b
TNF-α	LAG-3	TSHR	Collagen XVII			
	NG-2	HER2	Desmoglein-2			
	NRG-1	EGFR	Ephrin-A2			
	TREM2	APP	Ephrin-A5			
			L1-CAM			
			NCAM			
			Nectin-1			
			NGL-1			
			PCDHγC3			
			N and E - cadherin			

Table A1. List of the known ADAM10 substrates divided according to their role [82].

7.2 Annex 2

```
from Bio import SeqIO
from Bio.Seq import Seq
import pandas as pd
import numpy as np
import matplotlib.pyplot as plt

def documentRead():
    seqDic = {}
    doc = input("write the file name with the extension")
    for value in SeqIO.parse(doc, "fastq"):
        seqDic[value.description] = value.seq
    return seqDic

def translationMethod(seqs):
  translatedSeq = {}
  num = 0
  for seq in seqs:
        num = num + 1
        print(str(num)+"/"+str(len(seqs)))
        for x in range(3):
            seqTra=seqs[seq][x:].translate()
            name = str(seq)+"+"+str(x+1)
            translatedSeq[name] = seqTra

        seqCompl = seqs[seq].reverse_complement()
        for x in range(3):
            seqTra=seqCompl[x:].translate()
            translatedSeq[name] = seqTra
  return(translatedSeq)

def peptides(translatedSeq):
  foundPeptides = {}
  fwSeq = "LVVPFYSHS"
  RvSeq = "GGGSAETVE"
  empty = "LVVPFYSHSAETVE"

  for singleSeq in translatedSeq:
    posFw = translatedSeq[singleSeq].find(fwSeq)
    posRv = translatedSeq[singleSeq].find(RvSeq)
    if posFw != -1 & posRv != -1:
                                                  foundPeptides[singleSeq]
=  str(translatedSeq[singleSeq][(posFw+(len(fwSeq))):posRv])
    elif translatedSeq[singleSeq].find(empty) != -1:
```

```
      foundPeptides[singleSeq] = "Empty"

  return foundPeptides

class __init__():
    seqs = documentRead()
    translatedSeq = translationMethod(seqs)
    foundPeptides = peptides(translatedSeq)

    data = {
        "Name" : foundPeptides.keys(),
        "Sequences": foundPeptides.values()
    }

    df = pd.DataFrame(data)
    sdf = df.sort_values("Sequences")
    nunique = sdf["Sequences"].nunique()
    count = sdf["Sequences"].count()
    size = sdf["Sequences"].size
    uniqueNumbValue = sdf["Sequences"].value_counts()
     print("The size is ",size," the total count is",count," with the
following unique numbers", nunique )
    print("Unique value numbers", uniqueNumbValue)

    #create plot
    uniqueNumbValue.plot()
    plt.show()

    #create csv files
    sdf.to_csv("RawData.csv")
    uniqueNumbValue.to_csv("Resume.csv")
    print("done")
```

Script 1. Python script to convert all the refined NGS DNA sequences in amino acid sequences and to sort them into an excel file.

8 - Bibliography

8 – Bibliography

1. Batra, H. & Antony, V. B. The pleural mesothelium in development and disease. *Front Physiol* **5**, 284 (2014).

2. Jantz, M. A. & Antony, V. B. Pleural Fibrosis. *Clinics in Chest Medicine* **27**, 181–191 (2006).

3. Hiriart, E., Deepe, R. & Wessels, A. Mesothelium and Malignant Mesothelioma. *J Dev Biol* **7**, 7 (2019).

4. Marinaccio, A. *et al.* Pleural malignant mesothelioma epidemic: Incidence, modalities of asbestos exposure and occupations involved from the Italian National Register. *International Journal of Cancer* **130**, 2146–2154 (2012).

5. Dacic, S. Pleural mesothelioma classification—update and challenges. *Modern Pathology* **35**, 51–56 (2022).

6. Meyerhoff, R. R. *et al.* Impact of mesothelioma histologic subtype on outcomes in the Surveillance, Epidemiology, and End Results database. *J Surg Res* **196**, 23–32 (2015).

7. Montanaro, F. *et al.* Survival of pleural malignant mesothelioma in Italy: A population-based study. *International Journal of Cancer* **124**, 201–207 (2009).

8. Asbestos - Virta - Major Reference Works - Wiley Online Library. https://onlinelibrary.wiley.com/doi/epdf/10.1002/0471238961.0119020510151209.a01.pub3.

9. Kulkova, M. A. *et al.* Asbestos Ceramics from Archaeological Sites of Southern Fennoscandia (Karelia): Mineralogical and Geochemical Aspects. in *Geoarchaeology and Archaeological Mineralogy* (eds Ankusheva, N., Chechushkov, I. V., Stepanov, I., Ankushev, M. & Ankusheva, P.) 233–253 (Springer International Publishing, Cham, 2022). doi:10.1007/978-3-030-86040-0_21.

10. Tulchinsky, T. H. & Varavikova, E. A. Environmental and Occupational Health. *The New Public Health* 471–533 (2014) doi:10.1016/B978-0-12-415766-8.00009-4.

11. Paolini, V. *et al.* Asbestos treatment technologies. *J Mater Cycles Waste Manag* **21**, 205–226 (2019).

12. Mineral Commodity Summaries 2024.

13. Hajj, G. N. M. *et al.* Malignant pleural mesothelioma: an update. *J Bras Pneumol* **47**, e20210129.

14. Pairon, J.-C. *et al.* Pleural Plaques and the Risk of Pleural Mesothelioma. *J Natl Cancer Inst* **105**, 293–301 (2013).

15. NEB Phage Display Manual.

16. Olsen, N. J. *et al.* Increasing incidence of malignant mesothelioma after exposure to asbestos during home maintenance and renovation. *Medical Journal of Australia* **195**, 271–274 (2011).

17. Brims, F. Epidemiology and Clinical Aspects of Malignant Pleural Mesothelioma. *Cancers (Basel)* **13**, 4194 (2021).

18. Cavone, D. *et al.* Epidemiology of Mesothelioma. *Environments* **6**, 76 (2019).

19. Mott, F. E. Mesothelioma: A Review. *Ochsner J* **12**, 70–79 (2012).

20. Marinaccio, A. *et al.* The epidemiology of malignant mesothelioma in women: gender differences and modalities of asbestos exposure. *Occup Environ Med* **75**, 254–262 (2018).

21. Alpert, N., Gerwen, M. van & Taioli, E. Epidemiology of mesothelioma in the 21st century in Europe and the United States, 40 years after restricted/banned asbestos use. *Translational Lung Cancer Research* **9**, (2020).

22. Van den Borre, L. & Deboosere, P. Asbestos in Belgium: an underestimated health risk. The evolution of mesothelioma mortality rates (1969–2009). *Int J Occup Environ Health* **20**, 134–140 (2014).

23. Carel, R. *et al.* Occupational exposure to asbestos and man-made vitreous fibres and risk of lung cancer: a multicentre case-control study in Europe. *Occup Environ Med* **64**, 502–508 (2007).

24. Carbone, M., Minaai, M., Takinishi, Y., Pagano, I. & Yang, H. Preventive and therapeutic opportunities: targeting BAP1 and/or HMGB1 pathways to diminish the burden of mesothelioma. *J Transl Med* **21**, 749 (2023).

25. Carbone, M. *et al.* Mesothelioma: Scientific clues for prevention, diagnosis, and therapy. *CA: A Cancer Journal for Clinicians* **69**, 402–429 (2019).

26. Larson, D. *et al.* Investigating palygorskite's role in the development of mesothelioma in southern Nevada: Insights into fiber-induced carcinogenicity. *Journal of Toxicology and Environmental Health, Part B* **19**, 213–230 (2016).

27. Zhong, Y.-F. *et al.* HMGB1 as a Key Mediator in Malignant Mesothelioma and a Potential Target for Asbestos-Related Cancer Therapy. *Toxics* **13**, 448 (2025).

28. Ito, F. *et al.* Asbestos conceives Fe(II)-dependent mutagenic stromal milieu through ceaseless macrophage ferroptosis and β-catenin induction in mesothelium. *Redox Biol* **36**, 101616 (2020).

29. Cedres, S. *et al.* BAP1 Mutations and Pleural Mesothelioma: Genetic Insights, Clinical Implications, and Therapeutic Perspectives. *Cancers* **17**, 1581 (2025).

30. Vilchez, R. A. & Butel, J. S. Emergent Human Pathogen Simian Virus 40 and Its Role in Cancer. *Clin Microbiol Rev* **17**, 495–508 (2004).

31. Jain, S. L. The WetNet: What the Oral Polio Vaccine Hypothesis Exposes about Globalized Interspecies Fluid Bonds. *Medical Anthropology Quarterly* **34**, 504–524 (2020).

32. Sahu, R. K. *et al.* Malignant mesothelioma tumours: molecular pathogenesis, diagnosis, and therapies accompanying clinical studies. *Front Oncol* **13**, 1204722 (2023).

33. Peterson Jr., J. T., Greenberg, S. D. & Buffler, P. A. Non-asbestos-related malignant mesothelioma. A review. *Cancer* **54**, 951–960 (1984).

34. Radiation-induced mesothelioma among long-term solid cancer survivors: a longitudinal analysis of SEER database - Farioli - 2016 - Cancer Medicine - Wiley Online Library. https://onlinelibrary.wiley.com/doi/10.1002/cam4.656.

35. Churg, A. *et al.* Malignant mesothelioma in situ. *Histopathology* **72**, 1033–1038 (2018).

36. Churg, A. *et al.* Malignant mesothelioma in situ: morphologic features and clinical outcome. *Modern Pathology* **33**, 297–302 (2020).

37. Brcic, L. & Kern, I. Clinical significance of histologic subtyping of malignant pleural mesothelioma. *Transl Lung Cancer Res* **9**, 924–933 (2020).

38. Kadota, K. *et al.* Pleomorphic epithelioid diffuse malignant pleural mesothelioma: a clinicopathological review and conceptual proposal to reclassify as biphasic or sarcomatoid mesothelioma. *J Thorac Oncol* **6**, 896–904 (2011).

39. Nicholson, A. G. *et al.* EURACAN/IASLC Proposals for Updating the Histologic Classification of Pleural Mesothelioma: Towards a More Multidisciplinary Approach. *Journal of Thoracic Oncology* **15**, 29–49 (2020).

40. Mesothelioma Stages | Mesothelioma Metastasis. https://www.cancer.org/cancer/types/malignant-mesothelioma/detection-diagnosis-staging/staging.html.

41. Yonar - 1868 - Rapid diagnosis of malignant pleural mesothelioma .pdf.

42. Bianco, A., Valente, T., De Rimini, M. L., Sica, G. & Fiorelli, A. Clinical diagnosis of malignant pleural mesothelioma. *J Thorac Dis* **10**, S253–S261 (2018).

43. Karasalih, B., Duman, H., Bechelany, M. & Karav, S. Osteopontin: Its Properties, Recent Studies, and Potential Applications. *Int J Mol Sci* **26**, 5868 (2025).

44. Hollevoet, K. *et al.* Serum Mesothelin for Diagnosing Malignant Pleural Mesothelioma: An Individual Patient Data Meta-Analysis. *J Clin Oncol* **30**, 1541–1549 (2012).

45. Ohashi, R. *et al.* Osteopontin Modulates Malignant Pleural Mesothelioma Cell Functions in Vitro. *JJLC* **49**, 368–375 (2009).

46. Berr, A. L. *et al.* Vimentin is required for tumor progression and metastasis in a mouse model of non–small cell lung cancer. *Oncogene* **42**, 2074–2087 (2023).

47. Janes, S. M., Alrifai, D. & Fennell, D. A. Perspectives on the Treatment of Malignant Pleural Mesothelioma. *New England Journal of Medicine* **385**, 1207–1218 (2021).

48. Baas, P. *et al.* First-line nivolumab plus ipilimumab in unresectable malignant pleural mesothelioma (CheckMate 743): a multicentre, randomised, open-label, phase 3 trial. *The Lancet* **397**, 375–386 (2021).

49. Clive, A. O. *et al.* Prophylactic radiotherapy for the prevention of procedure-tract metastases after surgical and large-bore pleural procedures in malignant pleural mesothelioma (SMART): a multicentre, open-label, phase 3, randomised controlled trial. *Lancet Oncol* **17**, 1094–1104 (2016).

50. Waite, K. & Gilligan, D. The Role of Radiotherapy in the Treatment of Malignant Pleural Mesothelioma. *Clinical Oncology* **19**, 182–187 (2007).

51. Gelzinis, T. A. The 2019 ERS/ESTS/EACTS/ESTRO Guidelines on the Management of Patients With Malignant Pleural Mesothelioma. *Journal of Cardiothoracic and Vascular Anesthesia* **35**, 378–388 (2021).

52. Tsao, A. S., Pass, H. I., Rimner, A. & Mansfield, A. S. New Era for Malignant Pleural Mesothelioma: Updates on Therapeutic Options. *J Clin Oncol* **40**, 681–692 (2022).

53. Vogelzang, N. J. *et al.* Phase III study of pemetrexed in combination with cisplatin versus cisplatin alone in patients with malignant pleural mesothelioma. *J Clin Oncol* **21**, 2636–2644 (2003).

54. Riddell, I. A. Cisplatin and Oxaliplatin: Our Current Understanding of Their Actions. *Met Ions Life Sci* **18**, /books/9783110470734/9783110470734-007/9783110470734-007.xml (2018).

55. Adjei, A. A. Pharmacology and Mechanism of Action of Pemetrexed. *Clinical Lung Cancer* **5**, S51–S55 (2004).

56. van Meerbeeck, J. P. *et al.* Randomized phase III study of cisplatin with or without raltitrexed in patients with malignant pleural mesothelioma: an intergroup study of the European Organisation for Research and Treatment of Cancer Lung Cancer Group and the National Cancer Institute of Canada. *J Clin Oncol* **23**, 6881–6889 (2005).

57. Ellis, L. M. Mechanisms of Action of Bevacizumab as a Component of Therapy for Metastatic Colorectal Cancer. *Seminars in Oncology* **33**, S1–S7 (2006).

58. Zalcman, G. *et al.* Bevacizumab for newly diagnosed pleural mesothelioma in the Mesothelioma Avastin Cisplatin Pemetrexed Study (MAPS): a randomised, controlled, open-label, phase 3 trial. *Lancet* **387**, 1405–1414 (2016).

59. Grosso, F. *et al.* Nintedanib Plus Pemetrexed/Cisplatin in Patients With Malignant Pleural Mesothelioma: Phase II Results From the Randomized, Placebo-Controlled LUME-Meso Trial. *J Clin Oncol* **35**, 3591–3600 (2017).

60. Tsao, A. S. *et al.* Phase II Trial of Cediranib in Combination With Cisplatin and Pemetrexed in Chemotherapy-Naïve Patients With Unresectable Malignant Pleural Mesothelioma (SWOG S0905). *J Clin Oncol* **37**, 2537–2547 (2019).

61. Ledermann, J. A. *et al.* Cediranib in addition to chemotherapy for women with relapsed platinum-sensitive ovarian cancer (ICON6): overall survival results of a phase III randomised trial. *ESMO Open* **6**, 100043 (2021).

62. Ameri, P. *et al.* Cardiovascular safety of the tyrosine kinase inhibitor nintedanib. *British Journal of Clinical Pharmacology* **87**, 3690–3698 (2021).

63. Matulonis, U. A. *et al.* Cediranib, an Oral Inhibitor of Vascular Endothelial Growth Factor Receptor Kinases, Is an Active Drug in Recurrent Epithelial Ovarian, Fallopian Tube, and Peritoneal Cancer. *J Clin Oncol* **27**, 5601–5606 (2009).

64. Podolanczuk, A. J. & Cottin, V. A Narrative Review of Real-World Data on the Safety of Nintedanib in Patients with Idiopathic Pulmonary Fibrosis. *Adv Ther* **40**, 2038–2050 (2023).

65. Buchbinder, E. I. & Desai, A. CTLA-4 and PD-1 Pathways. *Am J Clin Oncol* **39**, 98–106 (2016).

66. Sépult, C. *et al.* ADAM10 mediates malignant pleural mesothelioma invasiveness. *Oncogene* **38**, 3521–3534 (2019).

67. ADAM, a novel family of membrane proteins containing A Disintegrin And Metalloprotease domain: multipotential functions in cell-cell and cell-matrix interactions. | Journal of Cell Biology | Rockefeller University Press. https://rupress.org/jcb/article/131/2/275/20898/ADAM-a-novel-family-of-membrane-proteins.

68. Edwards, D. R., Handsley, M. M. & Pennington, C. J. The ADAM metalloproteinases. *Mol Aspects Med* **29**, 258–289 (2008).

69. Smith, T. M., Tharakan, A. & Martin, R. K. Targeting ADAM10 in Cancer and Autoimmunity. *Front Immunol* **11**, 499 (2020).

70. Huxley-Jones, J. *et al.* The evolution of the vertebrate metzincins; insights from Ciona intestinalis and Danio rerio. *BMC Evol Biol* **7**, 63 (2007).

71. Puente, X. S. & López-Otín, C. A genomic analysis of rat proteases and protease inhibitors. *Genome Res* **14**, 609–622 (2004).

72. Rawlings, N. D., Morton, F. R., Kok, C. Y., Kong, J. & Barrett, A. J. MEROPS: the peptidase database. *Nucleic Acids Res* **36**, D320-325 (2008).

73. Moss, M. L. *et al.* The ADAM10 Prodomain Is a Specific Inhibitor of ADAM10 Proteolytic Activity and Inhibits Cellular Shedding Events*. *Journal of Biological Chemistry* **282**, 35712–35721 (2007).

74. Lum, L., Reid, M. S. & Blobel, C. P. Intracellular maturation of the mouse metalloprotease disintegrin MDC15. *J Biol Chem* **273**, 26236–26247 (1998).

75. Howard, L., Maciewicz, R. A. & Blobel, C. P. Cloning and characterization of ADAM28: evidence for autocatalytic pro-domain removal and for cell surface localization of mature ADAM28. *Biochem J* **348 Pt 1**, 21–27 (2000).

76. Seegar, T. C. M. *et al.* Structural Basis for Regulated Proteolysis by the α-Secretase ADAM10. *Cell* **171**, 1638-1648.e7 (2017).

77. Janes, P. W. *et al.* Adam meets Eph: an ADAM substrate recognition module acts as a molecular switch for ephrin cleavage in trans. *Cell* **123**, 291–304 (2005).

78. Caescu, C. I., Jeschke, G. R. & Turk, B. E. Active-site determinants of substrate recognition by the metalloproteinases TACE and ADAM10. *Biochem J* **424**, 79–88 (2009).

79. Pan, D. & Rubin, G. M. Kuzbanian Controls Proteolytic Processing of Notch and Mediates Lateral Inhibition during Drosophila and Vertebrate Neurogenesis. *Cell* **90**, 271–280 (1997).

80. Mitsiadis, T. A. *et al.* Adam10-dependent Notch signaling establishes dental epithelial cell boundaries required for enamel formation. *iScience* **25**, 105154 (2022).

81. Jorissen, E. *et al.* The Disintegrin/Metalloproteinase ADAM10 Is Essential for the Establishment of the Brain Cortex. *J Neurosci* **30**, 4833–4844 (2010).

82. Cuffaro, D. *et al.* A disintegrin and metalloproteinases (ADAMs) and tumor necrosis factor-alpha-converting enzyme (TACE). in *Metalloenzymes* 207–237 (Elsevier, 2024). doi:10.1016/B978-0-12-823974-2.00016-4.

83. Saftig, P. & Lichtenthaler, S. F. The alpha secretase ADAM10: A metalloprotease with multiple functions in the brain. *Prog Neurobiol* **135**, 1–20 (2015).

84. Altmeppen, H. C. *et al.* The sheddase ADAM10 is a potent modulator of prion disease. *eLife* **4**, e04260.

85. McInnes, I. B. & Schett, G. The Pathogenesis of Rheumatoid Arthritis. *New England Journal of Medicine* **365**, 2205–2219 (2011).

86. Murray, H. E. *et al.* A 12-month treatment of severe psoriasis with acitretin: results of a Canadian open multicenter study. *J Am Acad Dermatol* **24**, 598–602 (1991).

87. Kohutek, Z. A., diPierro, C. G., Redpath, G. T. & Hussaini, I. M. ADAM-10-Mediated N-Cadherin Cleavage Is Protein Kinase C-α Dependent and Promotes Glioblastoma Cell Migration. *J Neurosci* **29**, 4605–4615 (2009).

88. Liu, R. *et al.* Glioblastoma recurrence correlates with NLGN3 levels. *Cancer Medicine* **7**, 2848–2859 (2018).

89. Liu, W. *et al.* A novel pan-cancer biomarker plasma heat shock protein 90alpha and its diagnosis determinants in clinic. *Cancer Sci* **110**, 2941–2959 (2019).

90. ADAM10 Is a Potential Novel Prognostic Biomarker for Sacral Chordoma. https://www.annclinlabsci.org/content/49/3/309.long.

91. Yoneyama, T. *et al.* ADAM10 Sheddase Activity is a Potential Lung-Cancer Biomarker. *J Cancer* **9**, 2559–2570 (2018).

92. Baker, J. H. E. *et al.* Heterogeneous distribution of trastuzumab in HER2-positive xenografts and metastases: role of the tumor microenvironment. *Clin Exp Metastasis* **35**, 691–705 (2018).

93. Feldinger, K. *et al.* ADAM10 mediates trastuzumab resistance and is correlated with survival in HER2 positive breast cancer. *Oncotarget* **5**, 6633–6646 (2014).

94. Mullooly, M. *et al.* ADAM10: a new player in breast cancer progression? *Br J Cancer* **113**, 945–951 (2015).

95. Romero, Y., Wise, R. & Zolkiewska, A. Proteolytic processing of PD-L1 by ADAM proteases in breast cancer cells. *Cancer Immunol Immunother* **69**, 43–55 (2019).

96. Soundararajan, R., Sayat, R., Robertson, G. S. & Marignani, P. A. Triptolide: An inhibitor of a disintegrin and metalloproteinase 10 (ADAM10) in cancer cells. *cbt* **8**, 2054–2062 (2009).

97. Mahasenan, K. V. *et al.* In Search of Selectivity in Inhibition of ADAM10. *ACS Med Chem Lett* **9**, 708–713 (2018).

98. Pluda, S., Mazzocato, Y. & Angelini, A. Peptide-Based Inhibitors of ADAM and ADAMTS Metalloproteinases. *Front Mol Biosci* **8**, 703715 (2021).

99. Hu, J., Fiten, P., Van den Steen, P. E., Chaltin, P. & Opdenakker, G. Simulation of Evolution-Selected Propeptide by High-Throughput Selection of a Peptidomimetic Inhibitor on a Capillary DNA Sequencer Platform. *Anal. Chem.* **77**, 2116–2124 (2005).

100. Jozic, D. *et al.* X-ray Structure of Human proMMP-1: NEW INSIGHTS INTO PROCOLLAGENASE ACTIVATION AND COLLAGEN BINDING *. *Journal of Biological Chemistry* **280**, 9578–9585 (2005).

101. Morgunova, E. *et al.* Structure of human pro-matrix metalloproteinase-2: activation mechanism revealed. *Science* **284**, 1667–1670 (1999).

102. Bazan, J., Całkosiński, I. & Gamian, A. Phage display—A powerful technique for immunotherapy. *Hum Vaccin Immunother* **8**, 1817–1828 (2012).

103. Sergeeva, A., Kolonin, M. G., Molldrem, J. J., Pasqualini, R. & Arap, W. Display technologies: Application for the discovery of drug and gene delivery agents. *Adv Drug Deliv Rev* **58**, 1622–1654 (2006).

104. Vujadinovic, M. & Vellinga, J. Progress in Adenoviral Capsid-Display Vaccines. *Biomedicines* **6**, 81 (2018).

105. Daugherty, P. S. Protein engineering with bacterial display. *Current Opinion in Structural Biology* **17**, 474–480 (2007).

106. Kim, Y.-S., Jung, H.-C. & Pan, J.-G. Bacterial Cell Surface Display of an Enzyme Library for Selective Screening of Improved Cellulase Variants. *Applied and Environmental Microbiology* **66**, 788–793 (2000).

107. Kenrick, S. A. & Daugherty, P. S. Bacterial display enables efficient and quantitative peptide affinity maturation. *Protein Eng Des Sel* **23**, 9–17 (2010).

108. Jaroszewicz, W., Morcinek-Orłowska, J., Pierzynowska, K., Gaffke, L. & Węgrzyn, G. Phage display and other peptide display technologies. *FEMS Microbiology Reviews* **46**, fuab052 (2022).

109. Ho, M. & Pastan, I. Display and selection of scFv antibodies on HEK-293T cells. *Methods Mol Biol* **562**, 99–113 (2009).

110. Amstutz, P., Forrer, P., Zahnd, C. & Plückthun, A. In vitro display technologies: novel developments and applications. *Current Opinion in Biotechnology* **12**, 400–405 (2001).

111. Zimmermann, I. *et al.* Generation of synthetic nanobodies against delicate proteins. *Nat Protoc* **15**, 1707–1741 (2020).

112. Cong, C. *et al.* Cell-free ribosome display and selection of antibodies on arrayed antigens. *PROTEOMICS* **16**, 1291–1296 (2016).

113. Newton, M. S., Cabezas, Y. & Seelig, B. Advantages of mRNA display. *ACS Synth Biol* **9**, 181–190 (2020).

114. Ledsgaard, L., Kilstrup, M., Karatt-Vellatt, A., McCafferty, J. & Laustsen, A. H. Basics of Antibody Phage Display Technology. *Toxins (Basel)* **10**, 236 (2018).

115. Rasched, I. & Oberer, E. Ff coliphages: structural and functional relationships. *Microbiol Rev* **50**, 401–427 (1986).

116. Berkowitz, S. A. & Day, L. A. Mass, length, composition and structure of the filamentous bacterial virus fd. *Journal of Molecular Biology* **102**, 531–547 (1976).

117. Lubkowski, J., Hennecke, F., Plückthun, A. & Wlodawer, A. The structural basis of phage display elucidated by the crystal structure of the N-terminal domains of g3p. *Nat Struct Mol Biol* **5**, 140–147 (1998).

118. Pellegri, C., Moreau, A., Duché, D. & Houot, L. Direct interaction between fd phage pilot protein pIII and the TolQ–TolR proton-dependent motor provides new insights into the import of filamentous phages. *J Biol Chem* **299**, 105048 (2023).

119. Filamentous Fusion Phage: Novel Expression Vectors That Display Cloned Antigens on the Virion Surface | Science. https://www.science.org/doi/10.1126/science.4001944?url_ver=Z39.88-2003&rfr_id=ori:rid:crossref.org&rfr_dat=cr_pub%20%200pubmed.

120. Phage antibodies: filamentous phage displaying antibody variable domains | Nature. https://www.nature.com/articles/348552a0.

121. Løset, G. Å. & Sandlie, I. Next generation phage display by use of pVII and pIX as display scaffolds. *Methods* **58**, 40–46 (2012).

122. Advancement and applications of peptide phage display technology in biomedical science | Journal of Biomedical Science | Full Text. https://jbiomedsci.biomedcentral.com/articles/10.1186/s12929-016-0223-x.

123. Stanger, K. *et al.* Allosteric peptides bind a caspase zymogen and mediate caspase tetramerization. *Nat Chem Biol* **8**, 655–660 (2012).

124. Jaye, D. L. *et al.* Use of Real-Time Polymerase Chain Reaction to Identify Cell- and Tissue-Type-Selective Peptides by Phage Display. *Am J Pathol* **162**, 1419–1429 (2003).

125. Mullen, L. M., Nair, S. P., Ward, J. M., Rycroft, A. N. & Henderson, B. Phage display in the study of infectious diseases. *Trends Microbiol* **14**, 141–147 (2006).

126. Ph.D. Phage Display Libraries, E8100, E8101, E8110, E8111, E8120.

127. Peptide Ligands to Human Immunodeficiency Virus Type 1 gp120 Identified from Phage Display Libraries | Journal of Virology. https://journals.asm.org/doi/10.1128/jvi.73.7.5795-5802.1999.

128. Rajik, M. *et al.* Identification and characterisation of a novel anti-viral peptide against avian influenza virus H9N2. *Virology Journal* **6**, 74 (2009).

129. Selection of peptides with semiconductor binding specificity for directed nanocrystal assembly | Nature. https://www.nature.com/articles/35015043.

130. Sawada, T., Takahashi, T. & Mihara, H. Affinity-Based Screening of Peptides Recognizing Assembly States of Self-Assembling Peptide Nanomaterials. *J. Am. Chem. Soc.* **131**, 14434–14441 (2009).

131. Chang, K., Pastan, I. & Willingham, M. C. Isolation and characterization of a monoclonal antibody, K1, reactive with ovarian cancers and normal mesothelium. *International Journal of Cancer* **50**, 373–381 (1992).

132. Chang, K., Pastan, I. & Willngham, M. C. Frequent expression of the tumor antigen cak1 in squamous-cell carcinomas. *International Journal of Cancer* **51**, 548–554 (1992).

133. Hagerty, B. L. & Takabe, K. Biology of Mesothelin and Clinical Implications: A Review of Existing Literature. *World J Oncol* **14**, 340–349 (2023).

134. Cristaudo, A. *et al.* Two Novel Polymorphisms in 5' Flanking Region of the Mesothelin Gene are Associated with Soluble Mesothelin-Related Peptide (SMRP) Levels. *Int J Biol Markers* **26**, 117–123 (2011).

135. Faust, J. R., Hamill, D., Kolb, E. A., Gopalakrishnapillai, A. & Barwe, S. P. Mesothelin: An Immunotherapeutic Target beyond Solid Tumors. *Cancers (Basel)* **14**, 1550 (2022).

136. Liu, X., Chan, A., Tai, C.-H., Andresson, T. & Pastan, I. Multiple proteases are involved in mesothelin shedding by cancer cells. *Commun Biol* **3**, 728 (2020).

137. Ma, J., Tang, W. K., Esser, L., Pastan, I. & Xia, D. Recognition of Mesothelin by the Therapeutic Antibody MORAb-009. *J Biol Chem* **287**, 33123–33131 (2012).

138. Chang, K. & Pastan, I. Molecular cloning of mesothelin, a differentiation antigen present on mesothelium, mesotheliomas, and ovarian cancers. *Proc Natl Acad Sci U S A* **93**, 136–140 (1996).

139. Zhan, J. *et al.* Structures of Cancer Antigen Mesothelin and Its Complexes with Therapeutic Antibodies. *Cancer Research Communications* **3**, 175–191 (2023).

140. Kobe, B. *et al.* Turn up the HEAT. *Structure* **7**, R91–R97 (1999).

141. Muminova, Z. E., Strong, T. V. & Shaw, D. R. Characterization of human mesothelin transcripts in ovarian and pancreatic cancer. *BMC Cancer* **4**, 19 (2004).

142. Bera, T. K. & Pastan, I. Mesothelin Is Not Required for Normal Mouse Development or Reproduction. *Mol Cell Biol* **20**, 2902–2906 (2000).

143. Shen, J., Sun, X. & Zhou, J. Insights Into the Role of Mesothelin as a Diagnostic and Therapeutic Target in Ovarian Carcinoma. *Front Oncol* **10**, 1263 (2020).

144. Ledda, C., Loreto, C., Lombardo, C., Cardile, V. & Rapisarda, V. Mesothelin methylation, soluble mesothelin related protein levels and inflammation profiling in workers chronically exposed to naturally occurring asbestos fibers. *Transl Oncol* **40**, 101872 (2024).

145. Zhang, X.-Y., Hong, L.-L. & Ling, Z. MUC16: clinical targets with great potential. *Clin Exp Med* **24**, 101 (2024).

146. Kaneko, O. *et al.* A Binding Domain on Mesothelin for CA125/MUC16. *J Biol Chem* **284**, 3739–3749 (2009).

147. Huo, Q. *et al.* Free CA125 promotes ovarian cancer cell migration and tumor metastasis by binding Mesothelin to reduce DKK1 expression and activate the SGK3/FOXO3 pathway. *Int J Biol Sci* **17**, 574–588 (2021).

148. Egeblad, M. & Werb, Z. New functions for the matrix metalloproteinases in cancer progression. *Nat Rev Cancer* **2**, 161–174 (2002).

149. Bharadwaj, U., Li, M., Chen, C. & Yao, Q. Mesothelin-Induced Pancreatic Cancer Cell Proliferation Involves Alteration of Cyclin E via Activation of Stat3. *Mol Cancer Res* **6**, 1755–1765 (2008).

150. Silvestri, R., Colucci, E., Piccardi, M., Landi, S. & Gemignani, F. Decoding the role of mesothelin in tumor dynamics and targeted treatment innovations. *Mol Biomed* **6**, 131 (2025).

151. Jin, S., Zhou, F., Katirai, F. & Li, P.-L. Lipid Raft Redox Signaling: Molecular Mechanisms in Health and Disease. *Antioxid Redox Signal* **15**, 1043–1083 (2011).

152. Anselmo, S. *et al.* Lipid Rafts in Signalling, Diseases, and Infections: What Can Be Learned from Fluorescence Techniques? *Membranes* **15**, 6 (2025).

153. Paulick, M. G. & Bertozzi, C. R. The Glycosylphosphatidylinositol Anchor: A Complex Membrane-Anchoring Structure for Proteins. *Biochemistry* **47**, 6991–7000 (2008).

154. Kumari, S. Mesothelin as a Signal Pathways and Epigenetic Target in Cancer Therapy. *Cancers* **17**, 1118 (2025).

155. Cao, L. *et al.* Megakaryocyte Potentiating Factor as a Predictive Biomarker for Therapies Against Malignant Mesothelioma. *JCO Precis Oncol* **2**, PO.17.00282 (2018).

156. Michalska, M. & Wolf, P. Pseudomonas Exotoxin A: optimized by evolution for effective killing. *Front Microbiol* **6**, 963 (2015).

157. Hassan, R. *et al.* Phase I Study of the Immunotoxin LMB-100 in Patients with Mesothelioma and Other Solid Tumors Expressing Mesothelin. *Cancer* **126**, 4936–4947 (2020).

158. Villena-Vargas, J. & Adusumilli, P. S. Mesothelin-targeted immunotherapies for malignant pleural mesothelioma. *Annals of Cardiothoracic Surgery* **1**, 46671–46471 (2012).

159. Hassan, R. *et al.* Clinical Response of Live-Attenuated, Listeria monocytogenes Expressing Mesothelin (CRS-207) with Chemotherapy in Patients with Malignant Pleural Mesothelioma. *Clin Cancer Res* **25**, 5787–5798 (2019).

160. Le, D. T. *et al.* A Live-attenuated Listeria Vaccine (ANZ-100) and a Live-attenuated Listeria Vaccine Expressing Mesothelin (CRS-207) for Advanced Cancers: Phase 1 Studies of Safety and Immune Induction. *Clin Cancer Res* **18**, 858–868 (2012).

161. Santin, A. D. *et al.* Safety and activity of anti-mesothelin antibody–drug conjugate anetumab ravtansine in combination with pegylated-liposomal doxorubicin in platinum-resistant ovarian cancer: multicenter, phase Ib dose escalation and expansion study. *Int J Gynecol Cancer* **33**, 562–570 (2023).

162. Zhang, Y., Xiang, L., Hassan, R. & Pastan, I. Immunotoxin and Taxol synergy results from a decrease in shed mesothelin levels in the extracellular space of tumors. *Proc Natl Acad Sci U S A* **104**, 17099–17104 (2007).

163. Robinson, B. W. *et al.* Mesothelin-family proteins and diagnosis of mesothelioma. *The Lancet* **362**, 1612–1616 (2003).

164. Pantazopoulos, I., Boura, P., Xanthos, T. & Syrigos, K. Effectiveness of mesothelin family proteins and osteopontin for malignant mesothelioma. *European Respiratory Journal* **41**, 706–715 (2013).

165. Zhang, Q., Zhang, N., Xiao, H., Wang, C. & He, L. Small Antibodies with Big Applications: Nanobody-Based Cancer Diagnostics and Therapeutics. *Cancers (Basel)* **15**, 5639 (2023).

166. Jin, B., Odongo, S., Radwanska, M. & Magez, S. NANOBODIES®: A Review of Generation, Diagnostics and Therapeutics. *Int J Mol Sci* **24**, 5994 (2023).

167. Muyldermans, S. Nanobodies: Natural Single-Domain Antibodies. *Annu. Rev. Biochem.* **82**, 775–797 (2013).

168. Khalaf, H.-E., Al-Bouqaee, H., Hwijeh, M. & Abbady, A. Q. Characterization of rabbit polyclonal antibody against camel recombinant nanobodies. *Open Life Sci* **17**, 659–675 (2022).

169. Morrison, S. L. Murine heavy chain disease. *European Journal of Immunology* **8**, 194–199 (1978).

170. Alexander, A. *et al.* gamma Heavy chain disease in man: cDNA sequence supports partial gene deletion model. *Proc Natl Acad Sci U S A* **79**, 3260–3264 (1982).

171. Khalid, Z. *et al.* IgNAR antibody: Structural features, diversity and applications. *Fish & Shellfish Immunology* **121**, 467–477 (2022).

172. Hamers-Casterman, C. *et al.* Naturally occurring antibodies devoid of light chains. *Nature* **363**, 446–448 (1993).

173. Erasmus, M. F. *et al.* Developing drug-like single-domain antibodies (VHH) from in vitro libraries. *mAbs* **17**, 2516676 (2025).

174. Asaadi, Y., Jouneghani, F. F., Janani, S. & Rahbarizadeh, F. A comprehensive comparison between camelid nanobodies and single chain variable fragments. *Biomark Res* **9**, 87 (2021).

175. Fernández-Quintero, M. L. *et al.* On the humanization of VHHs: Prospective case studies, experimental and computational characterization of structural determinants for functionality. *Protein Sci* **33**, e5176 (2024).

176. De Genst, E. *et al.* Molecular basis for the preferential cleft recognition by dromedary heavy-chain antibodies. *Proc Natl Acad Sci U S A* **103**, 4586–4591 (2006).

177. Zhang, L. *et al.* Comparative analysis of CDR3 length-dependent patterns in VHHs. *Front Immunol* **16**, 1647230 (2025).

178. Arbabi Ghahroudi, M., Desmyter, A., Wyns, L., Hamers, R. & Muyldermans, S. Selection and identification of single domain antibody fragments from camel heavy-chain antibodies. *FEBS Letters* **414**, 521–526 (1997).

179. Pharmacokinetics of Single Domain Antibodies and Conjugated Nanoparticles Using a Hybrid near Infrared Method. https://www.mdpi.com/1422-0067/22/16/8695.

180. Rashidian, M. *et al.* Enzyme-Mediated Modification of Single-Domain Antibodies for Imaging Modalities with Different Characteristics. *Angew Chem Int Ed Engl* **55**, 528–533 (2016).

181. van Faassen, H. *et al.* Serum albumin-binding VHHs with variable pH sensitivities enable tailored half-life extension of biologics. *The FASEB Journal* **34**, 8155–8171 (2020).

182. Muyldermans, S. A guide to: generation and design of nanobodies. *FEBS J* **288**, 2084–2102 (2021).

183. Janssens, R. *et al.* Generation of heavy-chain-only antibodies in mice. *Proceedings of the National Academy of Sciences* **103**, 15130–15135 (2006).

184. Sabir, J. S. M. *et al.* Construction of naïve camelids VHH repertoire in phage display-based library. *Comptes Rendus Biologies* **337**, 244–249 (2014).

185. Verheesen, P. *et al.* Reliable and controllable antibody fragment selections from Camelid non-immune libraries for target validation. *Biochimica et Biophysica Acta (BBA) - Proteins and Proteomics* **1764**, 1307–1319 (2006).

186. Sevy, A. M. *et al.* Structure- and sequence-based design of synthetic single-domain antibody libraries. *Protein Eng Des Sel* **33**, gzaa028 (2020).

187. Sandin, S., Öfverstedt, L.-G., Wikström, A.-C., Wrange, Ö. & Skoglund, U. Structure and Flexibility of Individual Immunoglobulin G Molecules in Solution. *Structure* **12**, 409–415 (2004).

188. Murakami, T. *et al.* Construction of a Humanized Artificial VHH Library Reproducing Structural Features of Camelid VHHs for Therapeutics. *Antibodies (Basel)* **11**, 10 (2022).

189. Duggan, S. Caplacizumab: First Global Approval. *Drugs* **78**, 1639–1642 (2018).

190. Hegi-Johnson, F. *et al.* Imaging immunity in patients with cancer using positron emission tomography. *NPJ Precis Oncol* **6**, 24 (2022).

191. Berland, L. *et al.* Nanobodies for Medical Imaging: About Ready for Prime Time? *Biomolecules* **11**, 637 (2021).

192. Castano, A. P., Mroz, P. & Hamblin, M. R. Photodynamic therapy and anti-tumour immunity. *Nat Rev Cancer* **6**, 535–545 (2006).

193. Larson, S. M., Carrasquillo, J. A., Cheung, N.-K. V. & Press, O. Radioimmunotherapy of human tumours. *Nat Rev Cancer* **15**, 347–360 (2015).

194. Jin, R. *et al.* Dual Mechanisms of Novel CD73-Targeted Antibody and Antibody–Drug Conjugate in Inhibiting Lung Tumor Growth and Promoting Antitumor Immune-Effector Function. *Molecular Cancer Therapeutics* **19**, 2340–2352 (2020).

195. Dual HER2 Targeting with Trastuzumab and Liposomal-Encapsulated Doxorubicin (MM-302) Demonstrates Synergistic Antitumor Activity in Breast and Gastric Cancer | Cancer Research | American Association for Cancer Research. https://aacrjournals.org/cancerres/article/76/6/1517/616186/Dual-HER2-Targeting-with-Trastuzumab-and-Liposomal.

196. Deng, C. *et al.* Novel recombinant immunotoxin of EGFR specific nanobody fused with cucurmosin, construction and antitumor efficiency in vitro. *Oncotarget* **8**, 38568–38580 (2017).

197. Behdani, M. *et al.* Development of VEGFR2-specific Nanobody Pseudomonas exotoxin A conjugated to provide efficient inhibition of tumor cell growth. *N Biotechnol* **30**, 205–209 (2013).

198. Beig Parikhani, A. *et al.* A novel nanobody-based immunocytokine of a mutant interleukin-2 as a potential cancer therapeutic. *AMB Express* **14**, 19 (2024).

199. Nanobodies and their derivatives: pioneering the future of cancer immunotherapy | Cell Communication and Signaling | Full Text. https://biosignaling.biomedcentral.com/articles/10.1186/s12964-025-02270-4.

200. Nanobody–Antigen Conjugates Elicit HPV-Specific Antitumor Immune Responses | Cancer Immunology Research | American Association for Cancer Research. https://aacrjournals.org/cancerimmunolres/article/6/7/870/468909/Nanobody-Antigen-Conjugates-Elicit-HPV-Specific.

201. Campuzano, S. *et al.* Disposable amperometric magnetoimmunosensors using nanobodies as biorecognition element. Determination of fibrinogen in plasma. *Biosensors and Bioelectronics* **52**, 255–260 (2014).

202. Guo, K. *et al.* Rapid single-molecule detection of COVID-19 and MERS antigens via nanobody-functionalized organic electrochemical transistors. *Nat Biomed Eng* **5**, 666–677 (2021).

203. Martin, T. *et al.* Ciltacabtagene Autoleucel, an Anti-B-cell Maturation Antigen Chimeric Antigen Receptor T-Cell Therapy, for Relapsed/Refractory Multiple Myeloma: CARTITUDE-1 2-Year Follow-Up. *J Clin Oncol* **41**, 1265–1274 (2023).

204. Scully, M. *et al.* Caplacizumab Treatment for Acquired Thrombotic Thrombocytopenic Purpura. *New England Journal of Medicine* **380**, 335–346 (2019).

205. Tanaka, Y. Ozoralizumab: first Nanobody® therapeutic for rheumatoid arthritis. *Expert Opin Biol Ther* **23**, 579–587 (2023).

206. Prantner, A. M. *et al.* Anti-Mesothelin Nanobodies for Both Conventional and Nanoparticle-Based Biomedical Applications. *J Biomed Nanotechnol* **11**, 1201–1212 (2015).

207. Gasteiger, E. *et al.* ExPASy: The proteomics server for in-depth protein knowledge and analysis. *Nucleic Acids Res* **31**, 3784–3788 (2003).

208. Huang, J., Ru, B., Li, S., Lin, H. & Guo, F.-B. SAROTUP: scanner and reporter of target-unrelated peptides. *J Biomed Biotechnol* **2010**, 101932 (2010).

209. Huang, J. *et al*. MimoDB 2.0: a mimotope database and beyond. *Nucleic Acids Res* **40**, D271-277 (2012).

210. Accurate structure prediction of biomolecular interactions with AlphaFold 3 | Nature. https://www.nature.com/articles/s41586-024-07487-w.

211. Kurcinski, M., Jamroz, M., Blaszczyk, M., Kolinski, A. & Kmiecik, S. CABS-dock web server for the flexible docking of peptides to proteins without prior knowledge of the binding site. *Nucleic Acids Res* **43**, W419–W424 (2015).

212. Schake, P., Bolz, S. N., Linnemann, K. & Schroeder, M. PLIP 2025: introducing protein–protein interactions to the protein–ligand interaction profiler. *Nucleic Acids Res* **53**, W463–W465 (2025).

213. Wróblewski, K., Zalewski, M., Kuriata, A. & Kmiecik, S. CABS-flex 3.0: an online tool for simulating protein structural flexibility and peptide modeling. *Nucleic Acids Res* **53**, W95–W101 (2025).

214. Redeghieri, P. *et al*. Enzymatic, structural, and biophysical characterization of a single-domain antibody (VHH) selectively and tightly inhibiting neutrophil elastase and exhibiting favorable developability properties. *Protein Science* **33**, e5227 (2024).

215. Sloth, A. B. *et al*. Analysis of Compositional Bias in a Commercial Phage Display Peptide Library by Next-Generation Sequencing. *Viruses* **14**, 2402 (2022).

216. Sell, D. K. *et al*. Using NGS to Uncover the Corruption of a Peptide Phage Display Selection. *Current Issues in Molecular Biology* **46**, 10590–10605 (2024).

217. Thomas, W. D., Golomb, M. & Smith, G. P. Corruption of phage-display libraries by target-unrelated clones: Diagnosis and countermeasures. *Anal Biochem* **407**, 237–240 (2010).

218. Nagy, P. I. Competing Intramolecular vs. Intermolecular Hydrogen Bonds in Solution. *Int J Mol Sci* **15**, 19562–19633 (2014).

219. Melaiu, O. *et al*. MSLN Gene Silencing Has an Anti-Malignant Effect on Cell Lines Overexpressing Mesothelin Deriving from Malignant Pleural Mesothelioma. *PLoS One* **9**, e85935 (2014).

220. Wetzel, S., Seipold, L. & Saftig, P. The metalloproteinase ADAM10: A useful therapeutic target? *Biochimica et Biophysica Acta (BBA) - Molecular Cell Research* **1864**, 2071–2081 (2017).

221. Wang, X., Wang, C. & Pei, G. α-secretase ADAM10 physically interacts with β-secretase BACE1 in neurons and regulates CHL1 proteolysis. *J Mol Cell Biol* **10**, 411–422 (2018).

222. André, A. S., Moutinho, I., Dias, J. N. R. & Aires-da-Silva, F. In vivo Phage Display: A promising selection strategy for the improvement of antibody targeting and drug delivery properties. *Front Microbiol* **13**, 962124 (2022).

223. Song, B. P. C., Ch'ng, A. C. W. & Lim, T. S. Review of phage display: A jack-of-all-trades and master of most biomolecule display. *International Journal of Biological Macromolecules* **256**, 128455 (2024).

224. Derda, R. *et al.* Diversity of Phage-Displayed Libraries of Peptides during Panning and Amplification. *Molecules* **16**, 1776–1803 (2011).

225. Hoogenboom, H. R. *et al.* Selection-dominant and nonaccessible epitopes on cell-surface receptors revealed by cell-panning with a large phage antibody library. *European Journal of Biochemistry* **260**, 774–784 (1999).

226. Folgosa, L., Zellner, H. B., Shikh, M. E. E. & Conrad, D. H. Disturbed follicular architecture in B cell ADAM10 knockouts is mediated by compensatory increases in ADAM17 and TNFα shedding. *J Immunol* **191**, 10.4049/jimmunol.1302042 (2013).

227. Chen, X., Zaro, J. & Shen, W.-C. Fusion Protein Linkers: Property, Design and Functionality. *Adv Drug Deliv Rev* **65**, 1357–1369 (2013).

228. Nemecz, D., Nowak, W. A. & Nemecz, Á. VHH Nanobody Versatility against Pentameric Ligand-Gated Ion Channels. *J. Med. Chem.* **67**, 8502–8518 (2024).

229. Cong, Y., Devoogdt, N., Lambin, P., Dubois, L. J. & Yaromina, A. Promising Diagnostic and Therapeutic Approaches Based on VHHs for Cancer Management. *Cancers (Basel)* **16**, 371 (2024).

230. Jovčevska, I. & Muyldermans, S. The Therapeutic Potential of Nanobodies. *BioDrugs* **34**, 11–26 (2020).

231. Doñate, F. *et al.* Pharmacology of the Novel Antiangiogenic Peptide ATN-161 (Ac-PHSCN-NH2): Observation of a U-Shaped Dose-Response Curve in Several Preclinical Models of Angiogenesis and Tumor Growth. *Clinical Cancer Research* **14**, 2137–2144 (2008).